Characterization of the atmospheric turbulence at the Sutherland site and Conceptual design study and optimization of an Adaptive Optics system for the Southern African Large Telescope

-Laure Catala-

supervisor: Dr Steven M. Crawford (SAAO - SALT)
co-supervisor: Prof. Patricia A. Whitelock (UCT - SAAO)
Dr. David A. H. Buckley (SAAO - SALT)

Thesis Presented for the Degree of
DOCTOR OF PHILOSOPHY
in the Department of Astronomy at the
UNIVERSITY OF CAPE TOWN

submitted: 11th August 2016
Accepted: 14th November 2016
Final Copy: 20th January 2017

Abstract

Name: Laure CATALA

Title: Characterization of the atmospheric turbulence at the Sutherland site and Conceptual design study and optimization of an Adaptive Optics system for the Southern African Large Telescope

Submitted: 11/08/2016 - Accepted: 14/11/2016 - Final Copy: 20/01/2017

To support the potential development of an AO system for SALT, a site monitoring campaign of the Sutherland site was initiated in 2010. This campaign also led to the participation in the development of a new instrument to characterize the atmospheric turbulence. The results from five years of site testing were used in AO simulations in order to demonstrate the potential capabilities of an AO system on SALT.

The site testing study produced up-to-date seeing values and provided a measurement of the atmospheric turbulence profiles. I found a median seeing value of 1.51". The main contributor to the turbulence is clearly the ground layer, below 1 km, responsible for 83% of the turbulence. The next most significant contributor is the wind shear layer around 3 km. Seasonal trends show that slightly worse seeing conditions occur during the winter months due to predominant East, South-easterly winds that are associated with degraded seeing conditions.

In addition to the main site testing campaign, I helped develop the "Profileur de Bord Lunaire" (PBL, Profiler of Moon limb in English), a new instrument that uses the Moon limb to measure the atmospheric turbulence profile. The work on the data processing and inversion method led to the extraction of high altitude-resolution profiles of the turbulence strength. I present here those results along with a comparison with profiles obtained with the Multi-Aperture Scintillation Sensor (MASS).

Using the results from the site testing campaign along with the SALT optical design, I simulated the general dimensioning of a system for SALT that would use a single natural guide star (NGS). The trade-off between performances and sky coverage resulted in a 34x34 system using NGS in the range 10 to 14 magnitude in R-band. The 34x34 dimensions refer to the number of sub-apertures of the Shack-Hartmann wavefront sensor. I conclude with the significant improvement in spectroscopic performance for SALT that could be achieved by implementing an AO system. The gains in encircled/enslited energy are most significant in the near infrared where gains of 183% could be achieved at 1600 nm for the planned Near-infrared upgrade to the Robert Stobie Spectrograph (RSS). The gains in enslited and encircled energy at 700 nm for the visible arm of RSS and the High-Resolution Spectrograph (HRS) are limited to a maximum of 22% and 34%, respectively, due to the large apertures adapted to seeing-limited observations. Further gains could be achieved by designing the next generation of SALT instrumentation to take full advantage of an AO system.

Acknowledgements

After all, time to let it go! It is not perfect but there has to be a final word, so here it is. One last thing as I reflect on those years, I cannot avoid thinking about all the people who made it possible for me to make it through this thesis.

It has been a great journey starting a while back when I made the choice to come to South Africa for a 1 year abroad, that eventually turned into 7! I am grateful to Peter who accepted me into the NASSP Honours program where I began my South African venture. A couple of years later, it is only through the work of Patricia, Steve and David, who placed their trust in me, that I was given the opportunity to carry out my phd in South Africa as a joint UCT - SAAO fellow. I thank them for their continuous support and encouragements. And, Steve, your positiveness and patience were invaluable in the rough moments to put me back on track and restore confidence in my work.

There have been long hours in the cold tweaking screws, aligning the MASS-DIMM and drinking coffee... loads of coffee! Thanks to the SALT team for offering me a warm shelter and the use of the much-needed coffee machine. A special thanks goes to Fred, Veronica, Paul, Encarni and Eric who were very kind in helping out to keep the instrument running when it needed attention, and, of course, Steve and Tim who were part of the instrument setup team and also had their share of numb fingers. Then came the time to face my computer screen and work on all the accumulated data. David and Steve, your inputs, discussions and guidelines towards the best way of extracting and interpreting the results were very precious.

There was also the Nice collaboration for which I have to thank Aziz and Marcel to have accepted to share their knowledge in optical atmospheric turbulence and adaptive optics. My work would not have been the same without their contribution. Thank you for not giving up on me despite the long distance communications which were not always easy. Your competence and our numerous discussions were very fruitful and constructive.

My appreciation also goes to all the SAAO staff, from the IT crew, who avoided some fights between my computer and me, to the administration staff that were always helpful. A special thanks to the mechanical workshop, and in particular Doug, for being so great in enhancing my rudimentary DIY skills. In addition, my observing runs would not have been the same without Maggie and the cheerful Sutherland staff. On the UCT side, Roz your availability to all the students and commitment to easing all administrative process were much appreciated. I am also grateful to Kevin and Nuhaah, along with the rest of the OAD team, to have made me part of the team. My time at the OAD has been crucial to lifting my spirit and clear my mind when I was stuck with my thesis work. And of course, my South African experience would not have been complete without the Gatsby lunch.

And because hard work is not possible without good fun and within a good environment, my officemates and fellow phd students have their share in the completion of this manuscript. I will miss the lunch gossips and silly chats, and I am not quite sure how to survive without the Cocoa Chocolate cake I shared regularly with Pierre. Despite my persistent efforts, I am still at odds with beer. I promise the Astrobeer team to keep working on it and do my best to be a better fellow. Some of the hikes and week-ends away will remain among my best memories. And of course, when living away from home, the importance of the friend circle is priceless. My dear homies, Stef,

Rob, Klaus, Kate and Lena it was such a pleasure to share a home with you. Thank you for your kindness, happy faces and all the good food and unforgettable moments we shared. Nadeem, Fred, Pascal, Titia, Zé, Rupert and Amanda for being the beautiful human beings that you are. I am leaving a whole family behind, full of memories, with crazy moments, hearty laughs, amazing walks and views on Table Mountain and of course a good share of food and wine delectation. Looking forward to seeing your friendly faces around the corner of my next journey!

And because it all started with them, my parents who always supported my choices and fostered my curiosity and openness to the world.

A papi Max dont les fois gras ont égayé mes repas,

A mamie Lucie et son cerisier,

A mamie Yoyo dont les gauffres me manquent,

A papi Valère avec qui j'ai "appris" à conduire ...

Plagiarism Declaration

I, Laure Catala, know the meaning of plagiarism and declare that all of the work in the document, save for that which is properly acknowledged, is my own.
No part of this thesis has been submitted elsewhere for any other degree or qualification.
Some of the work presented in this thesis has been published in journals and or presented at conferences. The relevant publications list is given below:

- L. Catala et al., 2016, MNRAS, *submitted*
  High Altitude Resolution Profiles of the Atmospheric Turbulence with PML at the Sutherland Observatory.
  [$Ch.3$]

- L. Catala et al., 2013, MNRAS, Volume 436, p.590-603
  Optical turbulence characterization at the SAAO Sutherland site.
  [$Ch.$ 2]

- L. Catala et al., 2016, Ground-based and Airborne Telescopes VI, Proceedings of the SPIE, paper 9906-10
  Sutherland site characterization and prospects of an AO system for SALT.
  [$Ch.$ 2$and Ch.$ 4]

- L. Catala et al., 2012, Adaptive Optics Systems III. Proceedings of the SPIE, Volume 8447, 10 pp.
  Dimensioning and performances of an AO system for the SALT.
  [$Ch.$ 4]

- L. Catala et al., 2012, African Skies, Vol. 16, p.95
  Atmospheric Turbulence Characterization at the Sutherland Site: Implications for the Future SALT Adaptive Optics System.
  [$Ch.$ 2]

- T. Pickering et al., 2012, Ground-based and Airborne Telescopes IV. Proceedings of the SPIE, Volume 8444, 7 pp.
  Overview of site monitoring at the SAAO.
  [$Ch.$ 2]

- M. A. Kenworthy et al., 2016, Advances in Optical and Mechanical Technologies for Telescopes and Instrumentation, Proceedings of the SPIE, paper 9912-03
  Polarization dOTF: on-sky focal plane wavefront sensing.

Preamble

South Africa has a long history in astronomy. In 1820 the British Admiralty established the Royal Observatory Cape of Good Hope for the purpose of improving navigation in the Southern Hemisphere. In 1971 an observatory was established at Sutherland and various telescopes moved from elsewhere in the country. In 1972, the South African Astronomical Observatory (SAAO) was formed as a joint operation between Britain and South Africa. In 1986, the British pulled out leaving SAAO to be operated by various South African organizations in turn. The SAAO Sutherland observing station is located 370 km North-East from Cape Town. At a latitude of 32^o23'S and longitude of 29^o49'E and with an altitude of 1768 m above sea level, it is the host of 13 optical, infrared and solar telescopes, among which is the Southern African Large Telescope (SALT). SALT is an 11.1 x 9.8 meter telescope, run by a consortium of 13 institutions based in South Africa, The United States, The United Kingdom, Poland, Germany, India and New-Zealand. Its design is based on its twin, the Hobby-Eberly Telescope (HET) in Texas (Ramsey et al., 1994; Sebring et al., 1994; Sebring & Ramsey, 1997; Ramsey et al., 1997). There are a number of unconventional characteristics in the design of both telescopes:

- a fixed elevation, at 37^o from zenith for SALT,
- a spherical segmented primary made of 91 hexagonal segments in the case of SALT,
- no secondary mirror with all instruments located or fiber-fed at prime focus on the payload, 13 meters above the primary,
- and hence the science target tracking is done by the tracker supporting the payload in an "Arecibo-like" manner.

Such a design helped to significantly cut down the complexity and cost of the overall mechanical system. However, having a spherical primary requires the use of a Spherical Aberration Corrector (SAC, (O'Donoghue & Swat, 2002)) before feeding the science instruments. The SAC constitutes the main optical element of the telescope, conditioning its image quality. Despite an improved design over the HET one, with a new design came new problems. After SALT first light in 2005, a drastic image quality gradient was observed across the 8 arcminutes science field of view (FOV). This issue was nearly fatal to SALT operations and delayed the actual start of science operations for 4 years. However, the problem was successfully fixed (O'Donoghue et al., 2010; Crause et al., 2012), and science operations gradually resumed after the end of the SAC repair in August 2010. Currently, there are 3 main instruments on SALT:

- an imaging camera: SALTICAM (O'Donoghue et al., 2006), operating in the UV-visible range (320-900 nm),
- a low to medium resolution spectrograph: the Robert Stobie spectrograph (RSS, (Burgh et al., 2003; Kobulnicky et al., 2003)) operating at visible wavelength (320-950 nm),
- and the high-resolution spectrograph (HRS), with a "blue" arm covering the 370 to 550 nm wavelength range and a "red" arm covering the 550 to 890 nm range.

In addition, there is an auxiliary port instrument, the Berkeley Visible Imaging Tube (BVIT, (Siegmund et al., 2008)) offering high speed photometry capabilities. SALT has now been operating in full scientific mode for 4 years.

Like any ground-based telescope SALT image quality is degraded by the effect of atmospheric turbulence. While most large telescopes worldwide have now implemented some kind of adaptive optics (AO) system, following its first implementation on a telescope (Merkle et al., 1989, 1991) in 1989, SALT has not yet taken the plunge into the AO world. At the moment all observations with SALT are seeing-limited. However, in the prospect of taking greater advantage of its 11-meter size primary mirror, there has been a rising interest in evaluating the potential improvement that an AO system could deliver. Such a study, requires an extensive and accurate knowledge of the site optical atmospheric turbulence characteristics that one would ultimately like to compensate for with the AO system.

The degradation of astronomical image quality due to the distortion of light from atmospheric turbulence has long been a known problem to astronomers (Roddier, 1981; Tatarskii, 1961; Fried, 1966). Aristotle thought that the twinkling was not an intrinsic property of stars but was due to the unsteadiness of vision when looking at distant objects and explain that planets do not twinkle because they are much nearer (Stocks, 1930). His view was still held in the Middle Ages, even though some as Roger Bacon noticed that the scintillation was stronger closer to the horizon and conclude that the worsening might be due to the higher density of air on the line of sight (Burke, 1962). By the Renaissance it was generally accepted that the scintillation was due to turbulence in the atmosphere causing perturbation in the propagation of light:

"Long Telescopes may cause Objects to appear brighter and larger than short ones can do, but they cannot be so formed as to take away the confusion of the Rays which arises from the Tremors in the Atmosphere."

I. Newton, Opticks,
p. 110-111, book I - part I - proposition VIII, 1717

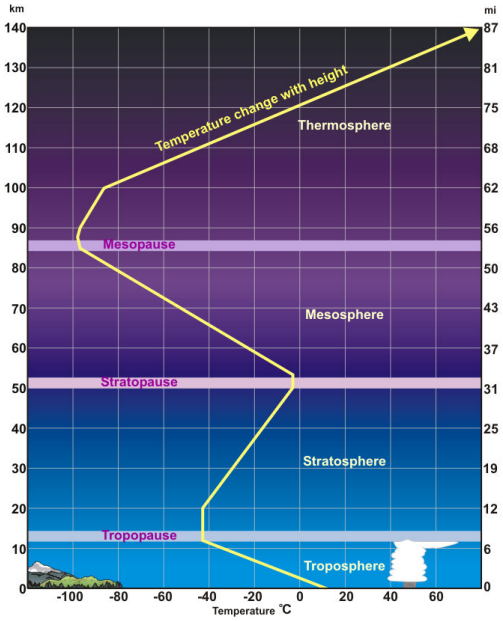

Figure 1: *Representation of the vertical structure of the Earth atmosphere. (credit: NOAA)*

The atmosphere is typically modelled by 5 main layers (Fig.1): the troposphere, the stratosphere, the mesosphere, the thermosphere and the exosphere. The stratosphere contains the Ozone

layer, around an altitude of 25 km, that absorbs most of the Sun ultra-violet (UV) radiation. The mesosphere extends from 50 to 90 km and is the region where the sodium layer used to generate laser guide star (LGS) for adaptive optics (AO) systems lies. The region of interest for us is the troposphere, extending from the ground up to around 20 km. It represents 75% of the atmosphere mass and contains 99% of its water vapour. It is within those last few tens of kilometres from the ground that the optical and infrared light propagation gets disturbed by turbulence. It is important to point out that optical turbulence affecting the image quality at a ground-based telescope is different from large scale turbulence that creates weather systems. The input of energy provided by solar heating creates temperature and pressure gradient between layers at different altitudes. Optical turbulence arises when mechanical mixing of air generates cells of different temperature and density. This produces cells with varying refractive indices. Light paths from different directions in the sky are affected by different series of cells with varying index of diffraction. It is seen as phase differences across the entrance pupil of the telescope, typically represented as a turbulent phase screen. In addition, wind velocity differences between layers and cells create a temporal variation of the refractive indices and hence the phase screen seen by the telescope also evolves in time. In those conditions, as a plane wavefront passes through the atmosphere it gets distorted, resulting in an aberrated wavefront when it reaches the entrance of a ground-based telescope (Fig.2) (Tatarskii, 1961) .

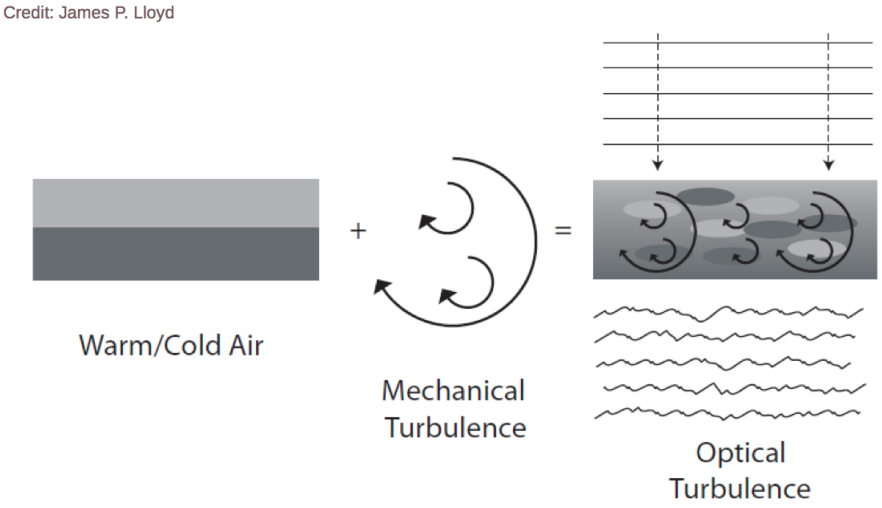

Figure 2: *Atmospheric turbulence and the Propagation of light.*

The theoretical model used to characterize optical turbulence consider the atmosphere as a superposition of infinitely thin layers and described by the Kolmogorov model, as explained in Roddier (1981). The strength of the turbulence in the different layers is determined by the atmospheric structure constant ($C_n^2(h)$), which is dependent on the altitude, h. Two main contributors to the turbulence within the first 20 to 30 km of the atmosphere are generally observed. The ground layer (GL) up to 1 km and the free atmosphere (FA) from 1 km and up. The GL is typically the strongest. In addition to the 2 main layers, the first 20 to 30 m of the GL are defined as the surface layer (SL). The SL can be significantly strong due to convection from the ground, however, most 8 to 10-meter class telescopes have their entrance aperture above it. A strong turbulent wind shear layer is also usually found between 2 and 5 km in the FA. And finally, the top of the FA also can contribute a significant amount of the turbulence due to the jet stream. The cumulative effect pf the turbulence in all of these layers can be calculated by integrating the C_n^2 profile over all altitudes. In terms of image quality, the principal effect is a loss of resolution and a decrease in the peak intensity as the atmospheric turbulence smears out the light of a point source into a disc. The most commonly used parameter to describe the image quality at a given astronomical

site as delivered by its typical atmospheric turbulence conditions is the seeing. The astronomical seeing is defined as the full width at half maximum (FWHM) of a long exposure image point spread function (PSF).

Over the last 20 years, atmospheric site characterization and seeing monitoring for all major astronomical observatories has come into common usage (Els et al., 2009; Chun et al., 2009; Vernin & Munoz-Tunon, 1994). Indeed, the seeing quality is one of the main critical parameters for site selection (IAU Symposium no.19, 1962; Coulman, 1985). Also, continuous monitoring of the seeing is highly valuable in terms of observing time optimization, especially for queue-scheduled observations (Sarazin, 1997). Although a first attempt to correct the image distortion was developed and implemented in 1970, using interferometric method (Labeyrie, 1970) it is only with the advent of adaptive optics (AO) systems (Babcock, 1953; Rigaut, 1992), that one was able to significantly compensate the wavefront distortion. Since such systems rely on the accurate knowledge of optical turbulence properties it led to the implementation of more extensive characterization of the atmospheric turbulence. Through the last decades, new instruments have been developed (GSM (Wood et al., 1995), SLODAR (Harding, 1974), MASS(Kornilov et al., 2003), MOSP (Wilson et al., 2009)) in order to determine, not only the seeing value, but also parameters such as the coherence time (τ_0), the coherence length (r_0) or the isoplanatic angle (θ_0) as well as turbulence profiles via the atmospheric structure constant ($C_n^2(h)$), giving the turbulence strength for layers at different altitudes.

The work done in this thesis is aimed at providing a first assessment of how well an AO system could perform on SALT. This was divided into two main parts. The first aspect of the work was dedicated to an extensive characterization of the Sutherland site in terms of optical atmospheric turbulence. The second aspect was aimed at the actual evaluation of AO performances given the site characteristics and SALT design. In addition, I also worked toward the development of a new site testing instrument.

In Ch. 1 I review the theoretical background of optical atmospheric turbulence and subsequent image distortion at a ground-based telescope along with all associated parameters used to describe the phenomenon. I then give a brief overview of ways of measuring those parameters, describing the instruments that have been used for the Sutherland site monitoring (Ch.2). The last section of this first chapter gives an overview of how one can correct the image distortion by the mean of an adaptive optics system. Since the Sutherland site characterization, done prior to the construction of SALT, very little has been done in terms of optical site quality studies. As the knowledge of the site seeing conditions is primordial to the study and potential development of an AO system, a comprehensive site characterization campaign was initiated in 2010. We permanently set up a MASS-DIMM instrument at the Sutherland site. In addition, I also used data from a SLODAR, on loan from Durham University from February to April 2010. A preliminary study of the first 2 years of data was published in Catala et al. (2013) . Expanding on this work, Ch. 2 is dedicated to the extensive study of characterization and monitoring of optical turbulence at the Sutherland observing station.

In the framework of the Sutherland site characterization, I also got involved in the development of a new instrument for atmospheric turbulence profiling. This project also falls within the context of the next generation of extremely large telescopes (ELTs). With apertures within the thirty to forty meter range, the upcoming AO systems for ELTs have much more severe constraints than current systems. One of them is the need for a highly accurate knowledge of the turbulence profiles with a much higher altitude resolution than that delivered by current dedicated instruments. The Laboratoire Lagrange of the University of Nice designed and built a new instrument, the PBL (also known as PML - Profiler of Moon Limb). It uses lunar limb motion to measure the angle of arrival across the wavefront. By using spatial and temporal cross-correlation, we are able to retrieve the atmospheric parameters (Wilson et al., 2011). The very high altitude resolution is

obtained thanks to the continuous Lunar limb, offering a wide range of separation angles, given by the combination of 2 points along the limb. It also provides the outer scale profile, a critical parameter for the future ELTs adaptive optics systems. As part of this thesis, I developed the data pre-processing scheme for the PBL instrument as well as an inversion method in order to retrieve the $C_n^2(h)$ profiles from the measurements. This work is presented in Ch. 3 that also includes an overview of the PBL working principle and theoretical background.

Finally, based on the results from the site characterization campaign (Ch. 2) as well as SALT specific optical design, I performed a conceptual design study for a potential AO system on SALT. In order to conduct such a study, I ran a number of AO simulations aimed at evaluating the potential performances on SALT. For this general dimensioning study I chose to use the analytical simulation tool PAOLA (Jolissaint, 2014). This allowed us to cover a wide range of parameter space. The results from those simulations are presented in Ch. 4.

Contents

List of Figures

List of Tables

Chapter 1

IMAGING THROUGH THE ATMOSPHERE

Contents

The atmosphere is an inhomogeneous medium made of cells of different temperature, pressure, and humidity. Turbulence arises from the dynamical displacement and mixing of those cells. Temperature variations induce changes in the refractive index, which will, in turn, affect the propagation of light, degrading the image quality and limiting the resolving power of any ground-based telescope. Measuring and understanding how atmospheric turbulence affects light propagation is critical to being able to design and operate adaptive optics (AO) systems that can significantly improve the performance of ground-based telescopes.

In Section 1.1 I summarized the theory describing turbulent media and how it leads to refractive index fluctuation in the atmosphere. I then describe the implications in terms of light propagation and the parameters commonly used to characterize its effects in Section 1.2. Over the years a number of instruments to measure those parameters have been developed and passed into common usage at observatories around the world. In this study, I made use of three of them (MASS, DIMM, SLODAR) and worked on the development of a new one (PBL). In Section 1.3, I give a

Figure 1.1: *Kelvin Helmholtz instabilities. (credit: BrokenInaGlory)*

brief description of the theoretical background and working principle of the three already existing instruments. The PBL will be described in more details in Ch.3. Section 1.4 gives an overview of the AO technique used to correct for image distortion and implemented at many large telescopes. To support the design of an AO system it is often required to use simulations that help to define its general dimensions and the most suitable parameters as constrained by the science goals. I summarized the sources of errors that could affect the performances of an AO system and describe metrics that can be used to assess the improvement in terms of image quality at the entrance of the instrument meant to be fed by the AO system.

1.1 Atmospheric turbulence

1.1.1 Dynamical turbulence

Turbulent flows are common phenomena in nature: cigarette smoke, water flow at a river mouth as well as air flow in the atmosphere. Turbulence of this nature are known as Kelvin-Helmholtz instabilities. Every now and then, one can see those instabilities in the atmosphere due to the presence of clouds as seen in Fig. 1.1. The physics of fluid flow is described by the Navier-Stokes equations established in 1823 (Frisch, 1995; Batchelor, 1970):

$$\frac{\partial \mathbf{u}}{\partial t} + \mathbf{u}.\nabla\mathbf{u} = -\frac{1}{\rho}\nabla P + \nu\nabla^2\mathbf{u},$$

where $\mathbf{u}$ is the three-dimensional velocity vector, P is the pressure, ρ the density and ν the viscosity of the fluid.

The strength of turbulence in a fluid flow is commonly determined by the value of the Reynolds number, $Re = \frac{Lu}{\nu}$, where L and u are respectively the size and the speed of the turbulent flow and ν is the viscosity of the fluid. The Reynolds number gives the ratio between inertial forces and viscous forces within the moving fluid and it characterizes the dynamical instability of a fluid flow compare to a state of laminar flow. Turbulence occurs at high Reynolds number when inertial forces dominate over the viscosity. In that case, the Navier-Stokes equations become non-linear and strongly dependent on the initial conditions. Hence, even though in principle the Navier-Stokes equations are valid not only for laminar flow but also turbulent ones, they are impossible to resolve in practice for most of the problems involving turbulence. It is only with a statistical approach that physicists have developed a theory of turbulence. (Richardson, 1922) gave his qualitative view of atmospheric turbulence:

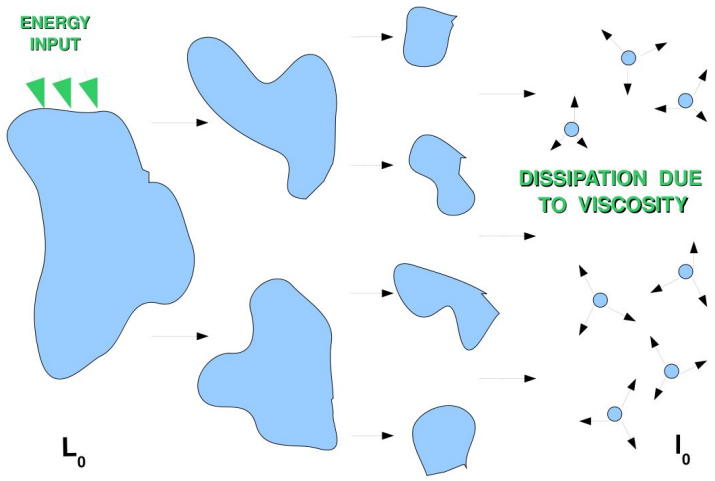

Figure 1.2: *Principle of energy cascade. Energy is injected on large scale and then transferred to smaller scale until dissipation.*

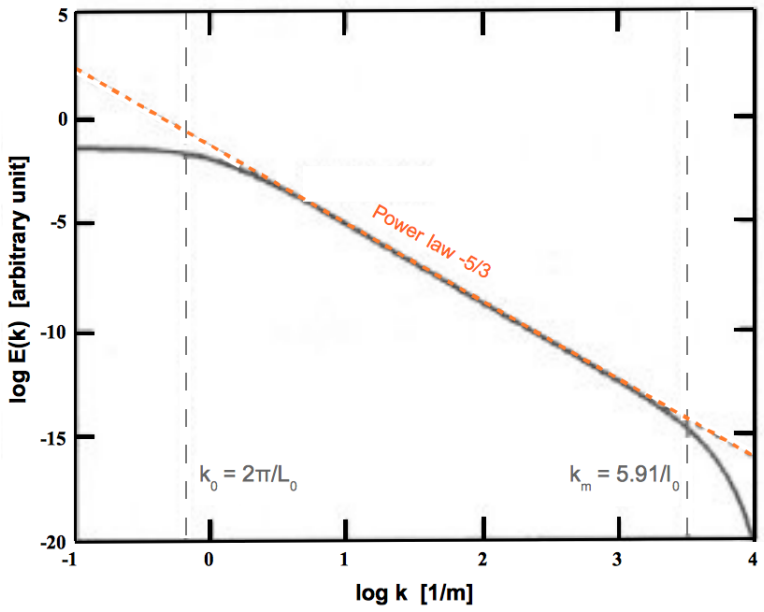

Figure 1.3: *Kolmogorov's spectrum.*

" Big whorls have little whorls which feed on their velocity; little whorls have smaller whorls, and so on onto viscosity."

Based on Richardson description, Andrei N. Kolmogorov (Kolmogorov, 1941a,b; Frisch, 1995) developed a theoretical model of turbulence starting from the hypothesis of energy cascade stating that the energy giving birth to the turbulence is injected onto large structures, associated with the outer scale ($\mathcal{L}_0$), and is then transferred to smaller and smaller structures until dissipation by viscosity when it reaches the inner scale (ℓ_0) size structures (Fig. 1.2). Kolmogorov's model applies only within the range of spatial scales between ℓ_0 and $\mathcal{L}_0$ (Fig. 1.3), corresponding to the inertial domain where the turbulence is fully developed and, from a statistical point of view, isotropic and homogeneous. He establishes that the spectral density of the turbulence kinetic energy for a

monodimensional spectrum was given by,

$$E(k) \propto k^{-5/3},$$

where k is the wave number.

1.1.2 Optical turbulence

The optical turbulence describes the perturbation experienced by light as it goes through a dynamically turbulent medium. In the atmosphere the turbulence causes mixing of air cells with different temperature (T), humidity, and pressure. This produces local variation in temperature, humidity, and pressure. The air refractive index (n) is directly dependent on temperature and humidity and hence also becomes turbulent and randomly variable.

Similarly to the mechanical atmospheric turbulence, the optical turbulence can be described with a statistical approach. Considering a single turbulent layer at an altitude h, the fluctuations of refractive index at a given position $\mathbf{r}$ are defined by:

$$F_n(r,h) = n(r,h) - < n(r,h) >,$$

Those fluctuations can be described by their covariance, also known as the coherence function ($\mathcal{B}_n(\rho,h)$) and their differential variance, also known as the structure function ($\mathcal{D}_n(\rho,h)$) (Tatarskii, 1961):

$$\mathcal{D}_n(\rho,h) = < |F_n(r,h) - F_n(r+\rho,h)|^2 >,$$

$$\mathcal{B}_n(\rho,h) = < F_n(r,h).F_n(r+\rho,h) >,$$

where ρ is the spatial distance between two points of the turbulent layer.

In the inertial range of Kolmogorov's law ($\ell_0 < \rho < \mathcal{L}_0$), the structure constant follows the Obukhov's law (Obukhov, 1949):

$$\mathcal{D}_n(\rho,h) = C_n^2(h)\rho^{2/3},$$

where $C_n^2(h)$ is the atmospheric structure constant of the refractive index fluctuations. It is an expression of the strength of the turbulence in a layer at an altitude h. The spatial power density of the index of refraction fluctuations can be deduced from the structure function and is given by:

$$W_n(f,h) = 0.033(2\pi)^{-2/3}C_n^2(h)f^{-11/3},$$

In astronomy, when observing with ground-based telescope, the light coming from the objects of interest is passing through the atmosphere and will hence be affected by the fluctuations in refractive index.

1.2 Characterizing the optical turbulence

1.2.1 Light propagation through the atmosphere - phase fluctuations

The light coming from astronomical objects, assumed to be at infinity with respect to the telescope entrance aperture, are unperturbed and enter the atmosphere as plane parallel waves. The properties of plane wave propagation through the turbulent atmosphere were extensively described in Roddier (1981). This description considers a plane monochromatic wave propagating downwards from zenith and a non-absorbing horizontally stratified atmosphere within the thin screen approximation, meaning that the layers are assumed to be thicker than the correlation scale but thin enough for the scintillation effect to be ignored.

The fluctuations in refractive index induce small phase changes as a plane wave travels down through the atmosphere. The phase fluctuations ($\Phi(\mathbf{r},\mathbf{h})$) are directly linked to those of the refractive index:

$$\Phi(r,h) = \frac{2\pi}{\lambda}F_n(r,h)\delta h,$$

where λ is the observing wavelength and h and δh the altitude and thickness of the turbulent layer.

The atmosphere is assumed to be a superposition of thin parallel layers and the incoming wave undergoes phase perturbations at each different layers. Those layers are considered statistically independent, and hence the resulting perturbation at ground layer is the sum of all layers contributions: $\Phi(r) = \sum_{i=1}^{N} \Phi(r, h_i)$. Hence the phase difference at the ground can be described by a standard normal distribution. It follows that the structure function of the phase fluctuations, linked to the one of the refractive index, is given by:

$$\mathcal{D}_\Phi(\rho, h) = 2.91(\frac{2\pi}{\lambda})^2 \rho^{5/3} \int_0^\infty C_n^2(h)\delta h,$$

and its power spectral density is given by:

$$W_\Phi(f) = 0.033(2\pi)^{-2/3}(\frac{2\pi}{\lambda})^2 f^{-11/3} \int_0^\infty C_n^2(h)\delta h,$$

It is worth mentioning that the Kolmogorov's model approximation is only valid within the inertial range. In the case of astronomical observation, this means a telescope's diameter must be much larger than ℓ_0 and much smaller than $\mathcal{L}_0$. The inner scale, ℓ_0, is usually not a concern as it ranges between a few millimeters to ~ 1 cm. However, the outer scale has typical values between 10 and 100 meters, and hence, can be of the same order as the diameter large telescopes. In order to take the finite size outer scale into account, other models were developed. The two most commonly used are the Von Karman model (Borgnino et al., 1992):

$$W_\Phi(f) = 0.033(2\pi)^{-2/3}(\frac{2\pi}{\lambda})^2[f^2 + \frac{1}{\mathcal{L}_0^2}]^{-11/6} \int_0^\infty C_n^2(h)\delta h,$$

and the Greenwood-Tarazano model (Greenwood & Tarazano, 1974):

$$W_\Phi(f) = 0.033(2\pi)^{-2/3}(\frac{2\pi}{\lambda})^2[f^2 + \frac{f}{\mathcal{L}_0}]^{-11/6} \int_0^\infty C_n^2(h)\delta h,$$

In the general description of the turbulence and its effects on image quality, I will assume a Kolmogorov's model. For all models, the information on the turbulence strength and distribution is contained in the $C_n^2(h)$ integral. Looking at the $C_n^2(h)$ value for different altitudes, one can draw a profile of the turbulence strength and identify the dominant layers contributing to the image distortion at the telescope. General parameters describing the overall characteristics of the turbulence affecting light propagation were derived based on the $C_n^2(h)$ integral.

Also, other parameters were defined in order to characterize the turbulence, those measure the overall effect of the atmosphere, and hence depend on the $C_n^2(h)$ integral.

1.2.2 Optical atmospheric turbulence parameters

In terms of how the perturbation of the wavefront affects the image quality at the telescope, a number of parameters have been defined to characterize and quantify the amount of turbulence and image degradation. I define the four main ones in this section. Note that as a common usage, all turbulence parameters are given for $\lambda = 500$ nm and at zenith ($\gamma = 0$).

1.2.2.1 The Fried parameter

Even though, in principle, the resolution of a telescope increases with its diameter size, Fried and Could (Fried, 1982, 1966) showed that there is a critical diameter size over which the telescope resolution is limited by the size of the atmospheric turbulent cells. This size is defined as the

coherence length of the turbulence and commonly known as the Fried parameter (r_0). Any telescope smaller than the Fried parameter will have its resolution (**R**) set by its diameter (D), such that **R**= λ/D. The resolution of larger telescopes will be set by the Fried parameter, such that **R**= λ/r_0 (Fig. 1.4).

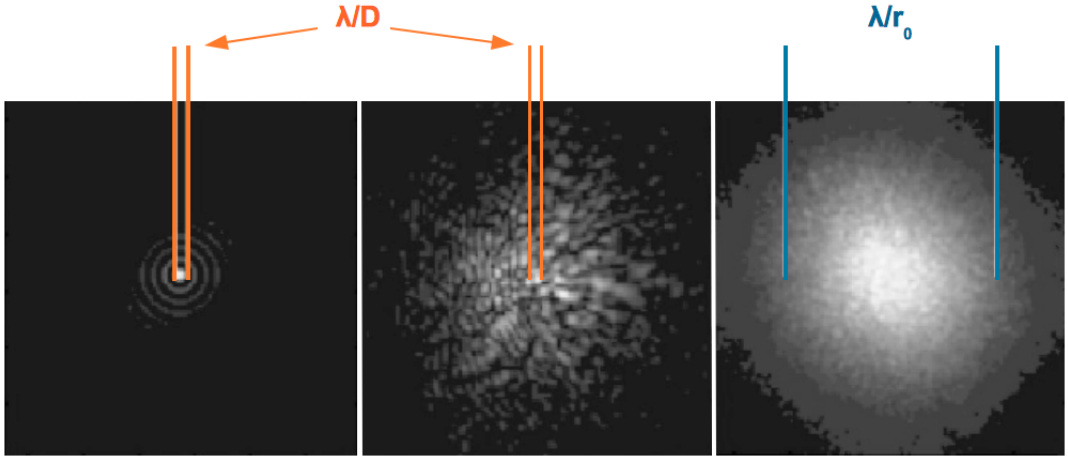

Figure 1.4: *Effect of atmospheric turbulence on astronomical images, for a telescope with diameter $D > r_0$. Left: Diffraction limited image, in the case of no turbulence. Middle: short exposure image with speckles of the size of the telescope diffraction limit. Right: long exposure image resulting in a blurred image, which size is determined by the strength of the turbulence and depend on r_0.*

Considering long exposure images, the resolving power of a telescope (R) is given by the integral over all frequency (f) of the product of the optical transfer function of the telescope ($T(f)$) and the optical transfer function of the atmosphere ($B_\psi(\lambda f)$):

$$R = \int B_\psi(\lambda f).T(f)df.$$

The contribution of the telescope alone, noted R_D, is given by $R_D = \int T(f)df$. For a circular aperture of diameter D with no obscuration this gives:

$$R_D = (\frac{\pi}{4})(\frac{D}{\lambda})^2.$$

The contribution from the atmosphere alone, noted R_∞, depends only on the size of the atmospheric turbulent cells and is hence given by: $R_\infty = \int B_\psi(\lambda f)df$. This can also be expressed as follow:

$$R_\infty = \int \exp^{-Kf^{5/3}} df,$$

with $K = \frac{1}{2}\,[2.914\,k^2\,\lambda^{5/3}\int C_n^2(h)dh]$. It can then be rewritten as:

$$R_\infty = \frac{6\pi}{5}\Gamma(6/5)K^{-6/5},$$

We define an equivalent telescope diameter, d, that solves $R_\infty = R_d$. This corresponds to the equivalent diameter of a telescope having the same resolution as the one delivered by the atmosphere and this is the definition of the Fried parameter, $r_0 = d$. Using the expression for R_∞ and R_D, replacing D by r_0 we can find an expression for r_0:

$$r_0 = [0.423k^2 \int C_n^2(h)dh]^{-3/5},$$

defined at zenith, with $k = \frac{2\pi}{\lambda}$.

Observations at a larger zenith angle (γ) are more affected by the turbulence since one is observing through a thicker atmospheric layer. An additional factor is necessary to take this into account, the general formula for the Fried parameter is given by:

$$r_0 = 0.185\lambda^{6/5}[sec(\gamma)\int C_n^2(h)dh]^{-3/5},$$

with $sec(\gamma) = \frac{1}{cos(\gamma)}$. The Fried parameter also corresponds to the characteristic size of the turbulence cells. Its value has an importance for the dimensioning of an AO system (see Section 1.4.1).

1.2.2.2 The seeing

Another commonly used parameter to characterize the global effect of turbulence on image quality is the seeing (ϵ_0). Its value is directly related to the Fried parameter via the following relation:

$$\epsilon_0 = 0.98\frac{\lambda}{r_0}.$$

which gives:

$$\epsilon_0 = 5.29\lambda^{-1/5}[sec(\gamma)\int C_n^2(h)dh]^{3/5}.$$

This is an estimation of the theoretical value of the angular resolution that could be achieved by a ground-based telescope. In the case of telescopes with a pupil larger than r_0, the resolution will be set by the Fried parameter rather than its diameter. Indeed, in this case, r_0 represents the smallest diffractive element of the system, and ϵ_0 is the smallest angular size that can be resolved. For telescopes smaller than r_0, their resolution remains set by their diameter size.

1.2.2.3 The isoplanatic angle

Due to the spatial variation of the turbulence, two wavefronts incoming at the entrance of the telescope from different angles do not "see" the same turbulence on the high altitude layers. This effect is known as anisoplanatism (Fig. 1.5) and affects the size of the corrected field of view by an adaptive optics system.

The isoplanatic domain of a telescope, over which one can consider that all wavefronts encounter the same turbulence, varies between few arcseconds to tens of arcseconds depending on the site location and observing wavelength. The definition of the isoplanatic angle by Fried states that it corresponds to the maximal angular distance from the optical axis within which the error on the estimation of the turbulence phase has a variance lower than 1 rad^2 (Fried, 1982). The expression of the isoplanatic angle as a function of the Fried parameter has been given in Roddier (1981):

$$\theta_0[rad] = 0.314\frac{r_0}{\bar{h}},$$

where, $\bar{h} = \left[\frac{\int C_n^2(h)h^{5/3}dh}{\int C_n^2(h)dh}\right]^{3/5}$, is an average altitude of the turbulence. Replacing r_0 by its expression its gives:

$$\theta_0[rad] = \frac{0.058}{\bar{h}}\lambda^{6/5}[sec(\gamma)\int C_n^2(h)dh]^{-3/5}.$$

Note that if ϵ_0 is only mildly chromatic with a $\lambda^{-1/5}$ dependence, θ_0 is strongly chromatic with a $\lambda^{6/5}$ dependence. This will have an impact on the correction that can be delivered by a given AO system when observing at different wavelengths, as we will see in Ch. 4.

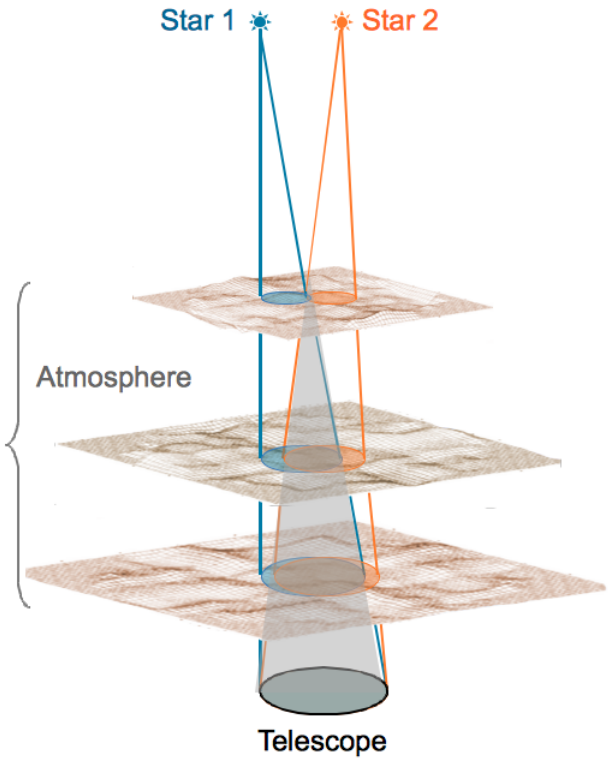

Figure 1.5: *Anisoplanatism effect. The light coming from 2 different stars does not follow the same path through the atmosphere and hence does not encounter the same turbulence. This effect gets stronger for the upper layers of the atmosphere.*

1.2.2.4 The coherence time

The atmospheric turbulence is dynamic and hence also evolves in time. The coherence time is an estimation of the characteristic time after which the turbulence at a given point has changed. The temporal properties of the turbulence are deduced from the Taylor hypothesis (Taylor, 1938), also known as "frozen turbulence". Considering the atmosphere as a succession of independent parallel phase screens at different altitude h with a speed $v(h)$. For a turbulence spatial statistic of type Kolmogorov, Conan et al. (1995) have shown that the temporal power spectrum is related to the spatial power spectrum. This relation, for one layer, is given by:

$$\phi(\mathbf{r},t+\tau) = \phi(\mathbf{r}-\tau\mathbf{V},t),$$

where t is the time, τ is the time difference, and $\mathbf{r}$ is the position.

The characteristic time of the turbulence is given by the structure function of the phase:

$$D_\phi(\tau) =< [\phi(\mathbf{r},t) - \phi(\mathbf{r},t+\tau)]^2 >\simeq 6.88(\frac{\bar{V}\tau}{r_0})^{5/3},$$

where, $\bar{V} = \left[\frac{\int C_n^2(h)|V(h)|^{5/3}dh}{\int C_n^2(h)dh}\right]^{3/5}$, is an average wind speed of the turbulence.

The coherence time (τ_0) is defined as the characteristic time over which $D_\phi(\tau)$ remains lower than 1 rad^2, which is:

$$\tau_0[s] = 0.314\,\frac{r_0}{\bar{V}},$$

The coherence is also of importance for an AO system, as this will set the speed at which the system needs to be able to measure and apply a correction to the turbulent wavefront (see Section 1.4.3).

1.3 Measuring the atmospheric turbulence

Once the theoretical formalism to describe the turbulence and its effects on optical light propagation was established, astronomers have developed a number of instruments to measure the parameters relevant for astronomical site characterization, r_0, ϵ_0, θ_0 and τ_0, as well as the $C_n^2(h)$ profile. Over the past 20 years, more than 10 different instruments and derivatives have been developed and used at different observatories to measure either the integrated parameters (r_0, θ_0,τ_0) or actual turbulence profile with different sensitivity and altitude resolution. Within the scope of this thesis, three different systems were used for the Sutherland site characterization that started in 2010. I give an overview of these instruments in this section.

1.3.1 Differential Image Motion Monitor (DIMM)

The DIMM, measuring the overall seeing, is the most commonly used seeing monitor. Due to the refraction of light throughout the different atmospheric layers and the temporal variation of the turbulence, short exposure images of a single star, by a telescope, will not form at the exact same position from one instant to the next one, causing the star to "dance around" in the focal plane. The principle of a DIMM is to measure this motion. The method is based on the differential motion of two images of a single star. The system uses a two hole mask on the entrance pupil of the telescope, one of them being fitted with a thin wedge prism in order to split the star light into two images. Telescope vibration and other instrumental noise can be suppressed by measuring the differential motion of the two images formed on the camera. The variance of the differential image motion is calculated for a series of images. A direct relationship between the variance and the Fried parameter exists. The principle of DIMM was first introduced by Sarazin & Roddier (1990) and more recently described in Kornilov & Kornilov (2011). Developments of the theory were also presented in Martin (1987) and expanded in Tokovinin (2002), where the following relationship is derived:

$$\sigma_{l,t}^2 = K_{l,t}(\lambda/D)^2(D/r_0)^{5/3},$$

with
$K_l = 0.364(1 - 0.532S^{-1/3} - 0.024S^{-7/3})$ and,
$K_t = 0.364(1 - 0.798S^{-1/3} - 0.018S^{-7/3})$,
where σ^2 is the variance of the differential image motion, λ is the wavelength, l and t stand for longitudinal and transverse and S is the ratio between the sub-apertures separation, b, to their diameter D.

The seeing is given by:

$$\epsilon_0 = \frac{0.98\lambda}{r_0} = 0.98\left(\frac{D}{\lambda}\right)^{0.2}\left(\frac{\sigma_{l,t}^2}{K_{l,t}}\right)^{0.6},$$

The DIMM principle is presented and discussed in more details in Sarazin & Roddier (1990). The DIMM is the most commonly used instrument for the seeing monitoring at astronomical sites. Some site studies based on DIMM measurements include: Cerro Pachon (Els & Sebag, 2011) host of the Large Synoptic Survey Telescope (LSST), Cerro Las Campanas (Berdja et al., 2011) host of the Giant Magellan Telescope (GMT) and Xinglong (Liu et al., 2010) host of the Large Sky Area Multi-Object Fibre Spectroscopic Telescope (LAMOST), as a non-exhaustive list.

1.3.2 Multi-Aperture Scintillation Sensor (MASS)

Apart from image motion, the atmospheric turbulence induces intensity fluctuations in the incoming light from a star. This is what we call scintillation and is seen as twinkling. As the light travels through turbulent layers in the atmosphere, the wavefront suffers phase distortions. Those phase distortions cause diffraction of light in different directions for different locations along the wavefront. After propagating down from the turbulent layer altitude to the telescope entrance

aperture, we observed variations in the pupil illumination as the light converges towards some areas and diverges from others (Fig. 1.6). While the magnitude of the intensity fluctuations over the pupil depends on the strength of the turbulent layer, their spatial scale is set by the altitude of the layer it originated from (Fig. 1.7). Moreover, as the turbulent layer is blown across the field of view by the wind it creates what is commonly called "flying shadows" and can be seen in short-exposure images of the telescope pupil plane. From Fig. 1.7, one can see that for lower atmospheric layers the scintillation effect becomes weaker. This is easily explained from the geometry of the effect. The small angle on the distorted wavefront can only create a significant deviation at the telescope entrance pupil if it propagates through a long enough distance.

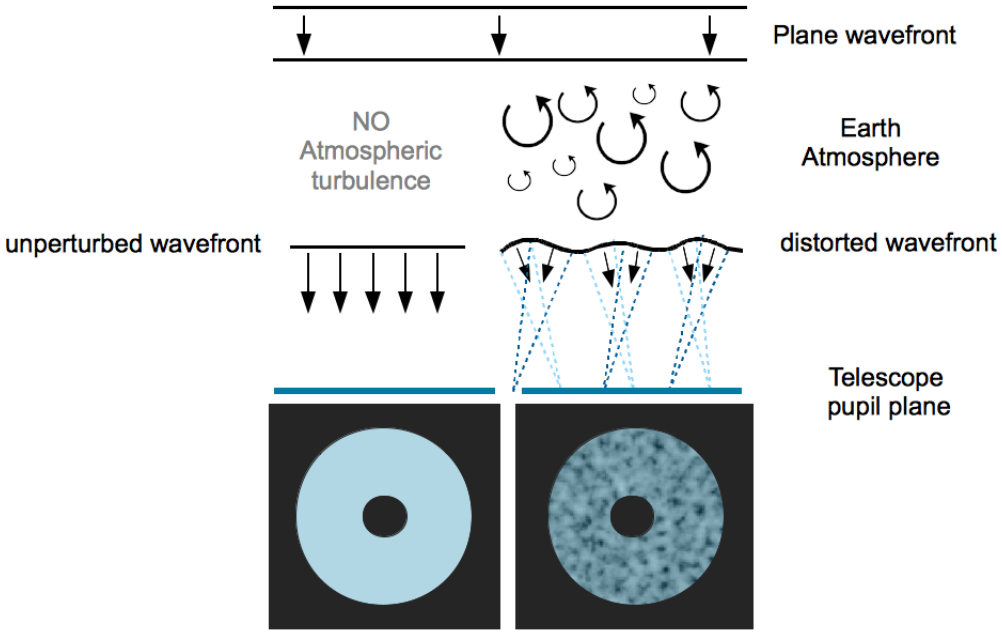

Figure 1.6: *Schematic of scintillation effect due to atmospheric turbulence.*

The MASS instrument has been developed to provide a measurement of the free atmosphere (FA) seeing as well as a low-resolution profile of the turbulence from 500 m and above. Based on the well-established relationship between scintillation from a single star and the atmospheric seeing (Roddier, 1981), it uses measurements of the scintillation in four concentric pupil apertures via photomultiplier tubes (PMTs) to recover the free atmosphere turbulence profile (Tokovinin et al., 2003b). The resolution and height of the measured Cn^2 values are set by the diameter of the different apertures acting as spatial filters. Using both the scintillation indices (SI) and the differential scintillation indices (DSI), the MASS, in the configuration of a MASS-DIMM, gives the C_n^2 values at 0.5, 1, 2, 4, 8 and 16 km above the telescope. Moreover, the MASS also provides values for the coherence time and the isoplanatic angle.

The SI, for aperture A, and DSI, between A and B, are computed as follow:

$$s_A^2 = \langle \sigma_{I_A}^2 \rangle / \langle I_A^2 \rangle,$$

$$s_{AB}^2 = \langle (\frac{\Delta I_A}{\langle I_A \rangle} - \frac{\Delta I_B}{\langle I_B \rangle})^2 \rangle,$$

where I_X is the instantaneous light intensity measured in aperture X and ΔI_X the standard deviation of its fluctuations over one integration time measurement.

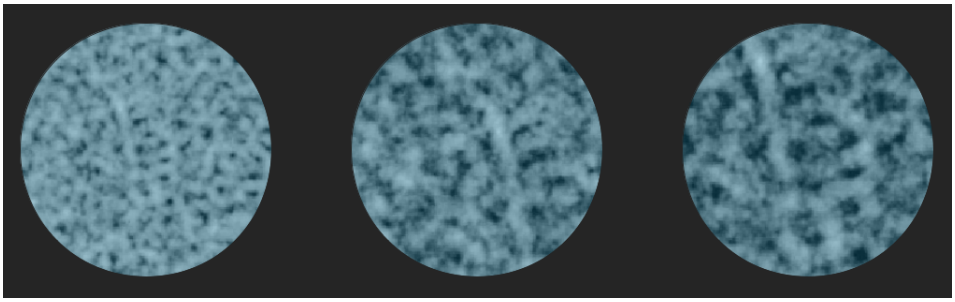

Figure 1.7: *Scintillation pattern as a function of the turbulent layer altitude. From left to right, the layer altitudes are 2,6 and 10 km respectively.*

The turbulence profile is then recovered via the following relationship:

$$s_x = \sum_{i=1}^{I} J_i W_x(h_i sec\gamma) sec\gamma,$$

where s_x is the measured scintillation index, $J_i = \int_{i^{th}layer} C_n^2(h)dh$, is the integral of the refractive index structure constant over the ith layer, γ is the zenith angle, $z = h_i sec\gamma$ is the propagation distance and the h_i are altitudes counted from the observatory level. $W_x(z)$ are weighting functions depending on wavelength and aperture size.

Using the obtained C_n^2 integral one can calculate the free atmosphere seeing, using:

$$\epsilon_f = 5.307\lambda^{-1/5}[\int_0^\infty C_n^2(h)W_0(h)dh]^{3/5},$$

where λ is the wavelength, ϵ_f is the seeing of the free-atmosphere (from 0.5 km up) and $W_0(h)$ is an arbitrary function (varying from 0 to 1) determining which layers contribute to the seeing. $W_0 = 1$ everywhere gives the zeroth moment of turbulence profile (Roddier, 1981).

A full description of the device is given elsewhere (Kornilov et al., 2003). Some site studies based on MASS measurements includes: Mauna Kea (Tokovinin et al., 2005), Cerro Paranal (Dali Ali et al., 2010), and the Thirty Meter Telescope (TMT) sites testing campaign (Els et al., 2008), as a non-exhaustive list.

1.3.3 SLOpe Detection And Ranging (SLODAR)

The SLODAR instrument is used to probe the ground layer (GL) profile of the atmospheric turbulence. The method uses a double star target to measure the spatial covariance of the slope of the wavefront phase aberration, seen at ground level, of two different paths through the atmosphere. In order to create two sets of spots (Fig. 1.8), one for each star, the system is made of a Shack-Hartmann wavefront sensor (SHWFS) mounted on a small aperture telescope. Aside from the GL profile, the SLODAR is also using the DIMM technique, described in section 2.3.1, to determine the overall seeing value.

The SHWFS produces two sets of spots separated by a distance $S = H\theta$, where H is the height of the turbulent layer and θ the separation angle of the double star. The separation of the double star has to be chosen so that the spot pattern of the two stars does not merge. They are either fully separated or interleaved (Fig. 1.8, b).

The number of sub-apertures of the SHWFS is limited by diffraction. In order to measure centroid motion due to seeing, they should be 5 to 10 cm in diameter. The vertical resolution (δH) and the maximum sensing altitude (H_{max}) of the system are given by:

$$\delta H = \frac{D}{n_{sub}\theta},$$

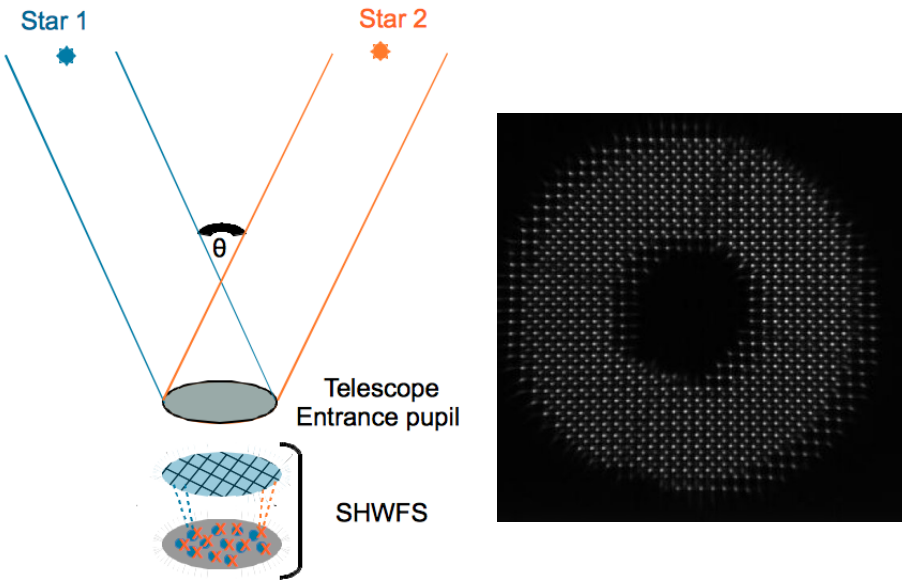

(a) (b)

Figure 1.8: *Working principle of a SLODAR. Left: The Light from a double star with separation angle θ is imaged by a Shack Hartmann wavefront sensor (SHFWS). The lenslet array is positioned on the telescope image pupil plane and focuses the light onto the CCD, creating a spots pattern for each star. Right: Interlace spot pattern from a double star imaged by a SLODAR (Butterley et al., 2008)*

$$H_{max} = n_{sub}\delta H,$$

where D is the diameter of the telescope, n_{sub} is the number of sub-apertures, θ is the angular separation of the double star.

A double star with a larger separation angle will give a better vertical resolution at the expense of a lower maximum altitude. The maximum separation is set by the detector size and the system field of view (FOV). The extraction of the $C_n^2(h)$ profiles from the correlation of the two spots patterns from the SHWFS can be retrieved in real time. The procedure consists in recording the short exposures of the Shack-Hartmann mask images for each star, then calculates the wavefront slopes on the two orthogonal directions for each pattern in order to compute the cross-correlation between the two patterns. If $s_{i,j}(t)$ is the slope on the sub-aperture (i,j) and $s'_{i,j}(t)$ on the corresponding sub-aperture for the second star, the cross-correlation is then expressed as follow:

$$C(\delta i,\delta j) = \langle \sum_{i,j} \frac{s_{i,j}(t)s'_{i+\delta i,j+\delta j}(t)}{O(\delta i,\delta j)} \rangle,$$

where $O(\delta i,\delta j)$ is the number of overlapping sub-apertures for which data are available and for separation $(\delta i,\delta j)$. The brackets are an average over a number of independent frames, typically 1000 over 30s.

The autocorrelation, $A(\delta i,\delta j) = \langle \sum_{i,j} \frac{s_{i,j}(t)s_{i+\delta i,j+\delta j}(t)}{O(\delta i,\delta j)} \rangle$, is also computed, and is used to recover the turbulence profile together with $C(\delta i,\delta j)$, via deconvolution, which, in absence of noise, is given by:

$$C_n^2(h) \propto F^{-1}[F(C)/F(A)],$$

where F is the Fourier transform operator.

In practice, the results are affected by shot noise on the SHWFS, which affects the centroid calculation, as well as noise associated with the finite number of realizations averaged in the

calculation of C and A. This leads to negative C_n^2 values and non-zero values at negative altitudes. Least-squares solutions via iterative minimization subject to the constraint of positivity and finite extent are used to remove the noisy data.

An extensive description is available elsewhere (Butterley et al., 2006). Some site studies based on SLODAR measurements includes: The European Extremely Large Telescope (E-ELT) site testing campaign (Wilson et al., 2004), Cerro Paranal (Lombardi et al., 2014) host of the Very Large Telescopes (VLTs) and Mauna Kea (Butterley et al., 2008), as a non-exhaustive list.

1.4 Correcting the image distortion with Adaptive Optics

Until the advent of adaptive optics (AO) systems in 1956 (Babcock, 1953), and the first application to astronomical instrumentation in 1992 (Rigaut, 1992), the only way to avoid the effect of atmospheric turbulence was to place a telescope above the atmosphere into space. This was done since the early seventies for high energy and UV observations that are hardly possible from the ground due to the atmosphere opacity at those wavelengths. However, it is only in the late eighties, early nineties that we started building space telescopes for observations in the visible and the infrared that were previously done exclusively from the ground. The most popular of them being the Hubble Space Telescope (HST) which was launched in 1990, and is still operating 26 years later . At the time, the image quality in the UV and visible range of the spectrum got 5 to 10 times better with the HST as compared to the available seeing limited ground-based telescopes. Prior to the implementation of AO systems on ground-based telescopes, partial correction of the seeing was performed thanks to the speckle interferometry technique developed by Antoine Labeyrie (Labeyrie, 1970).

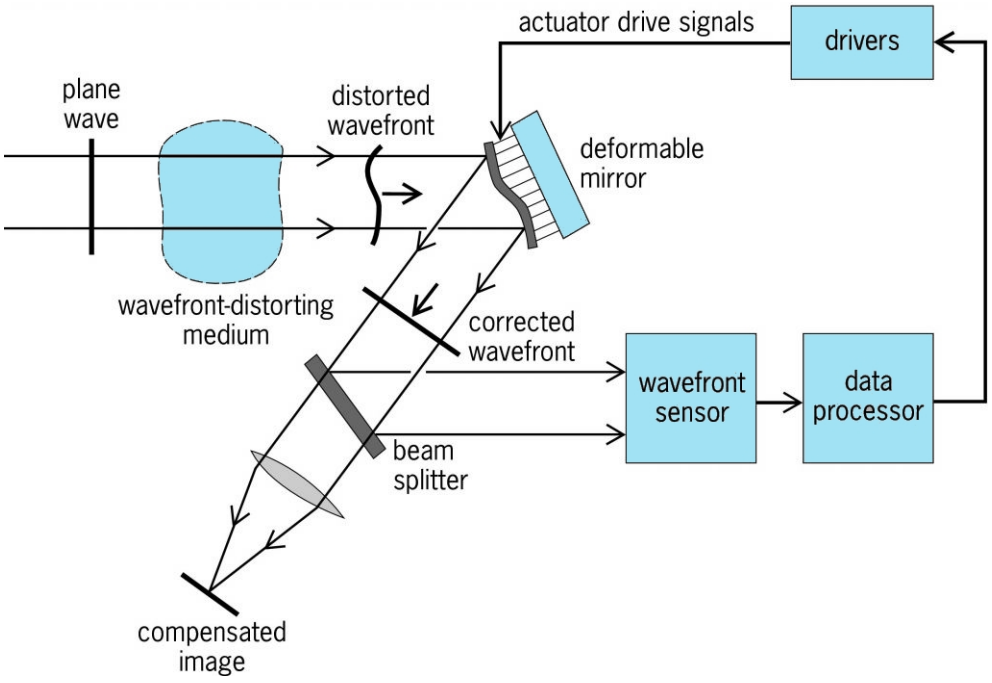

Figure 1.9: *Adaptive optics working principle.*

The idea behind AO systems is to measure the wavefront distortion and compensate it by the mean of a deformable mirror (DM). In principle, an AO system is simple; in practice, there are many issues that need to be accounted.

Fig. 1.9 represents a schematic of the general layout of an AO system. Any AO system is made up of three main components, the wavefront sensor (WFS), the control loop and the deformable

mirror (DM). All three parts have to be accurately tuned with respect to each other in order to optimize the efficiency of the system. Hereafter I give a description of each of them as well as their parameters and how they are related to each other and affected by on atmospheric parameters.

1.4.1 The Wavefront sensor

There are several types of wavefront sensors in use. The three main ones used in astronomy are: the Shack-Hartmann (Jiang & Li, 2009; Primot et al., 1990), the Pyramid (Ragazzoni & Farinato, 1999) and the curvature (Roddier, 1988). More recently holographic, non-linear curvature and differential optical transfer wavefront sensor have successfully been tested. In the case of SALT and for the general dimensioning study I only considered the most commonly used wavefront sensor, the Shack-Hartmann that I briefly describe below.

The Shack-Hartmann Wavefront Sensor (SHWFS) is made of a lenslet array and a camera (Fig. 1.10). The lenslet array spatially samples the wavefront in order to recover the local slopes. A SHWFS is characterized by its number of sub-apertures. The lenslet array is conjugated with the pupil of the system, and the camera is positioned in the focal plane of the lenslet array. Each lenslet produces a spot image on the camera, as one can see in Fig. 1.10. For an incoming plane wavefront, which would be the case without turbulence, each spot is centered on the optical axis of the lenslet (grey dots). In the case of a turbulent wavefront, the spot deviate from its nominal position (blue dots). The displacement with respect to the nominal position is directly related to the local slope of the wavefront part sensed by the lenslet. The following expression gives the relationship between the displacement (x_c, y_c), the phase (ϕ) and the slope or angle of arrival (θ_x, θ_y):

$$\theta_x = \frac{x_c}{f_{ul}} = \frac{\lambda}{2\pi S} \int\int \frac{\partial \phi}{\partial x} dxdy,$$

$$\theta_y = \frac{y_c}{f_{ul}} = \frac{\lambda}{2\pi S} \int\int \frac{\partial \phi}{\partial y} dxdy,$$

where f_{ul} is the focal length of the lenslet array and S is the surface of a lenslet. The scintillation effect is neglected in those expressions.

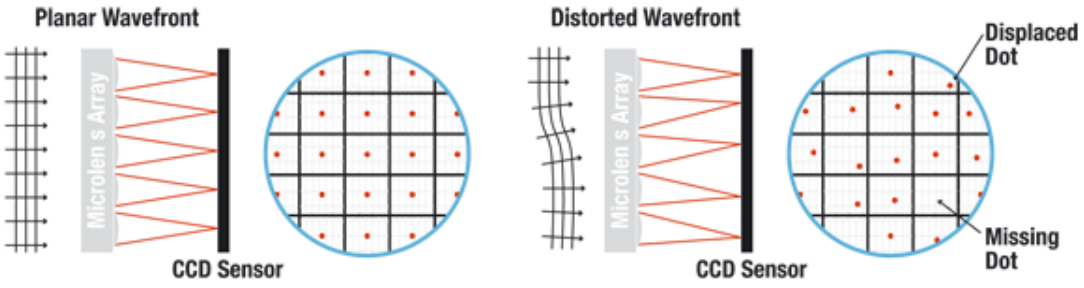

Figure 1.10: *Shack-Hartmann working principle. Left: spot pattern created for an incoming flat wavefront, with no turbulence. Right: spot pattern created for an incoming turbulent wavefront. The displacement of the dots with respect to the nominal position obtain with no turbulence is directly related to the local wavefront slope sensed by each lenslet. (credit: Thorlabs - AO Tutorial)*

From the spots pattern, there are different ways of determining the spots position and displacement. The most commonly used is the Center of Gravity method (CoG). Some systems also use quad-cell (QC) to determine the position of the spot. I will talk more about the estimation of the centroid position in Section 1.5. The measured displacement, $\mathbf{z}$, from the SHFWS is linked to the incident phase ϕ, expressed on a base of modes, Zernike modes are commonly used. The relation is given by:

$$\mathbf{z} = \mathbf{D}\phi + \mathbf{w},$$

where **D** is the WFS matrix and **w** is the noise, mainly due to photon noise (σ^2_{ph}) and detector noise (σ^2_{detect}):

$$\sigma^2_{ph} = \frac{\pi^2}{2n_{ph}}(\frac{X_t}{X_d})^2,$$

$$\sigma^2_{detect} = \frac{\pi^2}{3}(\frac{\sigma_e n^2_{pix}}{n_{ph} X_d})^2,$$

where n_{ph} is the number of photons received by each sub-apertures, X_t is the full width at half maximum (FWHM) of the spot in pixels and X_d is the reference FWHM of the spot when there is no turbulence. σ_e is the standard deviation of the pixel noise in electrons and n_{pix} is the linear number of pixels taken to compute the centroid position.

In an ideal case, increasing the number of sub-apertures gives a better spatial sampling of the wavefront improving its reconstruction. In practice, one can see that the noise limits the sampling. A guide star, natural (NGS) or laser (LGS), is used for the sensing. The amount of light per sub-aperture is hence limited by the magnitude of the star. Increasing the number of sub-aperture reduces the number of photons in each aperture and increases the noise leading to a poor precision on the centroid. That is the first trade-off to consider when dimensioning an AO system.

1.4.2 The Deformable Mirror

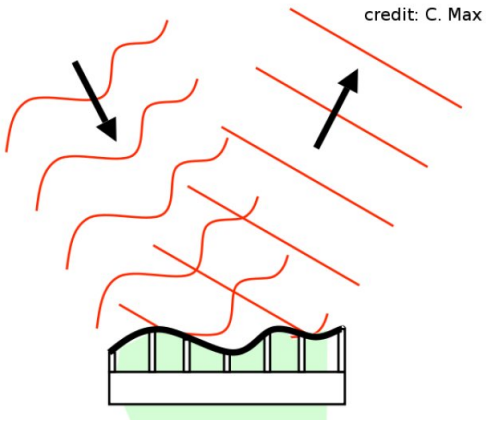

Figure 1.11: *General principle of a deformable mirror. The mirror is shaped in order to counteract the incoming wavefront distortion and reflect back a corrected plane wavefront. (credit: C. Max)*

The DM is used for the wavefront correction. It is made of a deformable reflecting surface supported by actuators used to shape it in order to correct the wavefront distortion (Fig. 1.11). After the DM, the wavefront is characterized by the corrected phase, $\phi_{corr} = \mathbf{Nu}$, where **N** is the influence matrix of the mirror containing all the influence functions of the mirror (deformations of the mirror in response to the activation of each of the actuator), and **u** is the commands matrix applied to the mirror. Depending on the matrix **N**, the deformation can be expressed on a modal basis (this is the case for Zernike modes) or on a zonal basis. The accuracy of the correction is mainly limited by the mirror time response, between the moment the command are sent and the moment they are applied. Other limiting factors are its stroke, limiting the amount of correction that can be applied, and its number of actuators, limiting the number of modes/zones that can be corrected. More actuators and more stroke allows for a better mirror shape but increases the time response. Again the optimization of an AO system will require to balance off those parameters.

1.4.3 The Control Loop

The control loop (CL) role is to determine the commands need to send to the DM in order to compensate for the wavefront distortions. It uses a command law that transforms the measures done by the WFS (**s**) into commands for the DM (**a**).

The command law is modeled by a matrix ($\mathcal{R}$):

$$\mathbf{s} = \mathcal{R}\mathbf{a}.$$

The command law is determined by poking individually each of the DM actuators, and record the WFS measures for each of them in the matrix $\mathcal{R}$. $\mathcal{R}$ is a NxM matrix where N is the number of measurements of the WFS and M is the number of actuators on the DM. This process assumes that the AO system is linear. The inversion of $\mathcal{R}$ gives the command law. However, $\mathcal{R}$ is generally not a square matrix and hence is not directly invertible. $\mathcal{R}^{-1}$ can be obtained using a singular value decomposition method:

$$\mathcal{R}^{-1} = (\mathcal{W}\mathcal{D})^{-1}\mathcal{U}^t,$$

where ^{t} indicates the transpose of the matrix. The column of $\mathcal{W}$ and $\mathcal{U}$ matrices make up orthonormal sets of the mirror deformation and actuator signal spaces respectively. The diagonal matrix $\mathcal{D}$ contains the singular values representing the "gains" of the different modes. Small singular values are associated with the requirement of large actuators movement to produce the necessary deformation. Hence the condition factor of the matrix $\mathcal{D}$, the ratio of the smallest to the largest singular value, gives a measure of the controllability of the mirror. Filtering the smallest values can improve the system behavior.

The optimization of an AO system is never perfect due to different sources of errors in the system and in particular the temporal delay which is the main constraint on the CL. In order to correct for the right deformation, the time covering measurements by the WFS, command reconstruction by the CL, and DM response time should ideally be shorter than the coherence time (τ_0) of the turbulence (of order of few ms). The faster the calculation is completed by the CL can be done the lower the temporal error will be.

1.5 Optimization of an AO system

Even though AO is a technique that proved to be efficient, it cannot provide a full correction. As mentioned in the previous sections, the different elements of an AO system introduce noises. The quality of the correction also depends on the model used for the reconstruction of the wavefront and the resulting DM commands. Therefore an AO system only partially corrects the wavefront. The overall residual error (σ^2_{res}) can be expressed as the sum of the individual errors,

$$\sigma^2_{res} = \sigma^2_{ani} + \sigma^2_{chr} + \sigma^2_{scin} + \sigma^2_{al} + \sigma^2_{noise} + \sigma^2_{fit} + \sigma^2_{servo} + \sigma^2_{cal} + \sigma^2_{NCPA}$$

Those errors can be sorted into three main groups:

- Atmosphere model errors: errors due to the knowledge and modeling of the turbulence.
- System component errors: errors associated with the choice of the AO system components that can be limited by technology advancement and/or budgeting constraints.
- System operation errors: errors linked to the AO system operation and interaction with the telescope and instruments.

1.5.1 Errors due to the turbulence modelisation (σ^2_{ani},σ^2_{chr},σ^2_{scin})

As developed in Section 1.1, the model describing the atmospheric turbulence is based on some assumptions and is only valid within certain limits. When using a guide star, located some distance away from the scientific object of interest, an error due to anisoplanatism (σ^2_{ani}) appears. As described in Section 1.2.2.3, the separation between the guide star and the science target results in a difference of light path through the turbulent layers of the atmosphere. Hence what we measure on the guide star is not exactly what is needed to correct for the science object. The greater the angle between the guide star and the science target, the higher the error of anisoplanatism under similar turbulence condition. In the case of natural guide stars (NGS), it is a significant error. The number of available stars providing a high enough signal to noise ratio (SN) for the WFS is limited, and hence the sky coverage for AO operation is reduced. For the best correction that the AO system can deliver, bright enough stars within the isoplanatic angle around the science target are needed. Using NGS further away from the science target increases the sky coverage at the expense of the correction quality. In order to increase the efficiency and sky coverage of AO systems, laser guide stars (LGS) have been developed.

In addition, the atmosphere refraction dependence on the wavelength induces a chromatism error (σ^2_{chr}). The measurements made by the WFS at a specific wavelength do not represent exactly the wavefront distortion seen by the instrument at a different wavelength.

Moreover an AO system only corrects for the phase fluctuations and does not correct for the scintillation effect which remains as a source of error (σ^2_{scin}). The centroid calculation by the WFS assumes amplitude homogeneity, hence the scintillation also affects the WFS measurements. This problem has been addressed by Mahé et al. (2005) for point source objects and Robert et al. (2006) for extended objects.

1.5.2 Errors associated with the AO system components (σ^2_{al},σ^2_{noise},σ^2_{fit},σ^2_{servo})

First, there is the error due to measurements by the WFS, the aliasing error (σ^2_{al}) and the noise error (σ^2_{noise}). If we take the example of the SHWFS (Section 1.4.1), the aliasing error is due to the spatial sampling of the wavefront by the lenslet array. This spatial sampling results in a periodic signal in the Fourier space causing the aliasing of frequencies higher than $\frac{1}{2d}$, with d the lenslet sampling pitch. In addition, poorer sampled high frequencies are also responsible for aliasing onto the low frequency range. σ^2_{al} depends both on the characteristics of the WFS and the high frequency spectrum of the turbulence. Poyneer & Macintosh (2004) and Fusco et al. (2005) show that this error can be reduced by filtering the high frequencies before the WFS measurements. The noise error includes the photon noise and the detector noise that were discussed in Section 1.4.1. It is also dependent on the command law used for the reconstruction that will define how the error propagates towards the computation of the DM commands.

The second intrinsic error to the AO system is the fitting error (σ^2_{fit}). For all wavefront measurements, the DM cannot reproduce all of the deformation. It is limited to a number of Zernike modes (or spatial frequencies), determined by its number of actuators, and amplitude of its stroke. One can evaluate this error if the number of Zernike modes effectively corrected is known.

Finally, the AO system also suffers from a servo-lag error (σ^2_{servo}). There is a time lag between the WFS measurement and the actual correction by the DM, resulting in a correction which is not exactly compensating the incoming wavefront at the time of correction. This error decreases for higher coherence time of the turbulence and/or for higher frequency of the control loop.

1.5.3 Errors linked to the AO system operation (σ^2_{cal},σ^2_{NCPA})

The calibration error (σ^2_{cal}) includes all errors associated with the construction of the interaction matrix from the zero point slopes of the WFS to the models used in the command law. Those

errors can be difficult to estimate.

The non-common path aberrations (σ^2_{NCPA}) are linked to the non-common optical path between the sensing channel and the science ones. Those comprise both the aberration located downstream from the beam splitter on the sensing channel and on the science channel. The first ones are seen by the WFS and compensated for on the DM while they do not actually affect the science channel. The second ones affect the science channel but are not seen by the WFS and hence are not compensated for. Those aberrations are usually static or slowly variable. They can be estimated and corrected via the phase diversity method (Blanc et al., 2003; Sauvage et al., 2006).

When designing an AO system, one has to trade off between all of those errors. Increasing the number of sub-apertures lowers σ^2_{fit} but increases σ^2_{noise} and σ^2_{servo}. Ideally, one will try to keep them as low as possible and avoid having one dominating over the others. The constraints that one needs to consider when dimensioning an AO system are the scientific needs, the atmospheric turbulence conditions at the telescope site, the type of AO system component available and the system interactions with the telescope and instrument.

1.6 AO-corrected image, performance metrics

The PSF of an AO-corrected image does not have the same characteristics as that of a seeing-limited image. There have been extensive studies on the topic (Roddier & Roddier, 1981; Conan et al., 1994; Lardiere et al., 2004), and I only describe the main points here. On a short exposure image, the PSF consists of a central peak surrounded by residual speckle. The residual speckles are due the uncorrected turbulence. The speckles position and intensity vary in time, leading to an uncorrected seeing limited halo surrounding the central peak, in long exposure imaging. I will give more details about the PSF shape in Ch. 4.

Different metrics are required in order to evaluate the correction quality of an AO system. The most commonly used criteria is the residual variance of the phase on the corrected wavefront. However, this is not the most suited parameter to describe the image quality on the science channel. There is a number of metric that can be used to describe the science image quality. The choice of metric will be mostly dependent on the science that one wants to do and/or the instrument used. Those metrics include:

- **The full width at half maximum (FWHM)**: It is a measure of the PSF width at half its peak intensity. It is mainly used for general characterization of the image quality. For imaging instruments, especially in the case of partial correction. It has the advantage to describe the overall shape and possible dissymmetry.

- **The Strehl Ratio (SR)**: It measures the ratio of the peak intensity of the corrected image over the theoretical diffraction limited one. It is a metric well suited in the case of very high correction aiming to reach close to diffraction limited images, as well as very high contrast imaging.

- **The Encircled Energy (EE)**: This gives the fraction of the total energy encompassed within a given area. It can be a circular area around the PSF peak, in which case we talk about encircled energy (later refer as EE) but it could also be within a slit, in which case we talk about enslited energy (later refer as ESE). One could also consider a square area associated with the ensquared energy. This metric is mostly used for spectroscopy when the instrument is usually fed by either a slit or fiber.

For the AO simulation study in Ch.4, I will consider the EE and ESE metric as I will focus on the enhancement of SALT spectroscopic performances thanks to AO correction.

1.7 Conclusions

In this chapter, I have established the context and theoretical background for the work I am presenting in this thesis. In Ch. 2 I will present the study of the Sutherland site atmospheric turbulence characterization, based on the theory presented in Section 1.1 and 1.2 and data collected with the instruments presented in Section 1.3. In Ch. 3 I present the work that I did towards the development of a new instrument, the "Profileur de Bord Lunaire" (PBL, Profiler of Moon Limb in English). The main purpose of this instrument is to improve on the altitude-resolution of the turbulence profile as compared to the already existing devices. Finally, in Ch. 4, I present a study exploring the potential improvements that an AO system could bring to SALT. For this part, I ran simulations to explore the performances of different system setups. I chose specific configurations using different values for the parameters presented in Section 1.4 and then evaluate the system performances based on the appropriate metrics (Section 1.6).

Chapter 2

SUTHERLAND SITE SEEING MONITORING

Contents

Over the past 20 years, atmospheric site characterization and seeing monitoring for all major astronomical observatories has come into common usage (Els et al., 2009; Chun et al., 2009; Vernin & Munoz-Tunon, 1994). Extensively used in the process of sites selection (IAU Symposium no.19, 1962; Coulman, 1985), suites of seeing and turbulence profiler instruments are now part of the standard operation at most of the major astronomical sites. In addition, to provide valuable information for post-observation data processing and analysis, this continuous monitoring became critical for telescope time optimization in the era of queue-scheduled observations (Sarazin, 1997). Moreover, the increasing use of adaptive optics (AO) systems (Babcock, 1953; Rigaut, 1992), and the need for better corrections also calls for more accurate and extensive characterization of the atmospheric turbulence at astronomical sites.

The first historical report of seeing conditions at Sutherland was made by Harding (1974) and indicated 69% of the nights had seeing better than 0.8" from visual observations [1]. Seeing measurements by Warner (1994), also based on eye estimation made during slit-scanning photometry of double stars observations between 1972 and 1994, reported 53% of the nights had seeing better

[1]The seeing reported in Harding (1974) was converted to FWHM by Warner (1994)

than 0.8". Due to the methodology used, it is difficult to evaluate the reliability of these measurements to compare to later quantitative results given by dedicated seeing monitors. From February 1992 to May 1993, seeing measurements were carried out using a trailed photographic technique and were reported in Gochermann et al. (1999). These results gave a median seeing of 1.23", but were subject to wind effects. Differential Image Motion Monitor (DIMM, Sarazin 1986a; Sarazin & Roddier 1990) observations were first obtained from April 1994 to February 1998. The system was based on that of Wood et al. (1995). These results were reported in Erasmus (2000) and indicated that the median seeing value for this period was 0.92" and the first and third quartiles were, respectively, 0.74" and 1.16" (Erasmus, 2000). A site testing campaign, using two DIMM instruments to select the final site for SALT, was done from December 1998 to March 2000. The results showed similar statistics with a median value of 0.95", and first and third quartiles of 0.79" and 1.18" (Erasmus, 2000). The seeing conditions measured over the period from April 1994 to February 1998 showed significant correlation with the wind speed and direction (Erasmus, 2000). South-Easterly winds brought poorer conditions while the best seeing values were observed for westerly winds. Also, worse seeing values tended to be associated with higher wind speed. The seeing conditions showed a very small dependence on the seasons. Observations during the SALT site testing campaign verified these correlations (Erasmus, 2000).

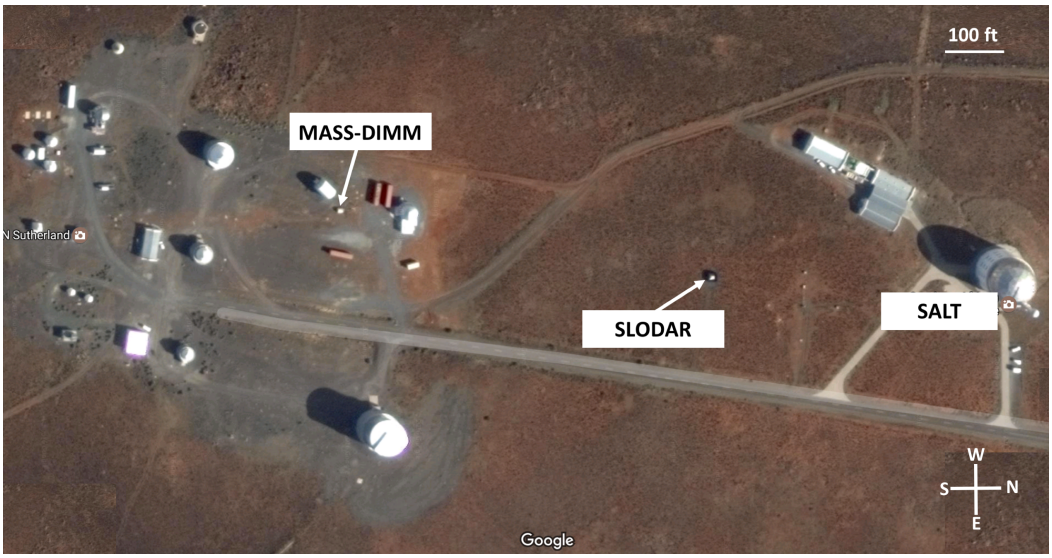

Figure 2.1: *Sutherland site and the seeing monitoring instruments location.*

Considering the topography together with wind speed and directions at different altitudes, the main contributions to the turbulence were expected to be the surface layer up to 1 km, a wind shear layer around 3 km, and one between 10 and 12 km due to the jet stream (Erasmus, 2000). Some information about the turbulence profile were obtained from a 40 min scan from a classical SCIDAR (SCIntillation Detection And Ranging, Vernin & Roddier 1973) and microthermal measurements from a 30 m mast gave more information about the turbulence profile. The SCIDAR scan showed 3 strong layers at the ground level, around 3 km and 12 km. Based on the microthermal data, Erasmus (2000) found that the first 30 m of the ground layer (GL) were contributing only 7.3% of the overall turbulence with a seeing of 0.19".

With currently 15 telescopes in use on the plateau, among which the Southern African Large Telescope (SALT) operating on queue-scheduled mode, Sutherland had a clear need for a dedicated device providing continuous monitoring of the seeing. In order to provide real-time observing conditions on the Sutherland plateau a MASS-DIMM, associating a Multi-Aperture Scintillation Sensor (MASS) and a Differential Image Motion Monitor (DIMM) in a single device, has been set up and commissioned in March 2010. The system was further developed to a semi-automated state in 2012 and is now in operation every night SALT is open for observations.

In the framework of this thesis, I have been using the data provided by the Sutherland MASS-DIMM in order to extensively characterize the atmospheric turbulence and seeing conditions at Sutherland. This study complements previous studies with up-to-date general seeing statistics and an additional low altitude resolution profile, lacking from the historical site selection data. In addition, during the year 2010, a SLOpe Detection And Ranging (SLODAR) instrument and a secondary DIMM instrument (hereafter referred as TimDIMM) have been used along with the MASS-DIMM, providing additional information. This chapter contains a review of the Sutherland seeing instruments setup and operation and presents the results of 5 years of seeing monitoring.

2.1 The Sutherland site monitoring setup

The Sutherland instruments working principle, setup, operation and data processing are described in this section, along with a summary of the observing periods for the different instruments. The location of the different seeing instruments on the plateau can be seen in Fig. 2.1.

2.1.1 SLODAR

2.1.1.1 Location and general setup

The SLODAR was located approximately 100 m South-East from the SALT building. It used a 40 cm aperture diameter telescope mounted on an equatorial pier at ground level. The system was in a dome enclosure protected by a 2-meter high windscreen.

2.1.1.2 Operation and control

The SLODAR was set up by R. Wilson and T. Butterley and operated from the University of Durham. The Sutherland setup uses an 8x8 Shack-Hartmann wavefront sensor with 5 cm size sub-apertures. With the system being fully robotic, it was operated from Durham, for the first 4 hours of the night, on each night when weather conditions allowed. More details on the operation and control are given in Wilson et al. (2009), which describes a similar setup of the instrument at Cerro Paranal. The higher vertical resolution of the Sutherland setup was achieved by using a CCD with a larger area that allowed a wider separation of the double stars. The resolution ranges from 55 to 80 meters, varying with star separation and elevation angle. Due to the wider separation, the maximum sensing altitude is around 500 m instead of 1 km on a regular setup.

2.1.1.3 Data processing

The SLODAR data were processed as extensively detailed in Wilson et al. (2009). However, the profile reconstruction model was modified and for the Sutherland data set is done using the "Mk II" analysis mentioned in Wilson et al. (2011). The "Mk II" analysis fits an extra turbulence component at the ground with a non-Kolmogorov power spectrum in order to account for dome/tube seeing. This component is also subtracted from the centroid autocovariance prior to fitting for r_0 to give an estimate of the total seeing that has been corrected for dome seeing.

2.1.2 TimDIMM

From July 2010 to January 2011 the TimDIMM was operated as a secondary DIMM instrument side by side with the MASS-DIMM. In February 2011, the CCD was migrated to the DIMM part of the MASS-DIMM to replace the SBIG-ST5, and the software was upgraded to handle the overall operation of the MASS-DIMM.

2.1.2.1 Location and general setup

The TimDIMM is located in the DIMM building next to the Monet-South telescope building, some 300 m South-East from the SALT. The system used a standard DIMM configuration (Sarazin & Roddier, 1990) on a 25 cm LX200-GPS Meade telescope mounted on the standard Meade tripod with an Alt-Az fork mount. The entrance aperture of the telescope lay at approximately 1.5 m from the ground. The detector used was an IEEE1394 camera from Point Grey Research (specifically, a Grasshopper GRAS-03K2M) which is capable of frame rates up to 200 Hz (full frame 640x480 pixels with no binning). A frame rate of 330 frames/sec with 2x2 binning is used in normal TimDIMM operations for additional speed and sensitivity.

2.1.2.2 Operation and control

The system's pointing and tracking, as well as the real-time data analysis process are fully automated. The observing protocol is set so that the system selects targets with zenith angle less than 45^o and a magnitude less than 3. The system acquires 10000 frames to produce a seeing measurement. This provides a new seeing value every 30 seconds when running at the standard rate of 330 frames/sec and a 1 to 3 ms exposure time.

2.1.2.3 Data processing

A software was developed for the processing of the TimDIMM data. This software is based on the theory and formulas described in detail in Tokovinin et al. (2002). The centroids of the stellar images are calculated via intensity-weighted moments within a 20x20 pixel box with a threshold set to 3σ above the measured background noise in the image. Only pixels with signal above the threshold are included in the centroiding calculations. The weighted variance of the longitudinal differential motion is calculated using the signal-to-noise ratios as weights. We are not currently calculating the transverse variance, which is more sensitive to bias from wind smoothing (Kornilov & Safonov, 2011). The formal uncertainties in the centroids are used to determine the variance due to measurement uncertainty. This is then used to determine a corrected variance from which a seeing value is derived. Also, we are not applying an exposure time correction. With 1–3 ms exposures (depending on the star's brightness) and a 3 ms cadence, we have found it largely unnecessary.

2.1.3 MASS-DIMM

2.1.3.1 Location and general setup

The MASS-DIMM is located in the DIMM building next to the Monet-South telescope building, some 300 m South-East from the SALT. The system uses a 25 cm LX200GPS Meade telescope. From March 2010 to February 2011 it was mounted on the standard Meade tripod with an Alt-Az mount. Later, the mount was replaced by an Astro-Physics 900GTO equatorial mount and bolted directly to a steel pier. In both configurations the entrance aperture of the telescope lies between 1 and 1,5 m from the ground.

2.1.3.2 Operation and control

The MASS-DIMM in its first configuration (February 2010 to January 2011) was operated manually. The tracking was handled by the standard Meade Autostar II control system. The MASS data were handled by the Turbina 2.06 software (Kornilov et al., 2003). The DIMM imaging was done by an SBIG-ST5 CCD and the data were processed by the CTIO RoboDIMM software (Tokovinin et al., 2002). In January 2011, the alt-az mount was replaced by the equatorial one. From February 2011 onward, the Point Grey IEEE1394 camera was migrated over from TimDIMM and replaced the ST5 on the MASS-DIMM. The TimDIMM software was updated to manage and

control the entire MASS-DIMM system, including DIMM data acquisition and processing, handling telescope pointing and tracking, conducting the initialization and remote operation of the Turbina software and archiving of all seeing data. In addition, in August 2012 we installed a new version of the Atmos algorithm (atmos 2.98.8), allowing up to 15 layers in the turbulence profile restoration (Kornilov & Kornilov, 2011).

Apart from roof opening, the MASS-DIMM has been working in fully robotic operation since March 2011. On all clear nights, the system was operated by one of the SALT operators.

In summary, the current system is made up of a 25 cm telescope on an equatorial pier at ground level, the entrance aperture of the telescope being at approximately 1 m from the ground. Targets are automatically selected to have a magnitude lower than 3 and a zenith angle less than 45^o. The MASS data are processed by the Turbina 2.06 software , and the DIMM data are managed by the TimDIMM software, which also controls the whole system. All of the data, raw and reprocessed, are stored within the SALT Science Archive.

2.1.3.3 Data processing

Table 2.1: *DIMM data reprocessing thresholds.*

	Threshold parameter	Discrimination value
MASS	Flux in D channel	> 50
	Flux error	< 0.01
	χ^2	< 100
	S_A^2	< 0.7
DIMM	Number of rejected frames	< 50
	S/N	> 5

Prior to using the TimDIMM setup on the DIMM channel of the MASS-DIMM, the DIMM data were handled by the CTIO RoboDIMM software. A description of the latest version is given in Tokovinin et al. (2002), although we used a former version, Robodimmnet 1.4. In this configuration, the DIMM frame rate was set to 2 and 4 ms exposure time, allowing a correction of the finite exposure time to the zero exposure time, as described in Tokovinin (2002). The latest configuration uses the TimDIMM setup described in the previous section.

The MASS data are acquired by the Turbina software and reprocessed by the Atmos algorithm (Kornilov & Shatsky, 2005). The Atmos algorithm fits the measured SI and DSI to atmospheric models, assuming Kolmogorov turbulence, in order to restore the fixed and floating layers turbulence profile (Kornilov & Shatsky (2005) 5.1.2.10).

The first data set, up to August 2012, was processed with the original version of the atmos algorithm, using 6 fixed layers at 0.5,1,2,4,8 and 16 km, for the profiles reconstruction. Later on, we used the latest version of the atmos algorithm (2.98.8), allowing for a higher altitude resolution in the restoration of the turbulence profiles. I also reprocessed all the former data with the new version of atmos and new altitude grid. In this study I used 13 fixed layers at 0.3,0.5,0.75,1,1.5,2,3,4,6,8,12,16 and 24 km.

Concerning the data acquisition, the PMTs have a 1 ms exposure time. Scintillation indices and statistical moments of the photon counts are calculated over a base-time of 1 sec, corresponding to a thousand 1 ms samples. Those values are then averaged over a 1 min accumulation time, corresponding to 60 data point. After each accumulation time, atmospheric parameters are calculated from the SI, DSI and their respective errors, and then stored in the output file (Tokovinin et al., 2003b).

Previous studies of MASS and DIMM data quality indicate that data of low quality should be rejected (Kornilov et al., 2007; Wang et al., 2006). For DIMM data, the criteria are the number of frames per integration time (1 min) and the signal-to-noise ratio (S/N) of the star images. For

MASS data, I considered the flux in channel D, the error on the flux measurement, the scintillation in channel A, and the χ^2 of the restored profiles. A summary of the chosen threshold values is given in Table 2.1. I chose the threshold levels in agreement with those indicated in Kornilov et al. (2007), except for the flux level in channel D. The flux threshold accounts for clouds and target lost due to tracking error, Kornilov et al. (2007) indicates to choose a threshold of a minimum of 100 counts. However, measurements with counts in channel D as low as 50 are consistent with the rest of the data set from the same run. Hence, I chose to apply a threshold of 50 for the flux. The limit on the χ^2 value allows to keep only data for which the reconstruction of the TP is accurate, and the threshold on the SI value suppresses data taken under strong scintillation for which the MASS measurements are not accurate (Tokovinin et al., 2003b). In order to be able to get a reliable value for the ground layer from differential DIMM and MASS measurements, I set the maximum value of S_A^2 to 0.7 as indicated in Kornilov et al. (2007). The percentage of data rejected for each threshold never exceeds 5%, and the parameters values obtained from the raw data are within ± 6% of the ones obtained from the "cleaned" data. For DIMM data, a flux threshold is also applied to each aperture along with a threshold on the number of frames used to calculate the variance of the differential image motion. This avoids biasing due to low signal-to-noise and helps to keep the statistics representative by maintaining a minimum number of samples per measurement.

2.1.4 Observing periods

Those 5 years of seeing monitoring were conducted with several instruments that were operating at different periods, locations, and with different telescopes. Table 2.2 gives an overview of the different operation schedules for each instrument. Simultaneous operation of the SLODAR and MASS-DIMM were carried out over a period of 10 nights in March 2010. Also, from August 2010 to early January 2011, more DIMM than MASS data have been taken. This is due to the fact that the TimDIMM was set to be remotely controlled, while the MASS-DIMM still required manual operation. Only the TimDIMM was operated for most of the nights through this period. Data from June and October 2010 were included in the statistics for July and November respectively. Only a few nights were observed during those months, and these nights were at the beginning or the end of the month. For all measurements after September 2013, we only have DIMM data as the MASS channel was deactivated after misfunctioning.

2.2 Data Analysis and Consistency

2.2.1 Data Analysis Method

For the purpose of data analysis, I defined the free atmosphere (FA) as all layers above 1 km. I re-derive the FA seeing from the C_n^2 profile measured by the MASS considering only the layers at and above 1 km and excluding the measurements at 300, 500 and 750 m from MASS, which are known to be less accurately restored (Tokovinin et al., 2005). However, the atmos software, which computes the MASS atmospheric profile, uses triangular weighting functions to define the altitudes of the layers. Fig. 2.2 shows those weighting functions for the 2 configurations of altitude grid, 6 layers (top) and 13 layers (bottom). Due to the layer boundaries not being sharply defined, the reported C_n^2 value at a given altitude will include contributions from a range of heights. For example, the 1 km layer includes contributions from turbulence located between 750 m and 1.5 km. As such, any turbulence measured by MASS at a specific altitude is a weighted average of turbulence measured over the altitude range of the triangular weighting function. For simplicity in the rest of this study, I will use 1 km as the boundary for the FA, but keeping in mind that this limit is only approximate.

Defining the GL-FA boundary at 1 km requires a re-binning (in terms of altitude and time) of

Table 2.2: *Observing periods with the Sutherland seeing monitoring instruments. The telescope diameter and DIMM sub-apertures diameter (d) and separation (s) are given in parenthesis as well as operating and data processing software.*

	SLODAR (40 cm)		**MASS-DIMM (25 cm - d=8 cm, s=17 cm)**						**secondary DIMM (25 cm - d=5 cm, s=15 cm)**	
			MASS		DIMM (CTIO RoboDIMM)		DIMM (TimDIMM)		(TimDIMM)	
Dates	# of nights	# of data	# of nights	# of data	# of nights	# of data	# of nights	# of data	# of nights	# of data
February 2010	8	1355	–	–	–	–	–	–	–	–
March 2010	16	2534	8	2108	8	2260	–	–	–	–
April 2010	4	646	20	7094	20	7817	–	–	–	–
May 2010	–	–	4	1180	4	1230	–	–	–	–
June 2010	–	–	1	–	1	–	–	–	–	–
July 2010	–	–	10	3983	7	2199	–	–	3	1272
August 2010	–	–	4	980	–	–	–	–	8	3990
September 2010	–	–	–	–	–	–	–	–	18	8436
October 2010	–	–	–	–	–	–	–	–	3	–
November 2010	–	–	1	239	–	–	–	–	14	7980
December 2010	–	–	2	614	–	–	–	–	14	2909
January 2011	–	–	16	4889	–	–	–	–	21	7500
February 2011	–	–	14	4277	–	–	14	7045	–	–
March 2011	–	–	11	3818	–	–	11	6001	–	–
April 2011	–	–	21	7423	–	–	21	11716	–	–
May 2011	–	–	16	6276	–	–	16	10525	–	–
June 2011	–	–	12	4807	–	–	12	8050	–	–
July 2011	–	–	23	11436	–	–	23	19451	–	–
August 2011	–	–	21	6716	–	–	21	12617	–	–
September 2011	–	–	25	10709	–	–	25	16295	–	–
October 2011	–	–	22	5877	–	–	20	9982	–	–
November 2011	–	–	13	5591	–	–	21	8674	–	–
December 2011	–	–	26	6691	–	–	26	9456	–	–
January 2012	–	–	25	8091	–	–	25	12059	–	–
February 2012	–	–	24	8896	–	–	24	12925	–	–
March 2012	–	–	16	7985	–	–	26	13066	–	–
April 2012	–	–	22	6999	–	–	22	11881	–	–
May 2012	–	–	18	8097	–	–	25	16442	–	–
June 2012	–	–	17	7007	–	–	16	9713	–	–
July 2012	–	–	18	7206	–	–	17	10211	–	–
August 2012	–	–	7	1788	–	–	8	4138	–	–
September 2012	–	–	–	–	–	–	24	15234	–	–
October 2012	–	–	3	610	–	–	19	8463	–	–
November 2012	–	–	21	2940	–	–	19	8716	–	–
December 2012	–	–	7	464	–	–	20	6793	–	–
January 2013	–	–	17	2966	–	–	25	11283	–	–
February 2013	–	–	23	4109	–	–	22	12201	–	–
March 2013	–	–	15	3371	–	–	25	12604	–	–
April 2013	–	–	–	–	–	–	24	12194	–	–
May 2013	–	–	7	1407	–	–	14	5881	–	–
June 2013	–	–	14	2174	–	–	13	2941	–	–
July 2013	–	–	15	2762	–	–	16	8183	–	–
August 2013	–	–	11	2575	–	–	11	6101	–	–
September 2013	–	–	3	611	–	–	6	2768	–	–
October 2013	–	–	–	–	–	–	13	4543	–	–
November 2013	–	–	–	–	–	–	15	4907	–	–
December 2013	–	–	–	–	–	–	23	6263	–	–
January 2014	–	–	–	–	–	–	20	6194	–	–
February 2014	–	–	–	–	–	–	23	7236	–	–
March 2014	–	–	–	–	–	–	25	11827	–	–
April 2014	–	–			–	–	16	6520	–	–
May 2014	–	–			–	–	15	4061	–	–
June 2014	–	–			–	–	8	2690	–	–
July 2014	–	–			–	–	12	2129	–	–
August 2014	–	–			–	–	10	543	–	–
September 2014	–	–			–	–	11	2318	–	–
October 2014	–	–			–	–	6	899	–	–
November 2014	–	–			–	–	9	1214	–	–
December 2014	–	–			–	–	14	1564	–	–
January 2015	–	–			–	–	5	791	–	–
February 2015	–	–			–	–	17	2787	–	–
March 2015	–	–			–	–	24	3672	–	–
April 2015	–	–			–	–	19	3947	–	–
May 2015	–	–			–	–	20	4666	–	–
June 2015	–	–			–	–	16	4139	–	–
July 2015	–	–			–	–	9	2261	–	–
August 2015	–	–			–	–	12	2202	–	–
September 2015	–	–			–	–	5	881	–	–
October 2015	–	–			–	–	19	3218	–	–
November 2015	–	–			–	–	24	2650	–	–

the data from the MASS-DIMM. The total integrated turbulence profile is given by:

$$J = \int_0^\infty C_n^2(h)dh. \tag{2.1}$$

The integrated turbulence profile can be given for different parts of the atmosphere by integrating $C_n^2(h)$ over different heights. For example, J^{500} is given by integrating between 300 m and 750 m using the triangular weighting function. J^{MASS} is the sum of all layer contributions, $J^{300} + J^{500} + J^{750} + J^1 + J^{1.5} + J^2 + J^3 + J^4 + J^6 + J^8 + J^{12} + J^{16} + J^{24}$. The model gives a discrete representation of the turbulence which is in reality continuously distributed. If the real turbulence is at an altitude located in between two of the predefined layers altitude, it will be redistributed between those 2 adjacent layers through the triangular weighting functions (Fig. 2.2). It is shown in section 6.2 of Tokovinin et al. (2003b) that the redistribution induces errors on the individual layers contribution, reaching 20% in the worst cases for the lower 500 m and 1 km layers, but is typically between 5 to 10% for the overall contribution, J^{MASS}. Despite differences in the distribution of the turbulence in the lower layers (below 2 km), errors due to layer redistribution are of the same order with the latest Atmos algorithm as shown in section 8 of Kornilov & Kornilov (2011). The seeing in arcseconds for a given layer is just obtained through the following relation: $\epsilon = J^{3/5} \times 5.307\lambda^{-1/5} \times 206265$, where λ is in m and J is in $m^{1/3}$.

To determine the free atmosphere seeing, we must subtract the turbulence contribution of the 300, 500 and 750 m layers from the overall MASS turbulence, then calculate the corresponding seeing. Using MASS profiles, the FA seeing (ϵ^{FA}) is given by:

$$\epsilon^{FA} = [J^{MASS} - J^{300} - J^{500} - J^{750}]^{3/5} \times 5.307\lambda^{-1/5} \times 206265. \tag{2.2}$$

The GL seeing is then calculated as follow, after the 10 min binning:

$$\epsilon^{GL} = [(\epsilon^{DIMM})^{5/3} - (\epsilon^{FA})^{5/3}]^{3/5}. \tag{2.3}$$

In addition, it has been shown that the coherence time, as measured by MASS, is underestimated (Tokovinin & Kornilov, 2007). I corrected this bias by applying the compensation given by equation (5) in Tokovinin & Kornilov (2007):

$$\tau_0^{-5/3} = (C.\tau_{MASS})^{-5/3} + 0.057^{-5/3}\lambda_0^{-2}V_{GL}^{5/3}J^{GL}, \tag{2.4}$$

where τ_{MASS} is the value given by the MASS, λ_0 is the wavelength (500 nm), V_{GL} is the ground layer wind speed obtained from the 30 m high probe on the weather mast (5.1 $m.s^{-1}$) and J^{GL} is the strength of the turbulence in the ground layer, derived from $'DIMM-MASS'$. C is a correction coefficient, whose value is determined empirically with fairly low accuracy. Tokovinin found a value of 1.27, however, he also mentioned a value of 1.7 and 1.73 found by Travouillon et al. (2009) and Kornilov (2011) as well as values varying between 2 and 2.5 found with comparative data at Cerro Tololo and Paranal. For the present study, I will use $C = 1.73$, given in Kornilov (2011), as it is the most commonly used, and in particular for the TMT site testing. This gives us a consistent comparison between the Sutherland site and other sites around the world, keeping in mind that the accuracy of the method is ± 20%.

In terms of qualitative analysis, for the overall statistics on integrated parameters ($\epsilon_0, \tau_0, \theta_0$), I defined best seeing conditions to be the first quartile of the seeing distribution, median conditions corresponds to the 25% around the median value, and bad conditions will be the fourth quartile of the seeing distribution.

For the overall profile analysis, I considered the 10 layers from 1 km and above as the FA contribution. The GL was split into 4 layers, the 300, 500 and 750 m layers given by MASS and a layer at 100 m given by the difference between DIMM and MASS seeing. The altitude of the later layer was determined based on the SLODAR ground layer data. I calculated the

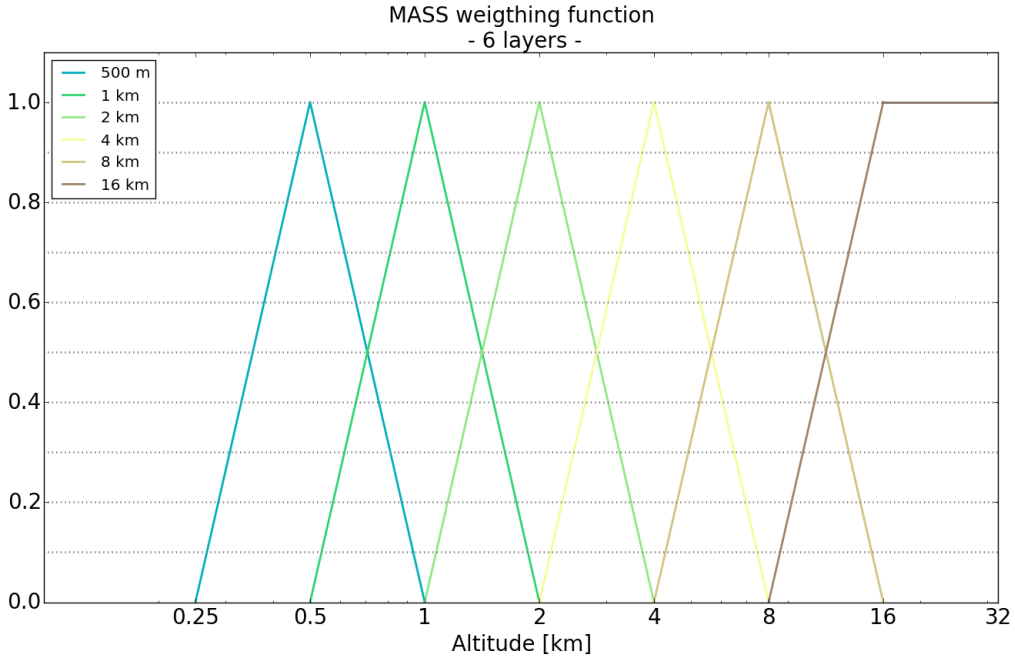

(a)

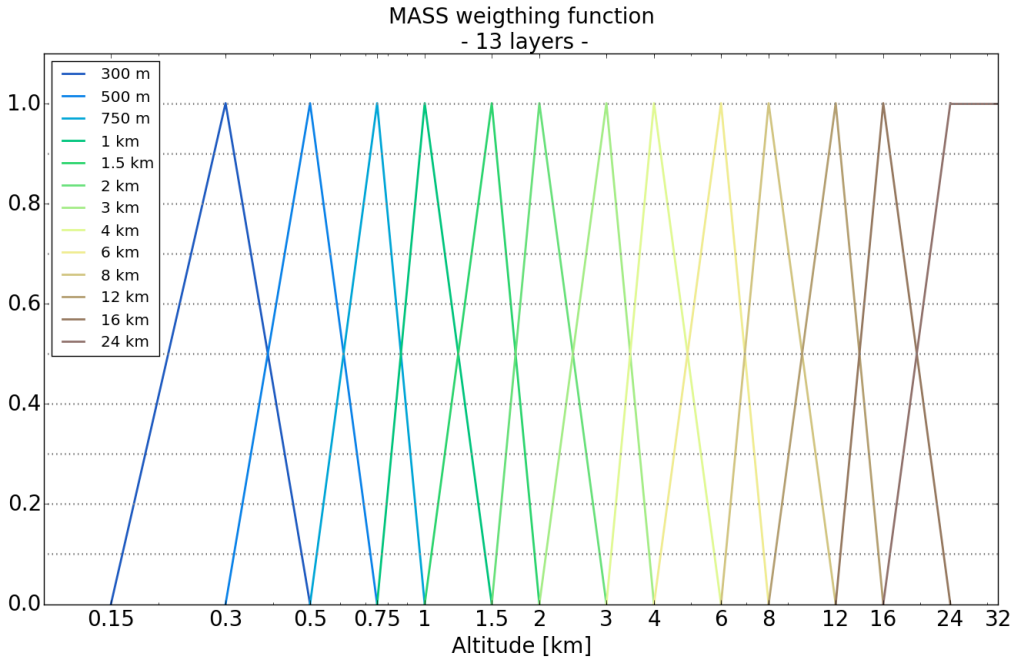

(b)

Figure 2.2: *MASS weighting function for profiles reconstruction. Left: Reconstruction altitudes for the original atmos algorithm for fixed layers at 0.5,1,2,4,8 and 16 km. Right: Reconstruction altitudes for the new version of atmos (2.98.8) for fixed layers at 0.3,0.5,0.75,1,1.5,2,3,4,6,8,12,16 and 24 km.*

average altitude (h_{eq}) of the lower part, below 250 m, of the SLODAR turbulence, weighted by the turbulence strength at each altitude, $h_{eq} = \frac{\sum h_i . J_i}{\sum J_i}$, which gives a value of 83 m. For simplicity, and since the calculation only gives a rough estimation of the equivalent altitude of the lower layer, I positioned it at 100 m. As for the GL profiles from SLODAR I also need to determine each layer altitude. Indeed, SLODAR profiles give the turbulence strength for 7 layers whose

altitudes vary with both the separation and zenith angle of the observed double star. Hence, when extracting typical SLODAR profiles, I determined their layer altitude by taking a weighted average, $h^{layer} = \frac{\sum h_i^{layer} . J_i^{layer}}{\sum J_i^{layer}}$.

Based on similar studies in the literature (Els et al., 2009; Egner et al., 2007), I defined "Good" profiles to be associated with r_0 values within the 20-30% interval of its cumulative distribution. "Median" profiles correspond to the 45-55% interval and "Bad" to the 70-80% interval.

2.2.2 Data consistency

2.2.2.1 MASS vs. DIMM

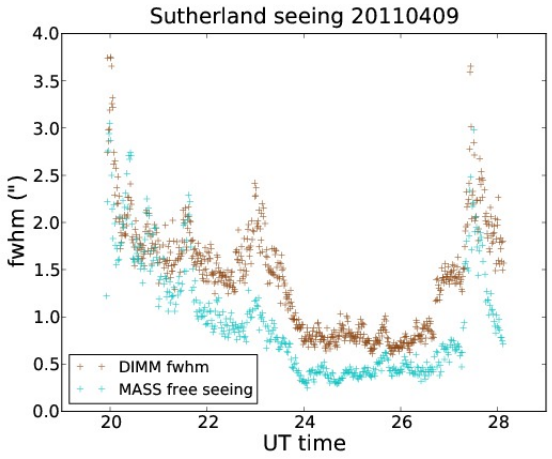

Figure 2.3: *An example of the nightly variation of the overall seeing measured by DIMM (brown crosses) and the seeing measured by MASS from layers above 500 m (blue crosses).*

Despite using two different technologies for measuring the seeing, the DIMM and the MASS show consistent behaviour throughout a typical night. An example of this is given in Fig. 2.3. As expected, $\epsilon^{DIMM} \geq \epsilon^{MASS}$, since the DIMM is measuring the overall seeing while the MASS is only measuring the FA seeing. However, on nights when the FA is dominant and one would expect $\epsilon^{MASS} \approx \epsilon^{DIMM}$, ϵ^{MASS} can be $> \epsilon^{DIMM}$ due to the overestimation of the contribution of the lower layers to the MASS seeing (Tokovinin et al., 2005).

2.2.2.2 DIMM vs. SLODAR

As confirmation of the reliability of the seeing monitors, I compared seeing values as measured by the DIMM and the SLODAR. In order to do so, only data from overlapping observing periods have been considered. In addition, data have been binned and averaged over 10 minute periods to account for non-simultaneity of the measurements. The overall correlation between DIMM and SLODAR seeing values can be seen in Fig. 2.4. Each night is represented by a different data point and color. Despite a high dispersion on certain nights, the DIMM and SLODAR measurements are reasonably well correlated: the Pearson correlation coefficient, which measures linear relationships, is 0.69. A possible explanation for the differences between the instruments seen on any given night may be due to the different optical paths observed by each instrument as they were separated by 200 m on the plateau and were not targeting the same star. In addition, the tendency of DIMM to give higher values can be explained by dome/tube seeing which, as mentioned in Section 2.1.1.3, has been removed from SLODAR measurements while it could still be affecting DIMM ones.

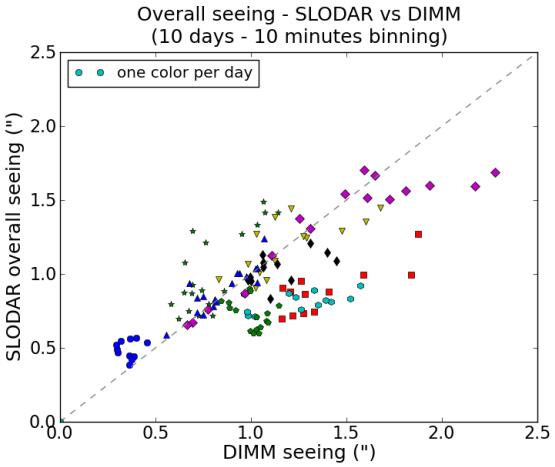

Figure 2.4: *Comparison of the overall seeing value as measured by the DIMM and the SLODAR. Different data points and colors indicate different observing nights.*

2.2.2.3 MASS 6 layers vs. 13 layers restoration method

In 2011 a new version of the Atmos software has been released by the MASS team (Kornilov & Kornilov, 2011). The new processing method provides the possibility to reconstruct profiles up to 15 layers instead of the original 6 layers in the former version of the software. Before implementing the new version of the software in the data pre-processing I did a comparison between the two methods to ensure they were consistent. I reanalyzed the old data to obtain higher altitude resolution profiles for all the data set.

2.3 Results

2.3.1 General statistics of the seeing

I used all of the DIMM data obtained with both MASS-DIMM (until July 2010) and TimDIMM (afterwards) with no temporal averaging to compute the median seeing for the site. The statistics for this present study are made of 4535 SLODAR data points, 142886 MASS data points and 464186 DIMM data points, taken over a period of 5 years from March 2010 to November 2015 and covering a total of 1107 nights. The median seeing value over the entire period is 1.51".

Using only the measurements for which both MASS and DIMM data are available, I looked at the contribution from the FA and the GL to the overall seeing. Distributions of the seeing values associated with each of these three components are shown in Fig. 2.5. To compare the MASS and DIMM measurements, I have averaged the data over 10 minute periods as explained in Section 2.2.1. After averaging, we end up with a total of 16860 data points observed over 561 days from March 2010 to September 2013. For this data set, the median overall seeing was 1.49" (Fig. 2.5, a), the median FA seeing was 0.42" (Fig. 2.5, b) and the median GL seeing was 1.34" (Fig. 2.5, c).

In order to investigate seasonal trends, I plotted the median seeing for each individual month from June 2010 to November 2015 in the top graph of Fig. 2.6. There we can see a clear pattern of the seeing getting worse over the winter months (June, July, August) and some extension into spring (September, October, November) shown in shaded blue and green respectively. For the past 2 years, we also started to see a peak in the seeing value around January during summer, shown in shaded yellow. I will discuss further the possible reasons for this trend when looking at correlations of the seeing and weather parameters later in this section. Now if we look at the global seasonal trend by regrouping all data from the same month together, as shown in the bottom graph of Fig. 2.6, the trend is not as clearly visible. We can notice, however, that winter has indeed the

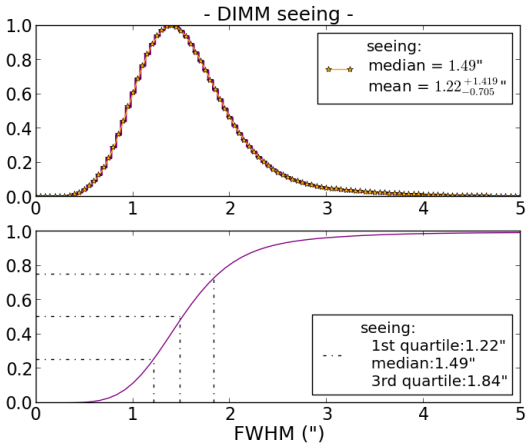

(a)

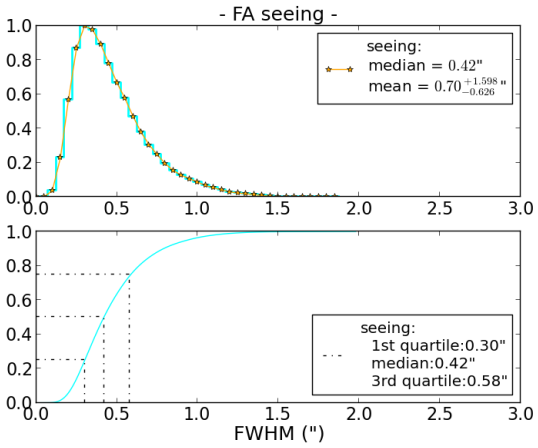

(b)

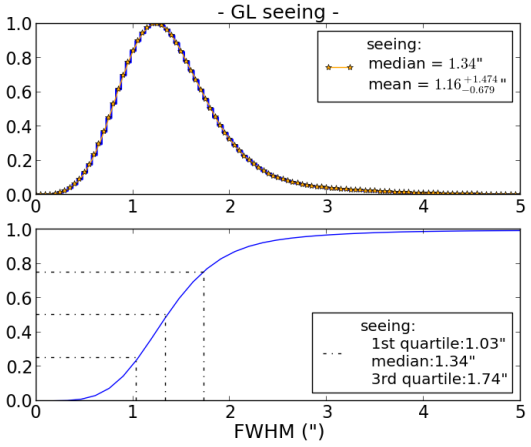

(c)

Figure 2.5: *5 years of statistics of the seeing at the Sutherland site. Data from MASS-DIMM measurements, with a limit between GL and FA defined to be at 1km above ground level. All data have been averaged over 10 min. (a) Overall seeing as measured from DIMM. (b) Free-atmosphere seeing from MASS. (c) Ground-layer seeing derive from the difference between DIMM and MASS.*

highest averaged seeing value (1.63"). On the other hand, the summer months present the widest distribution of seeing value, with a tale of bad seeing conditions, greater than 2.5" for the worst 10% of the distribution.

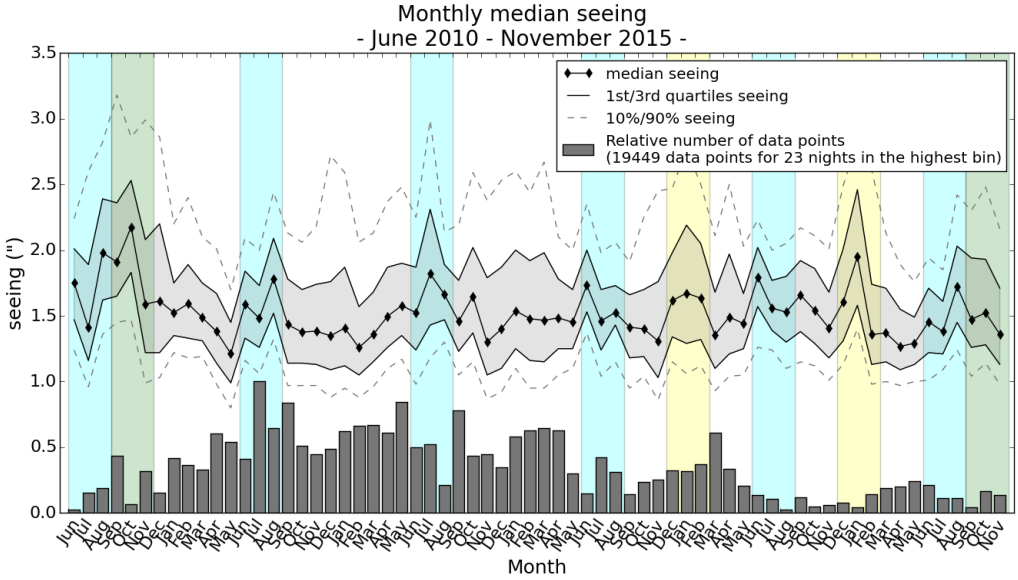

(a)

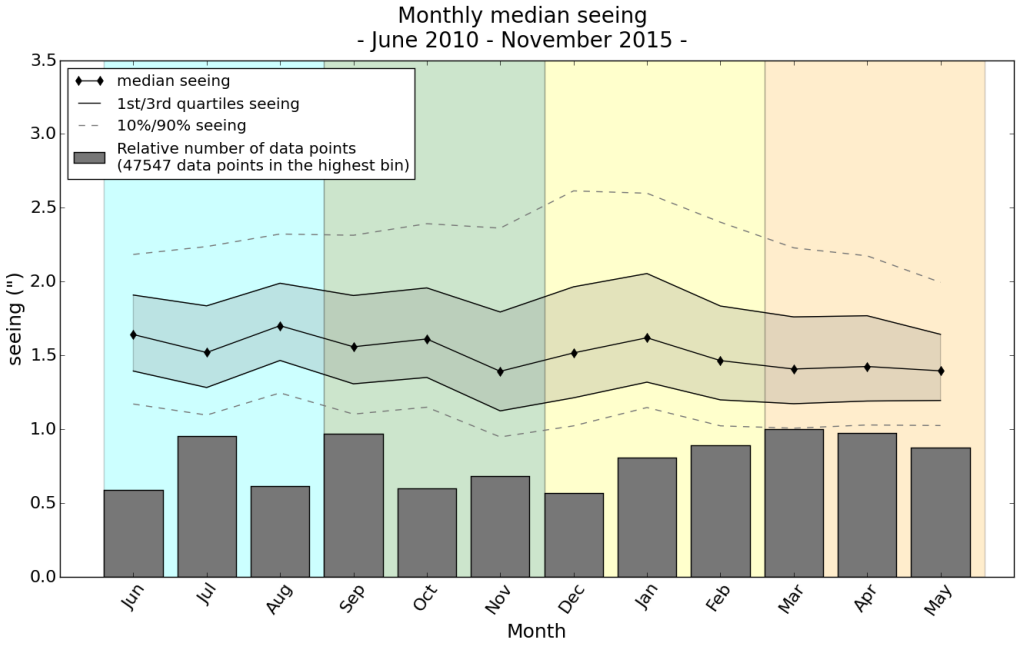

(b)

Figure 2.6: *Seasonal trend of the seeing from DIMM measurements. The top graph shows the median seeing value for each month from June 2010 to November 2015. Seasons for which a peak in the seeing value was observed are highlighted with shaded colors (blue:winter, green:spring, yellow:summer). The bottom graph shows the monthly averaged median seeing for the same period. The seasons are delimited with the shaded colors, winter in blue, spring in green, summer in yellow and autumn in orange. For both graphs, the solid line with diamonds gives the median seeing. The shaded grey section gives the 1st and 3rd quartile limits, while the dotted lines give the 10% and 90% limits of the seeing distribution. The grey bars represent the relative number of data points for each month.*

I also investigated seeing evolution throughout the night. In order to avoid seasonal bias I first split the data set per month. For each month, accumulating data over the 5 years of measurements, I plotted the median seeing per hour. The hourly trend of the seeing is shown in Fig. 2.7. From this figure, there is no clear trend of seeing variation through the night, which suggest relatively stable conditions throughout the night, within ± 0.2" in average.

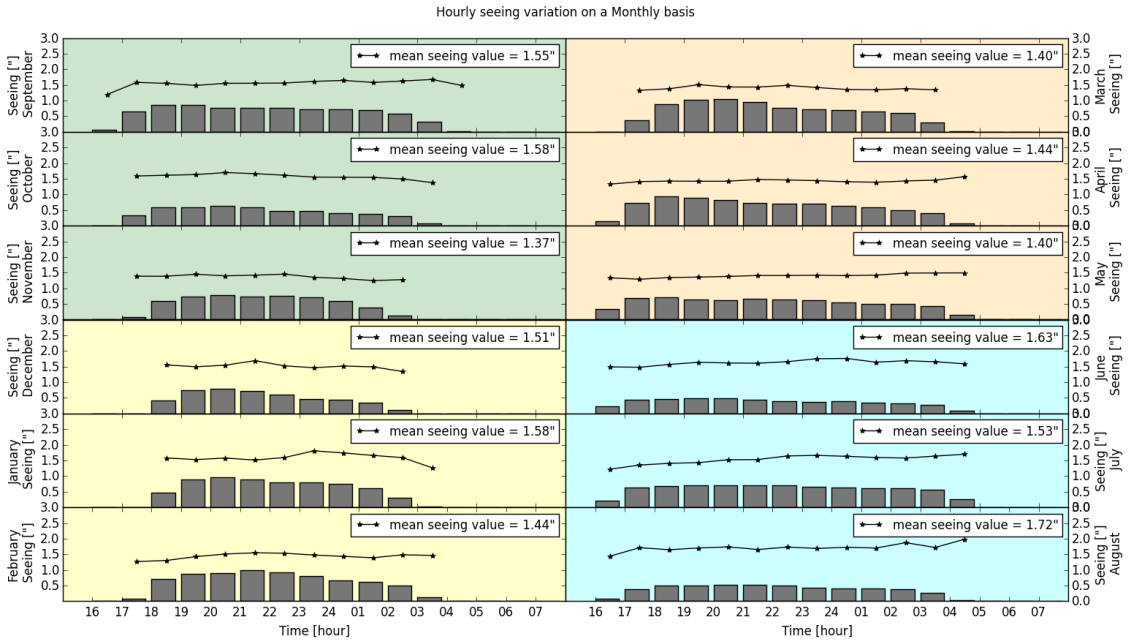

Figure 2.7: *Hourly seeing variation from DIMM measurements. For each month, accumulating data over the 5 years, I plotted the night variation of the seeing one hour at a time. The shaded colors delimit the seasons, Spring in green, Summer in yellow, Autumn in orange and Winter in blue. I also give the median seeing value for each month and the grey bars represent the relative number of data points for each time intervals.*

2.3.2 Isoplanatic angle and coherence time

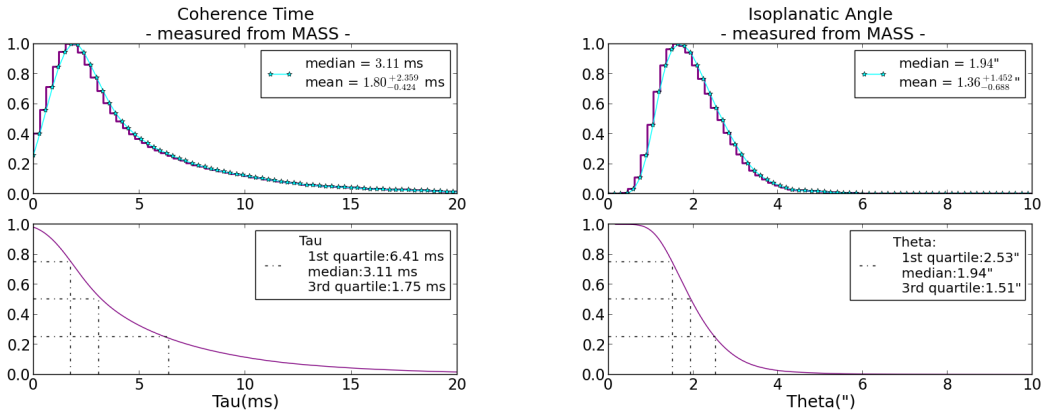

(a) (b)

Figure 2.8: *5 years of statistics of the coherence time of the turbulence (a) and the isoplanatic angle (b), as measured by the MASS instrument.*

In addition to the seeing value the MASS provides also a measurement of both the coherence time (τ_0) and the isoplanatic angle (θ_0). General statistics of those two parameters are represented

in Fig. 2.8. The median value of the coherence time (τ_0) at Sutherland, as given from the MASS instrument, is 3.11 ms, the first and third quartiles are respectively 6.41 and 1.75 ms. However, as explained in Section 2.2.1, we need to apply a correction due to an under-estimation inherent to the MASS measurement method. Results before and after applying the correction are presented in Table 2.3. After correction, the median value, first and third quartiles of the coherence time at Sutherland are respectively 5.38, 11.01 and 3.03 ms. I also looked at the coherence time value under good seeing conditions, for the ϵ_0 best 5% and 20% values. I found, respectively, a 26.78 ms and 12.99 ms coherence time. Comparison values from 12 other sites are given in Table 2.8 and further discussed in Section 2.4.2.

Table 2.3: *Coherence time at Sutherland. Value given by the MASS instrument (τ_0^{MASS}) and corrected value (τ_0^{corr}). The correction uses C = 1.73 and the GL contribution via J_{GL} in equation (4). The wind speed was obtained from the weather mast data 30 m probe ($5.1 m.s^{-1}$).*

	median	25%	75%	ϵ_0 best 5%	ϵ_0 best 20%
τ_0^{MASS} [ms]	3.11	6.41	1.75	15.48	7.51
J_{GL} [10^{-13} $m^{1/3}$] (DIMM-MASS)	8.99	5.88	14.02	0.32	4.92
τ_0^{corr} [ms] ($MASS_{corr}$+GL)	5.38	11.01	3.03	26.78	12.99

The isoplanatic angle median value at Sutherland is 1.94". The values for 12 comparison sites are listed in Table 2.8. The first and third quartiles values are respectively 2.53" and 1.51", which gives a range of 1.02" between the best 25% and 75%. This is similar to all sites apart from Mauna Kea and Mount Graham spanning over a 2" range with best 25% of respectively 3.61" and 3.6" (TMT site selection team, 2008; Vázquez-Ramió et al., 2012).

2.3.3 Atmospheric turbulence profiles

2.3.3.1 Turbulence profiles from MASS-DIMM

Table 2.4: *Contribution of the different layers for the median profile (solid line in Fig. 2.9-b)*

	altitude	layer contribution		seeing
FA	24 km	1.41%	16.4%	0.42"
	16 km	0.32%		
	12 km	0.6%		
	8 km	0.4%		
	6 km	0.27%		
	4 km	1.58%		
	3 km	3.94%		
	2 km	4.1%		
	1.5 km	2.6%		
	1 km	1.15%		
GL	750 m	1.53%	83.6%	1.34"
	500 m	1.29%		
	300 m	6.74%		
	100 m	70.07%		
Overall				1.49"

In addition to the integrated parameters, the MASS-DIMM also provides measurements of the turbulence profile. Fig. 2.9 shows the typical turbulence profiles at the Sutherland site. Fig. 2.9 (a) gives the median, first and third quartile values of the cumulative distribution of each layer independently. In Fig. 2.9 (b) I represent the profiles as selected by their associated r_0 value according to the pre-defined intervals for "Good", "Median" and "Bad" seeing (Section 2.2.1).

Fig. 2.9 (a) only gives the median profile and the range of turbulence strength for each layer with the first and third quartile values. While less representative of realistic profiles, due to the fact that it is unlikely to be in a configuration where all layers will be in their best condition or worse condition simultaneously, this representation is relevant for site comparison purpose.

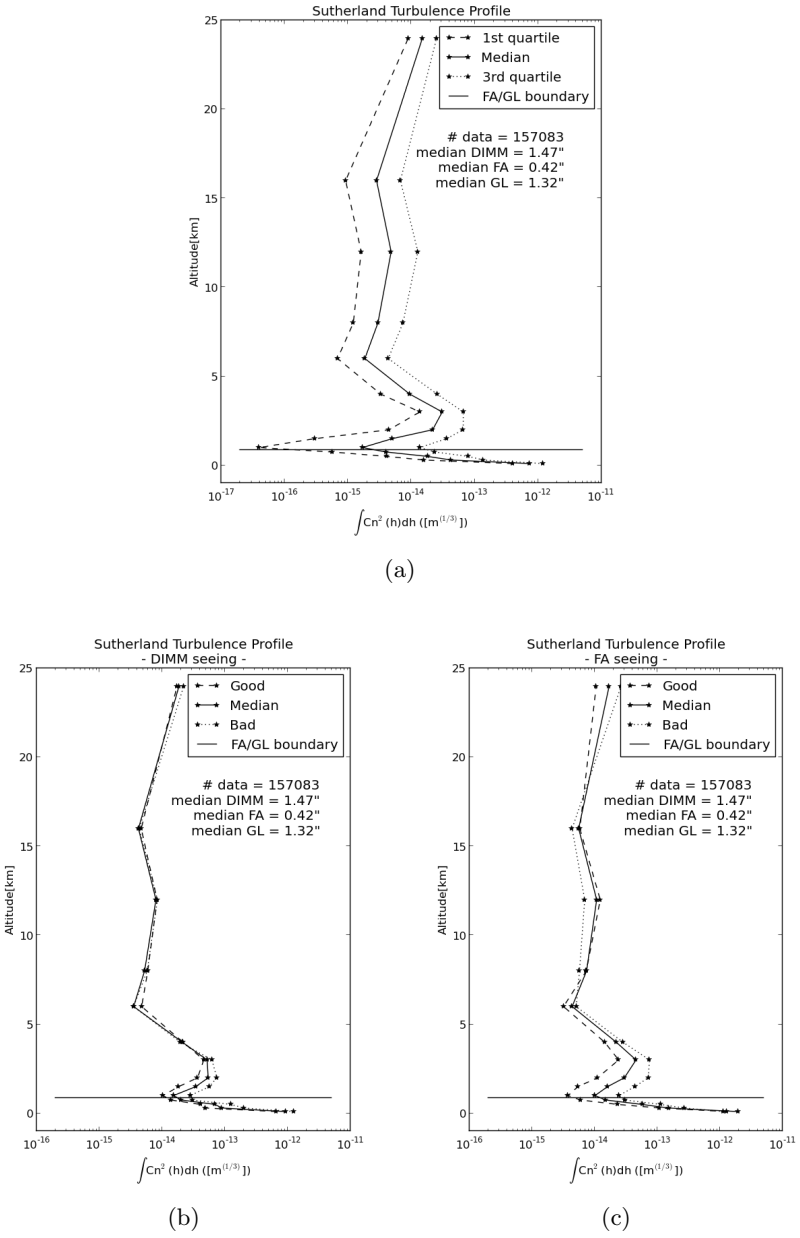

Figure 2.9: *Turbulence profiles from MASS-DIMM: (a) gives the median (solid line), first (dashed line) and third quartile (dotted line) values of the turbulence strength for each layer independently. (b) represents the typical profiles under "median" (solid line), "good" (dashed line) and "bad" (dotted line) seeing conditions. "Good", "median" and "bad" are defined as the 20-30%, 45-55% and 70-80% ranges of the respective cumulative distribution of ϵ_0 from DIMM. (c) is similar to (b) but using the FA seeing value distribution rather than the DIMM one.*

Table 2.5: *Contribution of the different layers for the median profile for each season.*

		Seasonal Influence											
		Summer			Autumn			Winter			Spring		
	altitude	layer contribution		seeing	layer contribution		seeing	layer contribution		seeing			
FA	24 km	1.82%	22.52%	0.48”	1.18%	14.67%	0.4”	1.25%	13.31%	0.39”	1.59%	16.99%	0.42”
	16 km	0.23%			0.27%			0.42%			0.34%		
	12 km	0.31%			0.61%			0.82%			0.53%		
	8 km	0.42%			0.48%			0.51%			0.28%		
	6 km	0.2%			0.32%			0.24%			0.23%		
	4 km	0.95%			1.59%			1.96%			1.77%		
	3 km	4.01%			3.76%			3.86%			4.4%		
	2 km	7.13%			3.36%			2.56%			4.09%		
	1.5 km	5.32%			2.05%			1.16%			2.55%		
	1 km	2.13%			1.06%			0.5%			1.2%		
GL	750 m	2.9%	77.48%	1.22”	1.23%	85.32	1.26”	0.65%	86.69%	1.5”	1.9%	83.01%	1.23”
	500 m	11.84%			3.51%			1.78%			6.35%		
	300 m	10.6%			5.92%			3.86%			8.54%		
	100 m	52.14%			74.65%			80.39%			66.22%		
Overall				1.43”			1.4”			1.63”			1.4”

Fig. 2.9 (b) and (c) are more relevant plots in terms of site characterization as it gives the typical profiles corresponding to "good", "bad", and "median" seeing conditions, based on the overall seeing value (Fig. 2.9 (b)) and the FA seeing value (Fig. 2.9 (c)). One can see that, as the seeing degrades, the 4 GL layers at 100, 300, 500 and 750 m, and the first FA layers, up to 3 km, become more turbulent. While having a weaker contribution to the overall turbulence, the higher layers from 4 km and above remain, overall, fairly similar under all seeing conditions. However, the layers from 8 to 16 km appears to be more turbulent under good seeing than for median and bad seeing. The overall contribution of the GL increases as the overall seeing degrades, being 81% under good seeing conditions (dashed line), 84% under median seeing (solid line) and 85% under bad seeing (dotted line). On the other hand, as the overall seeing degrades, the contribution of the FA decreases. This confirms that the overall seeing value is mainly driven by the GL seeing conditions.

Now looking at the profiles change as a function of the FA seeing distribution (Fig. 2.9 (c)), it appears that while the GL contribution as well as the 8 to 16 km section decreases as the FA seeing degrades, the 1.5 to 4 km section and the top 24 km and higher increases. This suggests that the FA turbulence is mainly driven by a wind shear layer around 3 km and the jet stream layer above 24 km. This is a fairly typical behavior seen at many other astronomical sites.

Also, while the distribution between the four GL layers does not change much between good and median seeing conditions, it varies significantly under bad seeing conditions. Under good and median seeing conditions the 100 m layer contributes around 87% to the GL turbulence and the upper layers only 13%. While under bad seeing conditions there is a shift of the turbulence towards the higher layers of the GL, the 100 contribution is down to 78% while the upper layer contribution goes up to 22%. As the seeing degrades the upper GL layers contribute more to the GL turbulence. I will discuss this point further in Section 2.3.3.2 with the results of the GL profiles from SLODAR.

Overall, based on the comparison of three typical profiles under good, median and bad seeing, one can conclude that the seeing value is mainly driven by the ground layer turbulence and to a weaker extent by the wind shear layer in the free atmosphere located around 3 km. The contribution from the different layers under median seeing conditions is summarized in Table 2.4. More details about the GL turbulence distribution were obtained thanks to the SLODAR. I discuss those results in the next section.

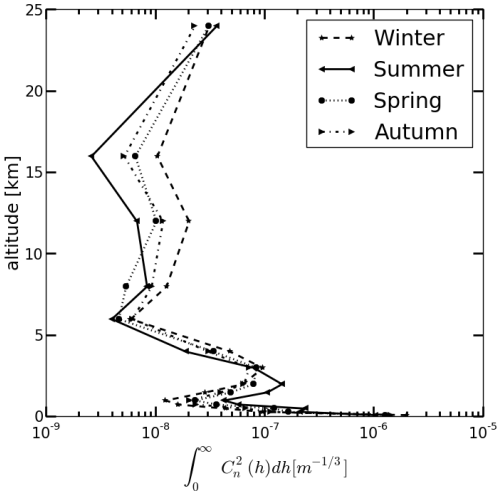

Figure 2.10: *Seasonal Profiles. Median profile of the turbulence for each season.*

Moreover, since I noticed a seasonal trend when analyzing the overall seeing behavior, I looked at seasonal profiles to see where the seeing degradation in winter is coming from. Fig. 2.10 shows the median profiles based on the overall seeing value for all 4 seasons. In addition, I summarized the layers contribution to the turbulence under median seeing conditions in Table 2.5. From this table and comparing it to the general profile values in Table 2.4, one can see that Autumn and Spring profile are very similar to the general profile. On the other hand, both Summer and Winter show noticeable differences. In winter the 100 m layer in the GL contributes 80% to the turbulence, which is 10% more than the typical conditions. As we saw earlier, an increase in the GL contribution is associated with worse seeing, and in fact, winter months show degraded seeing conditions as compared to the overall median value. For the summer months, with a low GL contribution, one would expect better seeing than in Spring and Autumn, however, the seeing is slightly worse. This can be explained by noticing a stronger than average turbulence in the 1.5 to 3 km layers. This burst of turbulence in the lower FA could also explain the peak in the seeing value that was observed over the past 2 years around January.

2.3.3.2 Ground layer turbulence profiles from SLODAR

From the 27 nights of SLODAR measurements, I extracted the typical GL profiles. Similarly to the profiles from MASS-DIMM I have represented the median, first and third quartiles for each layer independently on Fig. 2.11 (a), similar as to the measurements for Mauna Kea by Chun et al. (2009). Fig. 2.11 (b) shows the profiles corresponding to "good", "median" and "bad" seeing condition with the same intervals as used for the MASS-DIMM profiles, but here using only the GL seeing value rather than the overall seeing. This method is similar to the measurements of Mount Graham by Masciadri et al. (2010).

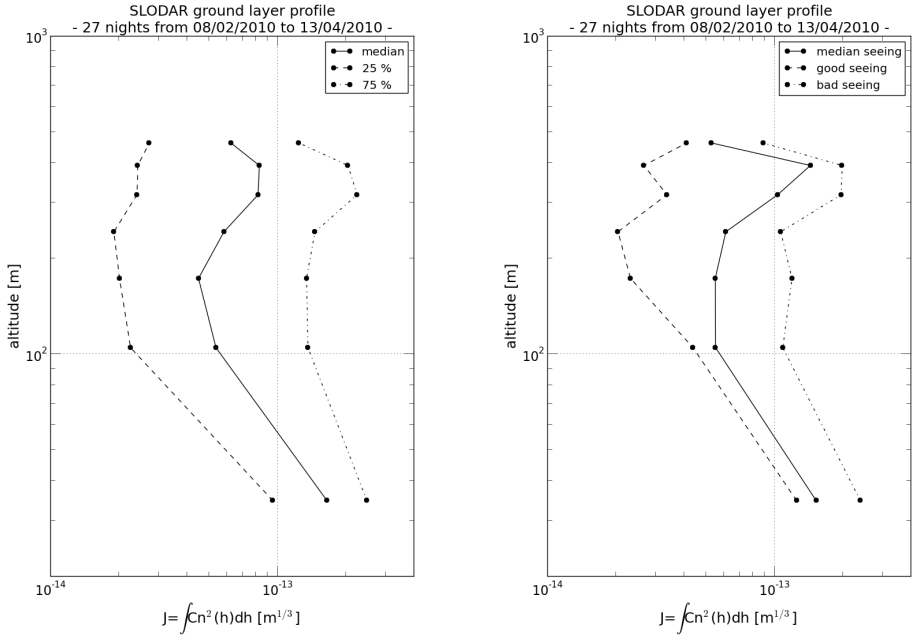

Figure 2.11: *GL turbulence profiles from SLODAR, based on 28 nights of data between February and April 2010. (a) gives the median (solid line), first (dashed line) and third quartile (dotted line) values of the turbulence strength for each layer independently. (b) are the typical profiles under "median" (solid line), "good" (dashed line) and "bad" (dotted line) GL seeing conditions. "median", "good" and "bad" are defined as the 45-55%, 20-30% and 70-80% ranges of the cumulative distribution of* ϵ_0^{GL}.

Table 2.6: *Contribution of the different layers for the GL median profile from SLODAR (solid line in Fig. 2.11-b)*

layer altitude	layer contribution
35 m	24.5%
105 m	8.8%
173 m	8.8%
243 m	9.8%
318 m	16.6%
393 m	23.1%
462 m	8.4%

I examined the contribution from each layer for the profiles associated with the median seeing conditions represented as a solid line in Fig. 2.11 (b) and summarized in Table 2.6. It appears that the first layer at 35 m contributes nearly 25% of the GL seeing while approximately 50% is contributed by layers above 300 m. On the other hand, under good seeing conditions nearly 40% of the turbulence is within the first 30 m while the upper layers are much weaker, particularly the 400 m that is less than 10% of the turbulence. Under bad seeing the contribution of the lower 30 m goes down to 20% and the 300 to 500 m contribute around 45%, while the contribution from the intermediate layers, 100 to 300 m, increases to 30%. The degradation in the GL seeing corresponds to the increasing turbulence in the upper layers. This is in good agreement with the earlier observations from MASS-DIMM profiles which show an increase of the upper GL contribution as the seeing degrades.

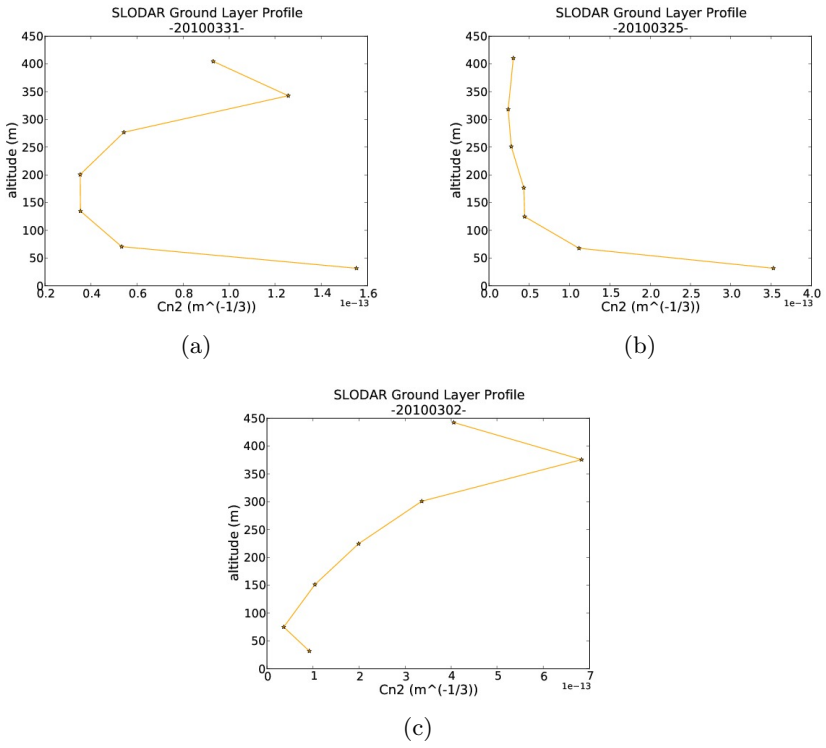

Figure 2.12: *Daily GL turbulence profile from SLODAR. (a): 31/03/2010. (b): 25/03/2010. (c): 02/03/2010.*

This median profile is consistent with the observed daily profiles, which present 3 typical behaviour illustrated by the nights presented in Fig. 2.12. On the first night (31/03/2010, (a)), both a strong lower layer and a strong upper layer are observed, while intermediate layers are much

weaker. The second night (25/03/2010, (b)) is dominated by the lowest layers, and the third night (02/03/2010, (c)) has a turbulence profile dominated by the upper layers. This third case is observed in lower proportions, 14 % of the time, compare to the other two, 47 and 39 % for (a) and (b) respectively.

In Section 2.4.2, I will discuss the GL profile at Sutherland as compared to profiles at other sites.

2.3.4 Correlation of seeing with the weather conditions

To see how the weather conditions influence the seeing, I compare the seeing measurements with data from the SALT weather station, which provided wind speed and direction at 10 and 30 m above ground, relative humidity level, and temperatures at 2,5,10,15,20,25,30 meter above ground. Previous studies (Erasmus, 2000) showed that the wind was the main weather component influencing the seeing conditions. In examining the current weather data, I do find a strong correlation with wind direction, a weak correlation with wind speed, and I find no correlation with the temperature or relative humidity.

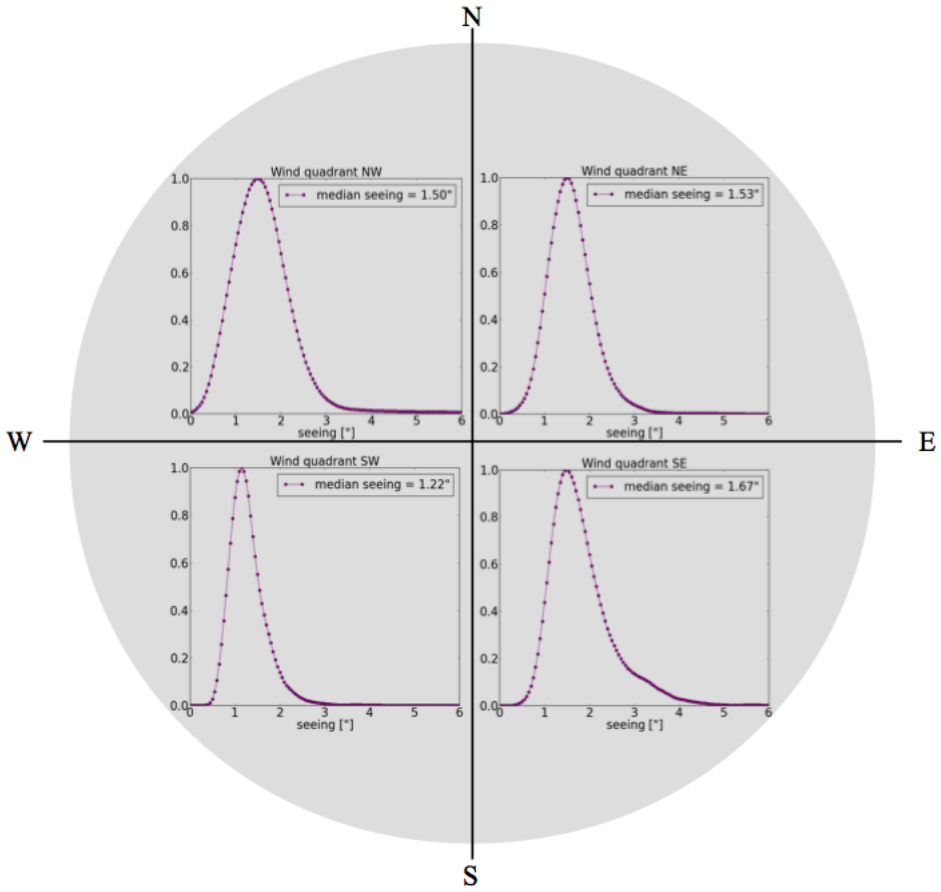

Figure 2.13: *Seeing statistics as a function of wind direction. The number of data points (after 10 min average) for each quadrant are 5732, 2529, 5564 and 3035 for NW, NE, SE and SW respectively.*

2.3.4.1 Influence of the wind direction

In order to determine the influence of wind direction on the seeing value I first split the data set according to four wind direction quadrant: westerly to northerly winds, northerly to easterly winds,

easterly to southerly and southerly to westerly winds. I show in Fig. 2.13 the seeing distribution for each quadrant. We can see that the overall seeing is worse for south-easterly winds while better for south-westerly winds. This latter direction is rarely seen at the Sutherland site and is hence not statistically relevant. I present a more detailed view of the correlation between the wind direction and the seeing in Fig. 2.14.

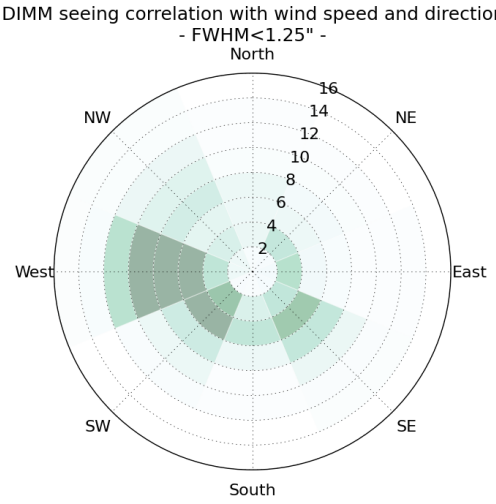

(a)

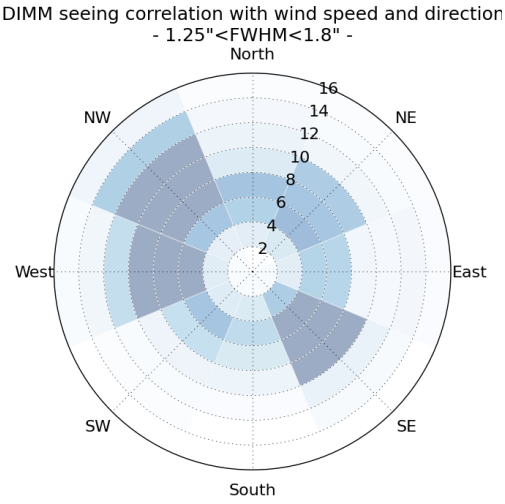

(b)

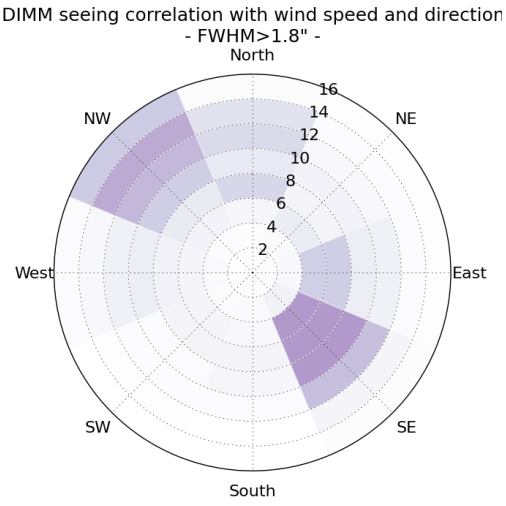

(c)

Figure 2.14: *Correlation of the seeing with wind direction and speed. In all three figures, the angle corresponds to the wind direction, the radius gives the wind speed in m/s, and the color gradient gives the density of data points. a) Good seeing conditions:* $\epsilon_0 \leq 1.25"$*, corresponding to the first quartile. b) Median seeing conditions:* $1.25" \leq \epsilon_0 \leq 1.8"$*. c) bad seeing conditions:* $\epsilon_0 \geq 1.8"$*, corresponding to the third quartile.*

Fig. 2.14 presents the correlation of the seeing with wind speed and direction. I have plotted different cases corresponding to good seeing conditions (a), median seeing conditions (b), and bad seeing conditions (c). On the wind roses the angles indicate the wind direction and the radii the wind speed in m/s. After splitting the data according to their seeing value in the 3 different seeing conditions, I binned them within wind speed range of 2 m/s and wind directions range of 45^o. The color of each bin indicates the number of data within each bin, darker color indicating a higher number density of events. Looking at Fig. 2.14 (a), one can see that good seeing occurred predominantly under westerly winds, while Fig. 2.14 (c) shows that bad seeing happened when winds are coming from the South-East. Apart from the North-West and North-East directions, having a fairly similar contribution under all seeing conditions, we could split the roses in two: the South-West to North half and the North-East to South half. If we look at the South-West to North half, the contribution from those wind directions gets weaker as the seeing degrades. On the other hand, the North-East to South half direction contribute more and more with degrading seeing. It is clear here that as the wind turns West to South-East, the 2 predominant wind directions, the seeing degrades. Moreover, in the case of South-Easterly winds, one can notice, by comparing the second and third roses, that the seeing tend to get worse with higher wind speed. However, as we will see in the next section, this is a behavior that is only visible in the case of South-Easterly winds.

In addition I also looked at the influence of the wind direction on the profile of the turbulence. In Fig. 2.15 I have plotted the median profile associated with each wind direction, split between north-east (NE), south-east (SE), south-west (SW) and north-west (NW). The contribution of all layers is summarized in Table 2.7.

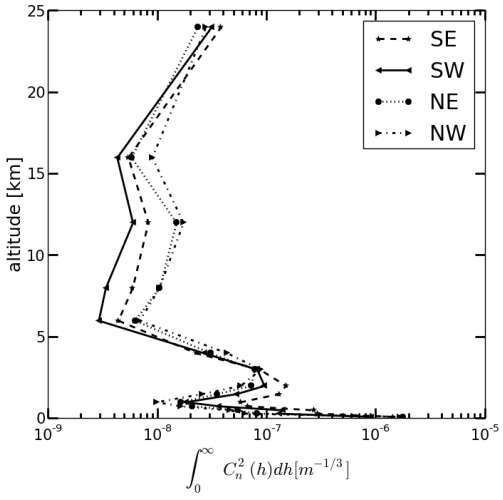

Figure 2.15: *Sutherland turbulence profiles as a function of wind direction.*

Comparing the dominant wind direction, NW and SE, we can see that the degradation of the seeing is present in both the GL and the FA. The seeing in the GL worsens and spreads towards the top layers of the GL (300 m, 500 m), however, it has a lower contribution to the overall turbulence since the turbulence in the FA also gets stronger. While the top layers of the FA stay relatively similar under all wind conditions, the 1 to the 3 km layers become more turbulent under SE wind conditions. The increase of turbulence in the top GL layers and the bottom FA ones associated with the seeing degradation under South-easterly winds is in agreement with the general analysis presented in Section 2.3.3.

Table 2.7: *Contribution of the different layers for the median profile associated with each wind direction.*

		Wind Direction Influence											
		NE			SE			SW			NW		
	altitude	layer contribution		seeing	layer contribution		seeing	layer contribution		seeing			
FA	24 km	1.05%	13.16%	0.39”	1.48%	19.77%	0.46”	2.05%	21.13%	0.43”	1.33%	14.2%	0.39”
	16 km	0.27%			0.21%			0.28%			0.43%		
	12 km	0.67%			0.32%			0.39%			0.83%		
	8 km	0.47%			0.23%			0.22%			0.5%		
	6 km	0.28%			0.17%			0.19%			0.33%		
	4 km	1.37%			0.88%			1.76%			2.09%		
	3 km	3.49%			3.36%			5.36%			4.23%		
	2 km	3.24%			5.83%			6.23%			2.77%		
	1.5 km	1.59%			5.05%			3.48%			1.23%		
	1 km	0.74%			2.24%			1.19%			0.47%		
GL	750 m	0.94%	86.84%	1.4”	2.60%	80.23	1.5”	2.39%	78.87%	1.05”	0.78%	85.8%	1.33”
	500 m	2.43%			10.51%			9.21%			2.2%		
	300 m	3.65%			11.38%			8.46%			3.02%		
	100 m	79.82%			55.75%			58.81%			79.8%		
Overall				1.53”			1.67”			1.22”			1.47”

2.3.4.2 Influence of the wind speed

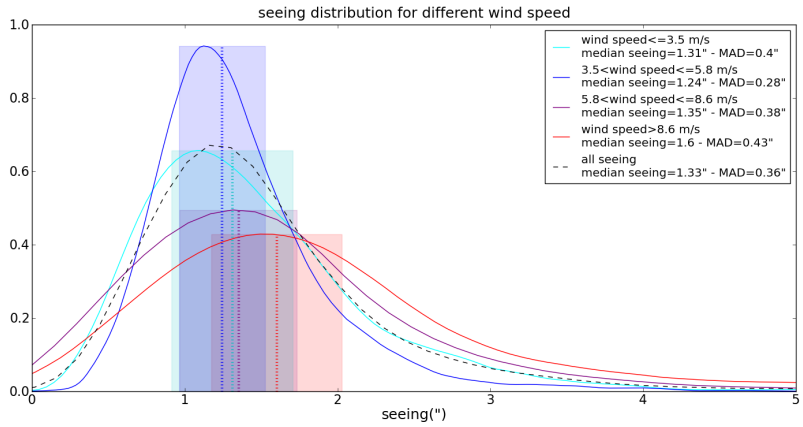

Figure 2.16: *Relation between wind speed and seeing values. Dark blue: seeing distribution for lowest wind speed (≤ 3.5 m/s). Light blue: seeing distribution for wind speed between 3.5 m/s and 5.8 m/s. Purple: seeing distribution for wind speed between 5.8 m/s and 8.6 m/s. Red: seeing distribution for highest wind speed (≥8.6 m/s). The dashed line is plotted as an indicator and is the seeing distribution for all data. For all curves, the dotted line shows the median value and the shaded area corresponds to the median average deviation (MAD).*

The median seeing for 4 different wind speed ranges, corresponding to <3.5 m/s, 3.5 to 5.8 m/s, 5.8 to 8.6 m/s, and >8.6 m/s are presented in Fig. 2.16. It is difficult to conclude that the wind speed has a very significant influence on the seeing. Better seeing was observed for wind speeds between 3.5 to 5.8 m/s (dark blue) than wind speed below 3.5 m/s (sky blue). On the other hand, the seeing does seem to degrade with stronger winds with wind speeds between 5.8 to 8.6 m/s (purple) and over 8.6 m/s (red). However, considering the large deviations on the data distribution, the shift towards worse seeing for high wind speeds is not very pronounced, and could be due to telescope shake or higher dome seeing rather than higher atmospheric turbulence. This will require further investigation before drawing a clear conclusion.

One could also suspect a wind speed bias due to the fact that the seeing monitors cannot operate at wind speed higher than 16 m/s. However, winds above this speed were only recorded 2% of the time over the last five years. Moreover, the seeing value is only relevant within the conditions for which the telescopes are operational. Since the operation limit at Sutherland for the small telescopes and for normal operations of SALT is a wind speed limit of 16 m/s, we can neglect the effect of wind bias.

2.4 Discussion

2.4.1 Degradation in the Site Conditions

The value for the median seeing reported in the present study is worse than those that were reported in earlier studies. Due to the methodology used in Warner (1994), we do not have a reliable way to compare their results with this study. Concerning the site testing results from Erasmus (2000), a more reliable comparison is possible as those measurements were made using the same type of instrumentation. This previous campaign reported a median seeing of 0.92", which is much lower than the 1.51" obtained from the entire set of DIMM data. That can be explained, to some extent, by the longer exposure time (10 ms) used in the previous study.

The bias in DIMM measurements due to long exposure times has been previously investigated by Tokovinin (2002). That analysis can be reproduced for the specific observing setups used for DIMM measurements in Sutherland studies by stacking the 3.3 ms exposures taken with TimDIMM. I

estimated the bias in the DIMM measurements from Erasmus (2000) by replicating their 10 ms exposure time. The variance of the differential motion in the stacked image with a 9.9 ms exposure time was 0.62 times the variance of the differential motion in the individual 3.3 ms exposures. Applying this correction to the 0.92" seeing reported by Erasmus (2000) gives a seeing value of 1.25" for an equivalent 3.3 ms exposure time, which is still lower than the current value of 1.51". Although this suggests a degradation of the seeing conditions since the site testing campaign of 1998-2000, one needs to be careful with such comparison. Even though this result is similar to the analytic model of Tokovinin (2002) for the degradation of the seeing measurement, the estimated correction may be inaccurate due to differences in the conditions between the two observing campaign. Regular, long-term monitoring with the same instrument is required to accurately determine how the site might be changing and whether those changes could be related to climatic change in Sutherland as observed at other sites (Sarazin, 2010).

2.4.2 Site Comparison

As reported in Section 2.3.1, the median integrated seeing conditions as measured for when both MASS and DIMM were operational and after a 10 minute binning was 1.49". I used this value to provide a uniform comparison to other sites, in terms of overall, FA and GL seeing. This median seeing is worse than that reported at other major astronomical observatories (Table 2.8), including Paranal (Sarazin et al., 2008), Cerro Tololo (Els et al., 2009), Mauna Kea (Chun et al., 2009), Mount Graham (Masciadri et al., 2010), Las Campanas (Thomas-Osip et al., 2012) and both the sites tested for the E-ELT (Vázquez-Ramió et al., 2012) and TMT (TMT site selection team, 2008). However, the FA seeing is comparable to the best astronomical sites (Table 2.8), which confirms the fact that turbulence at Sutherland is dominated by the ground layer. In terms of the other atmospheric parameters, the median isoplanatic angle at Sutherland, 1.94", is very similar to most sites. Five of the sites have a smaller isoplanatic angle, between 1.29" and 1.84", 3 have comparable values between 1.93" and 1.96" and 5 have larger values between 2.03" and 2.69". The median coherence time of 5.38 ms for Sutherland is the second best after Cerro Tolonchar. It also shows very long coherence time for the best 5% and 20% with respective values of 26.78 ms and 12.99 ms. However the accuracy of the coefficient C in eq. 2.4, used to derive the coherence time from MASS-DIMM data, is questionable. Comparing τ_0 results from MASS and DIMM measurements also shows discrepancies. Previous results from M. Sarazin at Paranal [2], reported in Tokovinin (2006), show that τ_0^{DIMM}, calculated from equation (3) in Sarazin et al. (2008), gives values 2.5 larger than τ_0^{MASS}. Here the correction I applied gives $\tau_0 \sim 1.73\tau_0^{MASS}$, which might still be underestimating the actual value. Considering the discrepancy between measurements from MASS and other instruments, as well as the low reliability of the correction applied due to the wide range of value for the coefficient C found in the literature, more investigation on the τ_0 value is needed. Although, it is reasonable to consider 5 ms as a lower limit on the coherence time at Sutherland since the 5.38 ms result is likely to be an under-estimation of the real value.

The observed overall worse seeing conditions at Sutherland compared to other sites can be partly explained due to several discrepancies between this data set and those from other sites results. First, many of these sites have only fully published results from earlier periods and I am not comparing results over the same time period. Recent results from Paranal indicated the seeing conditions have degraded over the last decade and that this may be due to longer term climatic changes (Sarazin, 2010).

[2] http://www.eso.org/gen-fac/pubs/astclim/paranal/asm/mass/MASS-Paranal-2003/

Table 2.8: *Comparison of Sutherland atmospheric turbulence parameters with other sites.*

Site	altitude [m]	median seeing			θ_0	τ_0	# nights / # data
		overall	GL	FA		(MASS$_{corr}$+GL)	
Sutherland	**1768**	**1.49”**	**1.34”**	**0.42”**	**1.94”**	**5.38 ms**	561 / 142,886 (16,860 after 10 min binning)
March 2010 - September 2013							
Cerro Tololo (Els et al., 2009)	2207	0.88”	0.44”	0.50”	1.56”	2.9 ms	NA / 433,162
2004-2008							
Mauna Kea (Chun et al., 2009)	4050	0.71”	0.51”	0.42”	2.69”	5.1 ms	124 / NA
2006-2007							
Paranal (Sarazin et al., 2008)	2635	1.1”	0.86”	0.56”	2.6”	3.6 ms	NA / NA
2007							
Mount Graham (Richardson, 1922)	3221	0.95”	0.81”	0.39”	2.5”	4.8 ms	43 / 16,659
2007							
Cerro Las Campanas (Primot et al., 1990)	2551	0.8”	0.58”†	0.47”	1.84”	2.46 ms‡	46 / 3,412
2010							
E-ELT (Batchelor, 1970)							
2008-2009 (∼ 1 year per site)							
Aklim (Morocco)	2350	1.0”	0.77”	0.52”	1.29”	3.5 ms	NA / 10,992
Cerro Maón (Argentina)	4653	0.87”	0.51”	0.66”	1.37”	3.4 ms	NA / 29,723
Roque de los Muchachos (Canary Island)	2346	0.8”	0.65”	0.32”	1.93”	5.6 ms	NA / 47,328
Cerro Ventarrones (Chile)	2837	0.91”	0.6”	0.55”	1.96”	4.9 ms	NA / 56,547
TMT (TMT site selection team, 2008)							
2003-2008 (> 2.5 years per site)							
Cerro Tolar (Chile)	2290	0,63”	0.34”	0.44”	1.93”	5.2 ms	NA / 196,812
Cerro Armazones (Chile)	3064	0.64”	0.35”	0.43”	2.04”	4.6 ms	NA / 212,367
Cerro Tolonchar (Chile)	4480	0.64”	0.32”	0.48”	1.83”	5.6 ms	NA / 89,958
San Pedro Mártir (Mexico)	2830	0.79”	0.58”	0.37”	2.03”	4.2 ms	NA / 139,359

†*GL seeing is not given in arcseconds in the reference paper, hence I calculated it from the MASS and DMM seeing values using the following formulae:* $see_{GL} = (see_{DIMM}^{5/3} - see_{MASS}^{5/3})^{3/5}$

‡*MASS time constant - not corrected*

Another important caveat is that the DIMMs at the comparison sites are typically located on 5 m high towers, while the Sutherland DIMM is located at ground level. Hence, the Sutherland results may be strongly affected by convective turbulence from the ground. Using the results from MASS-DIMM, SLODAR profiles, and previous studies, one can estimate the effect due to the lower 5 m surface layer. From MASS-DIMM, I found that 83% of the turbulence is located in the GL, and the SLODAR results tell us that the lowest 30 m contributed 25% of the GL. In Erasmus (2000), it is reported that the first 5 m have a seeing of 0.15", which correspond to 66.3% of the turbulence associated with the 0.19" seeing of the first 30 m for that period. Using the same proportion one can reasonably consider that the first 5 m contributes roughly 14% of the overall turbulence. From this, I would expect that the integrated median seeing measured from a 5 m platform would be 1.36". Following the same procedure, the expected seeing at the dome entrance for SALT, which is located at approximately 30 m, would be 1.29". In addition, when fitting the dome/tube seeing for profile reconstruction in SLODAR, part of the turbulence outside the dome belonging to the ground layer might be subtracted resulting in an underestimation of both the ground layer and the overall turbulence. As a result, the first 30 m may be contributing more than 25% of the turbulence.

However, despite the facts considered above, the altitude of the Sutherland site (1768 m) is much lower than all the other sites with altitudes ranging from 2290 m to 4653 m, so I do not expect the seeing at Sutherland to be as good as these other sites.

In terms of GL, both Chun et al. (2009) and Masciadri et al. (2010), respectively for Mauna Kea and Mount Graham, presented high vertical resolution turbulence profiles. The Sutherland site differs significantly from those two sites due to its strong upper ground layer located at 250 to 400 m. The Sutherland upper GL contributes nearly 50% of the GL turbulence while it is only 2% and 12% for Mauna Kea and Mount Graham, respectively. Most of the turbulence at those sites is located in the lower layers, 90% in the first 40 m for Mauna Kea and 70% in the first 100 m for Mount Graham, compare to only 30% in the first 100 m at Sutherland.

2.5 Conclusions

In this study, I built on previous studies of the Sutherland observing site to provide a more recent measurement of the site conditions, which may have degraded over time, and a measurement of the turbulence profile. A fully automated MASS-DIMM, providing them with real-time continuous seeing measurements, has proven to be highly valuable for observers on the Sutherland plateau.

From 5 years of seeing measurements consisting of 28 days of SLODAR operation, 561 days of MASS-DIMM operation and 546 additional days of TimDIMM measurements, for a total of 4535 SLODAR data points, 142886 MASS data points and 464186 DIMM data points, I obtained a reliable evaluation of the current seeing conditions at the Sutherland site. Even though the Sutherland site presents generally worse seeing conditions than at other astronomical sites with a median value of 1.51", 83% of the turbulence is located in the first 1 km layers. In addition, its coherence time is comparable to the best sites with a median value of 5.38 ms and a value of 12.99 ms for favorable conditions (20% of the time). Under such conditions, significant image quality improvements could be achieved by the means of adaptive optics correction. Like most astronomical sites, Sutherland presents three main layers contributing to the turbulence: the ground layer below 1 km, a layer between 2 and 5 km in which turbulence is driven by the wind shear, and the upper layers above 12 km where turbulence are associated with the jet-stream. Moreover, the 28 nights of SLODAR profiles indicate that the GL is dominated by two layers: the first 50 m and another layer between 250 and 400 m.

In the end, the Sutherland site presents atmospheric turbulence characteristics quite similar to other sites and, despite a worse overall seeing, presents favourable features (strong ground layer and some long coherence time periods) for AO correction. The results from this extensive site characterization were used as the input for AO simulations and the study of potential improvement for

SALT image quality. This study is presented in Ch. 4 of this thesis.

To further characterize the atmospheric turbulence at the Sutherland site, a three weeks campaign with a GSM (Generalized Seeing Monitor) and a PBL (Profileur de Bord Lunaire) was carried out in August 2011 in collaboration with a team from the University of Nice Sophia Antipolis. This campaign was part of the commissioning of the PBL instrument. In the framework of this thesis, I have been working on the data processing and inversion method for the reconstruction of high altitude resolution profiles from PBL data. This work is presented in Ch. 3.

Chapter 3

PBL: A NEW INSTRUMENT TO CHARACTERIZE THE TURBULENCE

Contents

A collaboration with the "Laboratoire Lagrange" at the University of Nice has been initiated in July 2011. They developed the "Profileur de Bord Lunaire" (PBL, Profiler of Moon limb in English), a new instrument which is aimed to provide high altitude-resolution profiles of the atmospheric turbulence as well as profiles of the outer-scale. The principle of the PBL is based on the use of the differential angle of arrival (AA) measurements along the Moon limb to reconstruct the turbulence and outer scale profiles (Ziad et al., 2013). An observing campaign with the PBL was conducted at the Sutherland site in August 2011. Those measurements were used to implement the data processing scheme and develop an inversion method in order to recover the atmospheric turbulence profile and associated parameters.

The main advantage of the technique is to give all the integrated atmospheric parameters that can be determined by other instruments ($r_0, \varepsilon_0, \theta_0 \tau_0$) at once, and in addition provide a very high

altitude-resolution profile of the turbulence ($C_n^2(h)$) and potentially the outer scale ($\mathcal{L}_0(h)$).

Section 3.1 of this chapter is dedicated to the description of the optical and mechanical layout of the instrument. Section 3.2 is dedicated to the data acquisition and pre-processing of the data performed prior to the extraction of the atmospheric parameters and the profile reconstruction. In the Section 3.3 I give a summary of the theoretical background of the measurement method using the differential angle of arrival covariance. In Section 3.4 I describe the experimental measurement process. In order to test the measurement pre-processing and inversion method, I ran simulations on synthetic data. Those simulations are described in Section 3.5. Finally, in Section 3.6 I present the results from the Sutherland observing campaign.

3.1 Optical layout - Data acquisition process

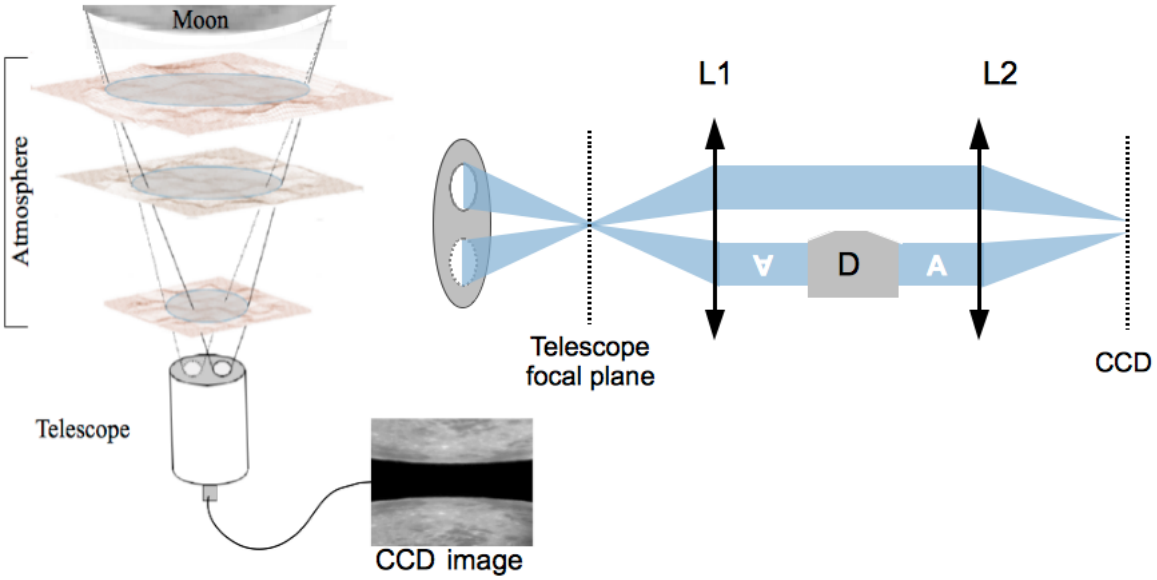

Figure 3.1: *PBL optical layout. Left: Sketch of the overall instrument setup with the 2 sub-aperture mask at the entrance pupil of the telescope. Right: Diagram of the optical path from the telescope entrance pupil to the imaging CCD. L1 is a collimating lens, D represents the Dove prism and L2 re-focuses the collimated beam onto the imaging CCD.*

The PBL (Ziad et al., 2013) was designed to provide high altitude-resolution profiles of the atmospheric turbulence. Similar to the DIMM technique, it uses a differential method via a two sub-aperture mask mounted at the entrance pupil of the telescope. This allows for telescope vibration and wind shake effects to be ignored. Similar to the SLODAR method, the profiles are reconstructed from the covariance functions. The use of the continuous Lunar limb, as compared to a double star with SLODAR, provides a large number of separation angles, allowing for the high altitude-resolution of the profiles.

The PBL consists of a 16 inch MEADE telescope tube mounted on an Astro-Physics AP3600 equatorial mount with a mask made of 2 holes with separation $B = 0.267$ m, and diameter $D = 0.06$ m (Fig. 3.1, left). When pointing the telescope at the Moon two images of the limb are produced, corresponding to the two sub-apertures. In order to separate the 2 images, a Dove prism is introduced in the optical path (Fig. 3.1, right). The Dove prism flips over one of the images and avoids overlap of the images. The image acquisition is performed by a PCO Pixelfly CCD operating at a frame rate of 33 Hz. The CCD, with a pixel size of 9.9 microns, produces images of 640x480 pixels. The image scale is 0.594 arcseconds per pixel. The exposure time needs to be short enough to "freeze" the turbulence, typically of the order of few ms (i.e. τ_0), here it was set

to 5 ms. The number of images used for each measurement was set to a thousand images per data set. For each acquisition, I used the statistical properties of the atmospheric turbulence to retrieve its parameters.

3.2 Data pre-processing

Prior to the data analysis leading to the profile reconstruction, there are a number of steps that need to be followed. These will ensure that any instrumental bias due to optical misalignment and imperfect tracking were removed. When performing the differential measurements, it is crucial to properly match the same point on the Moon edge from both images, and hence only measure the edge motion due to atmospheric turbulence.

3.2.1 Image "cleaning"

As for most astronomical images, it is necessary to remove the flats and darks of all images. The first step of the pre-processing will hence consist in dark and flat fielding the images. Both master dark and flat images are constructed by taking the mean value of a series of 10 images at the beginning of the night prior to starting the measurements. After creating the master flat and the master dark, I applied the usual method to clean the images:

$$IMAGE_{clean} = \frac{IMAGE_{raw} - DARK}{FLAT - DARK}.$$

3.2.2 Image rotation

Due to a slight misalignment of the dove prism, there might be some rotation between the top and bottom images that needs to be corrected for. This is a static bias that is measured once and then used to apply the correction to all images. This value needs to be verified any time the system is moved to a new site and on regular basis for a set location, as temperature variation may affect the position of the prism as well as the general optical alignment of the system.

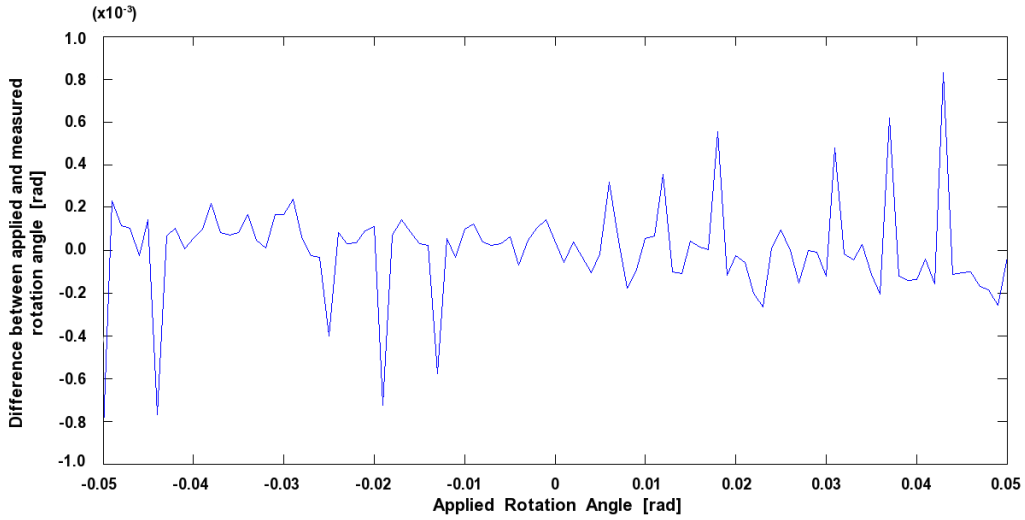

Figure 3.2: *Testing the rotation angle measurement. I measured the difference between a known rotation applied to the image and the value measured using the parabola fitting method. x-axis: Applied rotation in radians. y-axis: difference between applied and measured rotation in radians.*

In order to correct for this rotation, I first did simulations. By applying a known rotation to a reference image, and recovering it using the method described below, I could probe the accuracy of the method before applying it to the data set. To retrieve the rotation angle between the top and

bottom images, I first fit a parabola to both Moon limb position. Then I subtract one parabola to the other and the data points of the difference are fitted with a straight line which slope s is directly related to the rotation angle (θ): $s = tan(\theta)$. I created a series of simulated images with a range of rotation angle going from -0.05 to 0.05 radian. Then, I applied the method defined earlier to measure those angles and compared them with the value of the rotation angle that was originally applied. Fig. 3.2 shows the difference between the measured and the applied rotation as a function of applied rotation angle, the mean error ($< |\theta_{applied} - \theta_{measured}| >$) is 0.0002 rad.

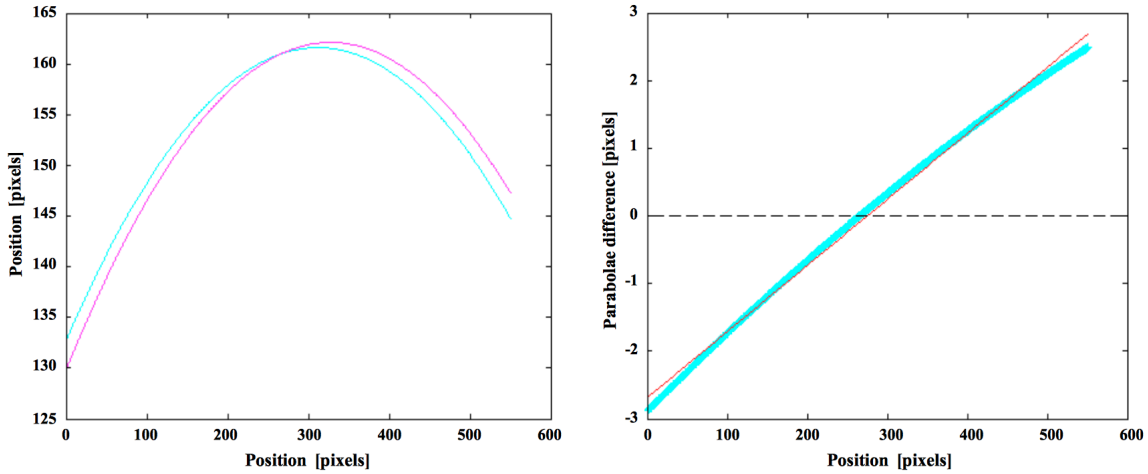

Figure 3.3: *Measured rotation angle on a single acquisition. Left: example of one parabola fitting. In pink, the fit to the top images mean position, in blue the one to the bottom images. Right: Parabola difference (blue) and line fitting (red) from which I retrieve the rotation angle.*

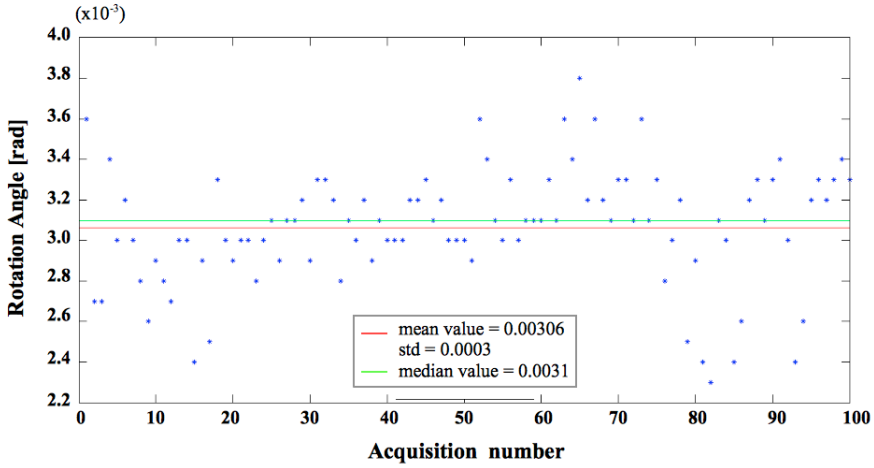

Figure 3.4: *Measured rotation angle over a hundred of acquisitions. The measured rotation angle for 100 acquisition (blue dots) are re[resented along with the mean (red) and median (green) values.*

In practice the images are not always aligned, so on top of the rotation they are also most likely affected by x-y translation. However, while the rotation is static and common to all images, translations, due to image drifting, telescope vibrations and wind shake or seeing, varies from one image to the next. Hence, instead of measuring the rotation angle for single images, I used the mean position of top and bottom images over one acquisition of a thousand images. The averaging over the thousand images of an acquisition smooth out the not static translations to only show the static rotation bias. Fig. 3.3 (left) shows one example of the parabola fitted to the top and bottom mean limb positions. One can clearly see the rotation between the two. Fig. 3.3 (right)

shows the difference between the two and the fitted line from which the slope gives the rotation angle. I measured the parabolae and the slopes of the differential position line fitting for a hundred acquisitions. Then I calculated the mean and median value of the measured rotational angle, respectively 0.0029 and 0.003 rad as one can see in Fig. 3.4. As expected, the standard deviation (0.0003 rad) is of the same order of the previously determined measurement error (ie. 0.0002 rad). Based on those measurements, I applied a rotation correction of 0.003 rad to the full data set.

Once the rotation angle between the top and bottom images has been determined, I implemented the correction in my final data pre-processing method. After the dark subtraction and flat fielding I applied the rotation correction to the bottom image with respect to the top one.

3.2.3 Image shift

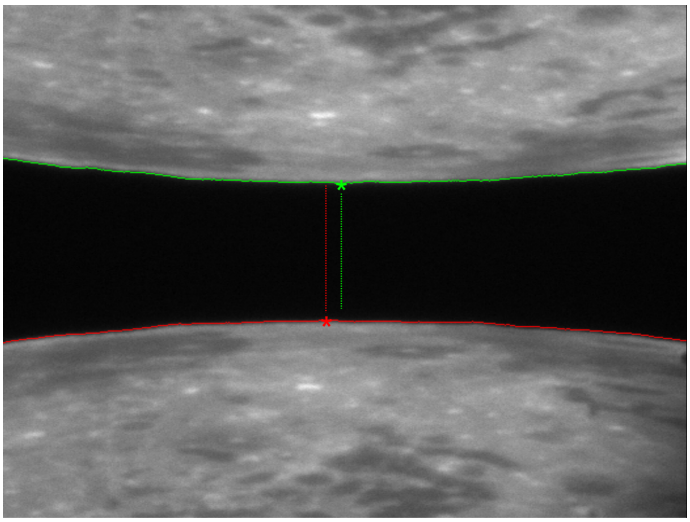

Figure 3.5: *Coarse image alignment using parabolae. Moon limb image and the fitted parabola (green and red) to its edge positions. The lower (higher) point of the parabola are marked with a star. The dotted lines help to visualize the shift between the 2 images.*

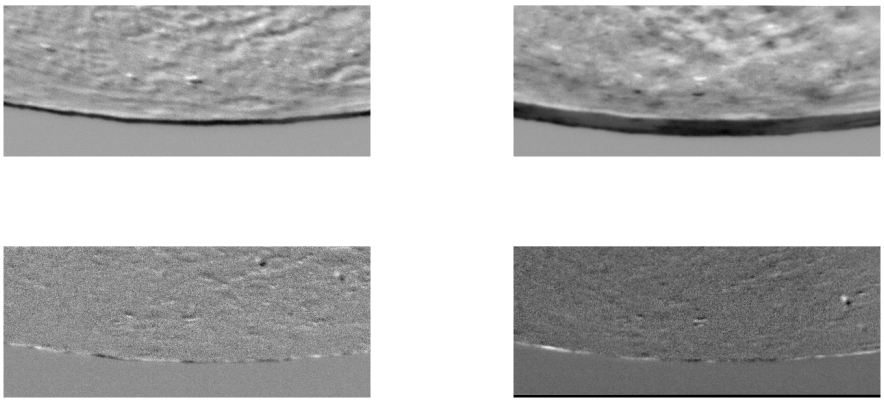

Figure 3.6: *Fine alignment using image difference. Top: image difference between the reference image (the first image from an acquisition) and image 500 of that same acquisition. Bottom: image difference after alignment. On the left alignment of the top image of the Moon limb, and on the right, alignment of the bottom image.*

After measuring and correcting for residual rotation due to potential optical misalignment, a fine alignment of the top and bottom images along the x-axis is necessary. Since I am using a

differential method I need to have the corresponding points from the top and bottom limb images accurately aligned on the same pixel column. I performed a first coarse alignment which consists in fitting a parabola to both edges, then use the shift between the position of their maximum to align the images. This process is illustrated in Fig. 3.5. I then refined the alignment by computing the intensity difference D between the image to be aligned and a reference image, for shifts ($d_x(i)$,$d_y(j)$) between -10 and +10 pixels:

$$D(i,j) = \frac{\Sigma_{x,y}[I_{REF}(x,y) - I_{IM}(x + d_x(i), y + d_y(j))]^2}{\Sigma x.\Sigma y}$$

The minimization of the square difference gives us the image shift correction ($d_x(i_{min})$,$d_y(j_{min})$) that needs to be applied in order to align each image with the reference image. In practice, I took the first image of an acquisition as the reference image for alignment of all the other images of that acquisition. An example of image alignment is shown in Fig. 3.6.

From this alignment I only kept the correction in x ($d_x(i_{min})$) for each image. The correction in y corrects for image wandering due to telescope shake and vibration as well as image drifting. However it also corrects image motion due to seeing that we intend to measure. Under strong seeing (> 2"), the displacement along y due to seeing can be as large as 10 pixels. Hence if we align the images in the y direction we will smooth out the displacement due to seeing and underestimate it. Instead I will correct for telescope vibration and image drifting independently.

3.2.4 Image drift

The drifting is a systematic bias due to inaccuracy in the polar alignment and tracking error. Hence it can be measured using the average position of the limb throughout a series of a thousand images obtained during an acquisition (Fig. 3.7). As one can see, when drifting occurs, we see a slope trend throughout an acquisition. By measuring this slope one can compensate for the drifting effect.

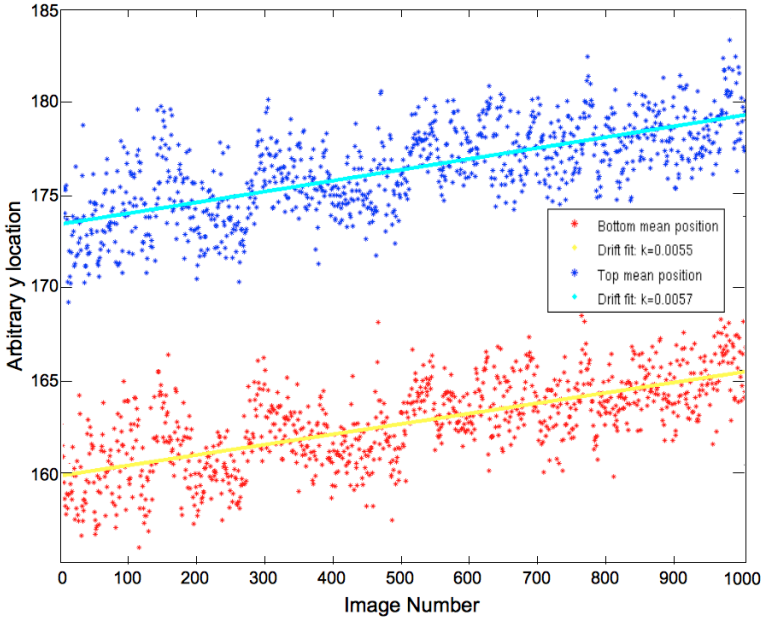

Figure 3.7: *Measurement of the drifting of the top image (blue) and the bottom image (red) throughout an acquisition (1000 images). The stars represent the average position of the Moon limb for each image and the slope (k) of the fitted line gives us the amount of drifting.*

3.2.5 Vibrations and wind shake

Telescope vibrations and wind shake are random processes, so the best way of getting rid of it is via differential measurement, as both the top and bottom images are similarly affected by this effect. In addition, and for verification purposes, I also used single edge measurements. In order to suppress the effect of telescope shake and vibrations, I applied a high frequency filter to the measured positions as shown in Fig. 3.8.

In conclusion, the overall alignment process in the case of differential measurements is summarized in Fig. 3.9.

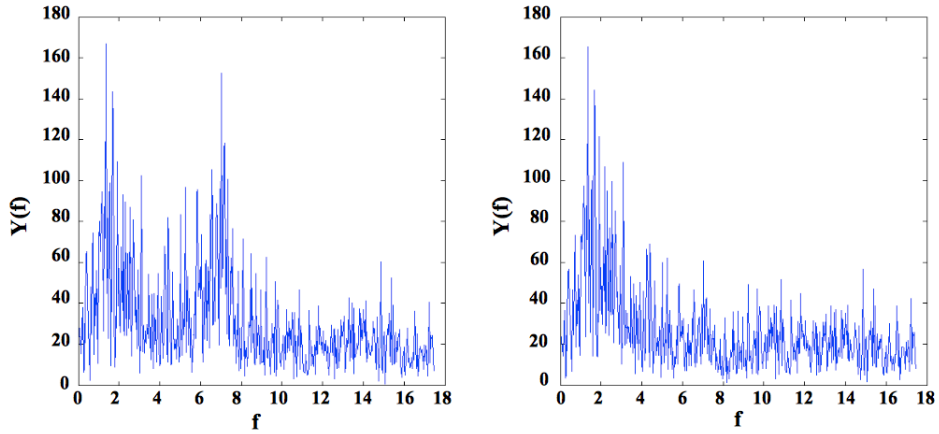

Figure 3.8: *High frequencies filtering. Representation of the temporal variation of limb position in the frequency domain. Right: before filtering. Left: after filtering.*

3.2.6 Edge detection

Since the PBL is based a method that uses differential measurements of the position of the Moon limb, an accurate detection of the edge position of the Moon is essential. Around the edge, the image can be assimilated to an Heaviside function, and hence its derivative will be close to a Dirac function (Fig. 3.10). In practice, the edge doesn't drop sharply and there is noise, both before and after the step. Because of this, the derivative will give a peak function which width and height mainly depend on the image contrast and Moon features of different brightness affecting the wings. However, the peak is high enough above the noise and sharp enough to determine its center accurately. Fig. 3.11 is an example of an image (Top left) and its derivative (Bottom left). For both figure, a vertical cut along one column (blue line) and their corresponding intensity profiles are shown on the right-hand-side of each figure. The peak detection is then done via a first rough determination of the peak by finding the maximum of the derivative function. Then I applied a barycenter measurement around the position of the maximum $(p(i_{max}), I(i_{max}))$ to obtain the final peak position p_{peak} (Fig. 3.11, right):

$$p_{peak} = \frac{\sum_{i_{max}-5}^{i_{max}+5} p(i) * I(i)}{\sum_{i_{max}-5}^{i_{max}+5} I(i)},$$

where p is the position along the image column (the x-axis on the right hand side graph of Fig. 3.11), and I is the "intensity" of the derivative (y-axis on the right-hand-side graph of Fig. 3.11). I excluded negative "intensity" values from the calculation by replacing them by zero. The measured p_{peak} for each position along the images x-axis are saved as the Lunar limb positions.

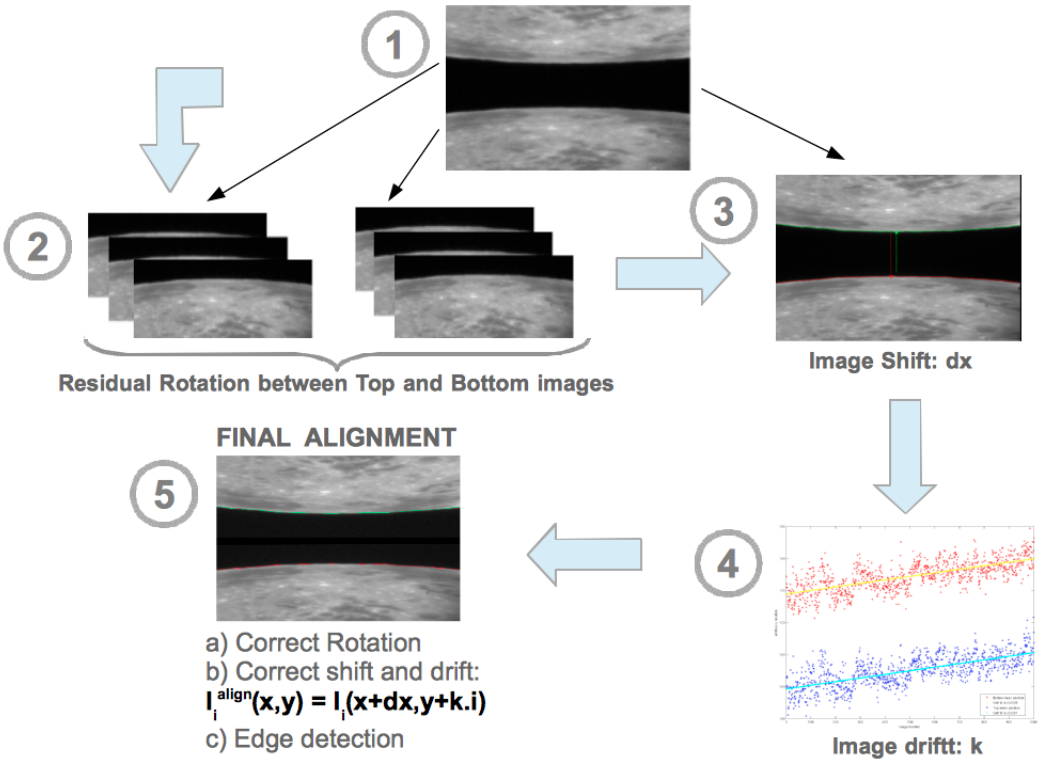

Figure 3.9: *Full alignment process summary. 1: use the first image of an acquisition as the reference image. 2: from the 1000 images of an acquisition measure the residual rotation between the Top and Bottom images. Use it to correct each image of the acquisition. 3: find the x displacement of each image (dx_i) with respect to the reference image. 4: find the amount of drifting through an acquisition, and the correction parameter k. The figure in step 4 shows, in dark blue and red, the position of the 1000 images before correction of the drifting, and in cyan and yellow, the positions after correction. 5: the last step consists in applying the dx_i and $k.i$ correction to each image, after correction of the rotation. Then the images are ready to be used for edge detection and data extraction.*

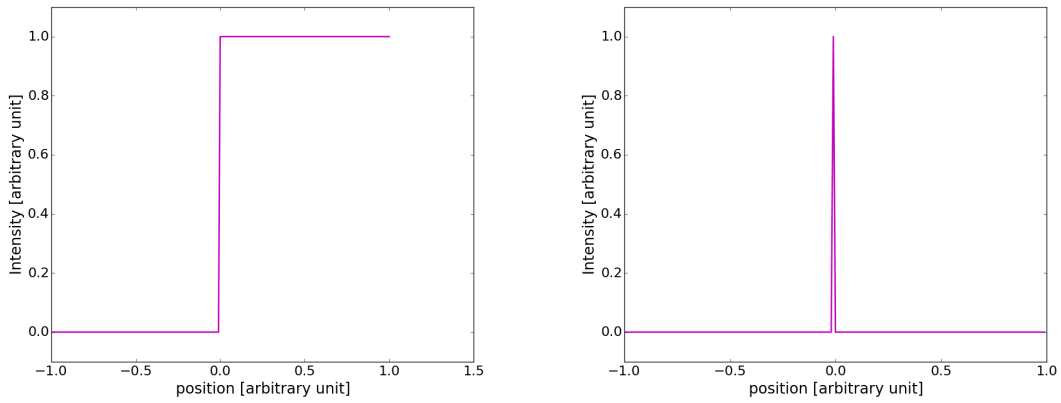

Figure 3.10: *Edge detection - theoretical curve. Left: Heaviside function. Right: derivative of the Heaviside function.*

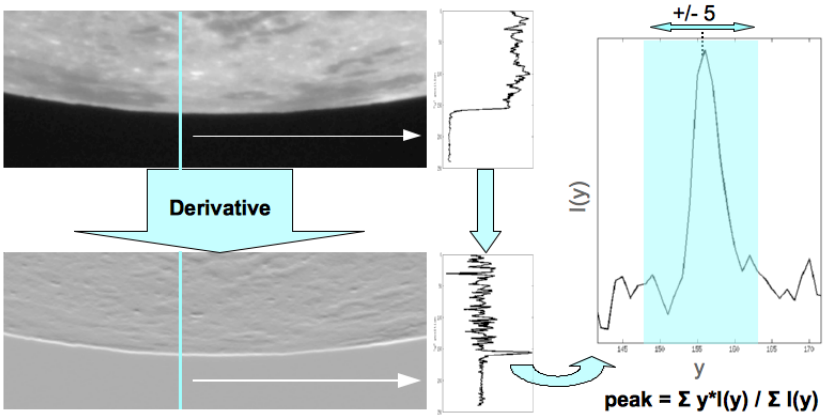

Figure 3.11: *Edge Detection. Top left: original image and an example of a vertical cut showing an Heaviside step function at the edge of the Lunar limb. Bottom Left: Derivative of the image and the peak function of its vertical cut. Right: Zoom in around the peak of the image derivative and windowing used to perform a barycenter measurement of the peak position.*

3.3 Theoretical Background and Reconstruction Method

The optical atmospheric turbulence is commonly described by a Kolmogorov spectrum: $\Phi_n(k) = 0.033\ C_n^2\ k^{-11/3}$, where k is the wave number. However, the Kolmogorov's model assumes an infinite outer scale ($\mathcal{L}_0$) value. In order to take into account the finite size of the outer scale, other models were developed. In the case of the PBL instrument the Von Karman model is used: $\Phi_n(k) = 0.033\ [2\pi]^3\ C_n^2\ [k^2 + [\frac{2\pi}{\mathcal{L}_0}]^2]^{-11/6}$. Based on this model, the AA spatial covariance is given by (Borgnino et al., 1992; Avila et al., 1997):

$$C_\alpha(B,D) = 1.19 sec(z) \int dh C_n^2(h) S(B,D,\mathcal{L}_0(h)), \tag{3.1}$$

with

$$S(B,D,\mathcal{L}_0(h)) = \int df f^3 (f^2 + \frac{1}{\mathcal{L}_0(h)^2})^{-11/6} [J_0(2\pi f B) + J_2(2\pi f B)] \left[2\frac{J_1(\pi D f)}{\pi D f}\right]^2, \tag{3.2}$$

where z is the zenith angle, B is the separation between two sub-apertures of diameter D, $\mathcal{L}_0(h)$ is the outer scale at the altitude h, $C_n^2(h)$ the turbulence strength at that same altitude, f the spatial frequency and J_n are Bessel function of order n.

In the case of differential measurements, and for observations in two directions separated by an angle θ (Fig. 3.12) the differential angular covariance can be expressed as follow (Ziad et al., 2013):

$$C_{\Delta\alpha}(B,D,\theta) = 2C_\alpha(\theta h, D) - C_\alpha(B - \theta h, D) - C_\alpha(B + \theta h, D). \tag{3.3}$$

θh is the spatial distance of the perturbed wavefront intercepted by an angle θ at an altitude h (Fig. 3.12). Using eq. 3.1 and 3.2, this gives:

$$C_{\Delta\alpha}(B,D,\theta) = 1.19 sec(z) \int dh C_n^2(h) [2S_0^h - S_-^h - S_+^h]. \tag{3.4}$$

where, $S_0^h = S(\theta h, D, \mathcal{L}_0(h))$, $S_-^h = S(B - \theta h, D, \mathcal{L}_0(h))$ and $S_+^h = S(B + \theta h, D, \mathcal{L}_0(h))$.

Considering the overall atmosphere as a superposition of thin (Δh_i) discrete layers at altitudes (h_i), we can rewrite this expression as a sum:

$$C_{\Delta\alpha}(B,D,\theta) = 1.19 sec(z) \sum_i \Delta h_i C_n^2(h_i) [2S_0^{h_i} - S_-^{h_i} - S_+^{h_i}], \tag{3.5}$$

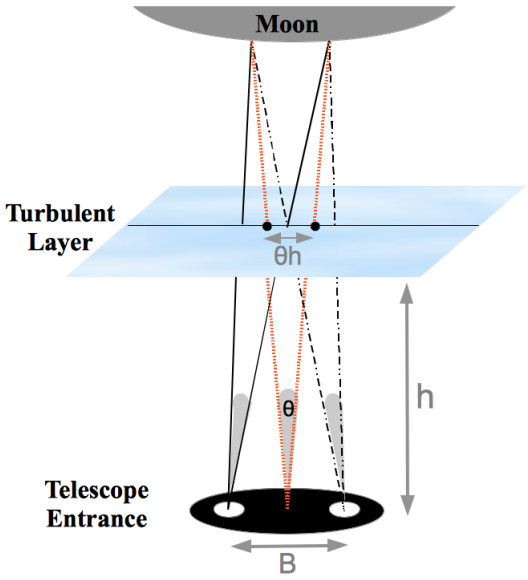

Figure 3.12: *Principle of PBL measurement. When measuring the angular covariance of a system with a fixed base, B, the contribution of a layer at an altitude h peaks for an angular value of* $\theta = \frac{B}{h}$.

For easier calculation, we split the components solely dependent on predefined parameters (altitude grid and system parameters) from those dependent on parameters that need to be determined($C_n^2(h)$, $\mathcal{L}_0(h)$), as follow:
- The energy term, containing the turbulence strength information:
$K^{Cn}(h) = 1.19sec(z)\Delta h C_n^2(h)$,
- The shape term, containing the outer scale value information:
$K^L(h,f) = f^3(f^2 + \frac{1}{\mathcal{L}_0(h)^2})^{-11/6}$,
- The filtering terms, linked to the system sub-pupils and base:
$K_0^J(h,\theta,f) = [J_0(2\pi f\theta h) + J_2(2\pi f\theta h)]\left[2\frac{J_1(\pi Df)}{\pi Df}\right]^2$,
$K_-^J(h,\theta,f) = [J_0(2\pi f(B-\theta h)) + J_2(2\pi f(B-\theta h))]\left[2\frac{J_1(\pi Df)}{\pi Df}\right]^2$ and
$K_+^J(h,\theta,f) = [J_0(2\pi f(B+\theta h)) + J_2(2\pi f(B+\theta h))]\left[2\frac{J_1(\pi Df)}{\pi Df}\right]^2$.
This allows us to rewrite the S integrals in the following form:

$$S_{0,-,+}(h,\theta) = \int_f df K^L(h,f).K_{0,-,+}^J(h,\theta,f), \tag{3.6}$$

The $S_{0,-,+}(h,\theta)$ functions can be determined for each individual layer and hence summing over all altitude gives:

$$C_{\Delta\alpha}(\theta) = \sum_h K^{Cn}(h).[2\int_f df K_0^J(h,\theta,f).K^L(h,f) - \int_f df K_+^J(h,\theta,f).K^L(h,f) - \int_f df K_-^J(h,\theta,f).K^L(h,f)]. \tag{3.7}$$

If we consider the case of a fixed $\mathcal{L}_0$, the three $\int_f df K^J.K^L$ components can be pre-calculated and stored in a matrix $K^S = 2S_0 - S_- - S_+$ (Fig. 3.13). We can then write:

$$C = K^{Cn}.K^S,$$

where K^{Cn} is a 1xN matrix and K^S is a NxM matrix, with N the number of layers of the reconstruction grid and M the number of separation angle (θ) along the Lunar limb. θ is shown in

Fig. 3.12. The Lunar limb is an extended source and hence provide a large number of separation angle, as compared to DIMM that only uses one.

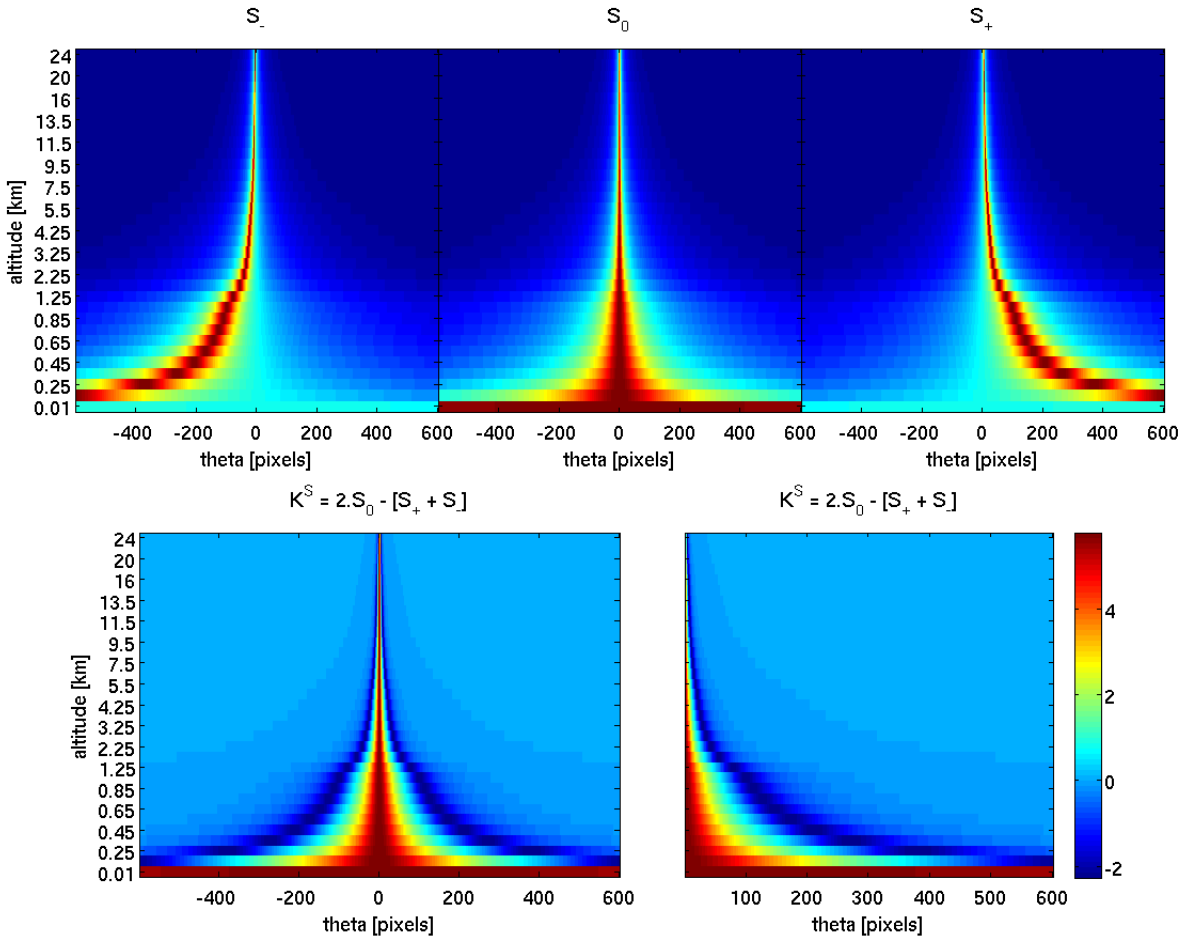

Figure 3.13: *Theoretical "S" functions, given by eq. 3.6. Top: $S_{-}(\theta,h)$, $S_0(\theta,h)$ and $S_{+}(\theta,h)$ from left to right. Bottom: K^S matrix. In all five figures h is increasing from bottom to top. Values are given for the 33 single layers of the reconstruction grid. θ goes from -365" to 356" from left to right for the three top figures and the bottom left. The bottom right figure shows the positive values of K^S that will be used for the inversion as we only measure positive θ.*

Using a chosen altitude grid and the θ values set by the system configuration, one can compute all the K^J functions, and in turn the S functions at fixed $\mathcal{L}_0$, and the corresponding K^S matrix. The top row of Fig. 3.13 shows the theoretical $S_{0,-,+}$ functions while the bottom graph represents the K^S matrix that I will use in the inversion. The bottom left shows the full K^S matrix, including negative θ values. Since measurements are only done for positive θ,I used the positive side of the matrix for the inversion (bottom right of Fig. 3.13). The number of separation angles available (x-axis) is set by the system layout and is given by the number of pixels along the Lunar limb. Here I have set the number of layers to 33 with a range of altitudes going from 10 m to 24 km above the telescope entrance pupil. $\mathcal{L}_0$ is set to 20 m. I also show the 2D curve of the theoretical $S_{0,-,+}$ functions for 7 individual layers in Fig. 3.14. From this representation, we can clearly see that the position of the covariance peak in the lateral components (bottom graph of Fig. 3.14) is dependent on the layer altitude h. In fact, $\theta_{peak} = \frac{B}{h}$, with B the base between the 2 apertures at the telescope entrance pupil. Hence for lower altitudes, the peak of covariance is located at larger separation angles θ. Fig. 3.15 shows the combined S_0,S_{-} and S_{+} (blue lines) resulting in the theoretical differential covariance (black line) for a single layer at 350 m. Here for simplicity, I considered a layer of unity

strength, $K^{Cn} = 1$, and $\mathcal{L}_0 = 20$ m. For a given base B, the peak of covariance seen in the lateral components at $\theta_{peak} = \pm\frac{B}{h}$, reflects as a negative peak in the differential covariance. Note that only positive separation angles are measured, so for the reconstruction, I only considered the positive components of the covariance. In the more realistic case, the atmosphere is assumed to be made

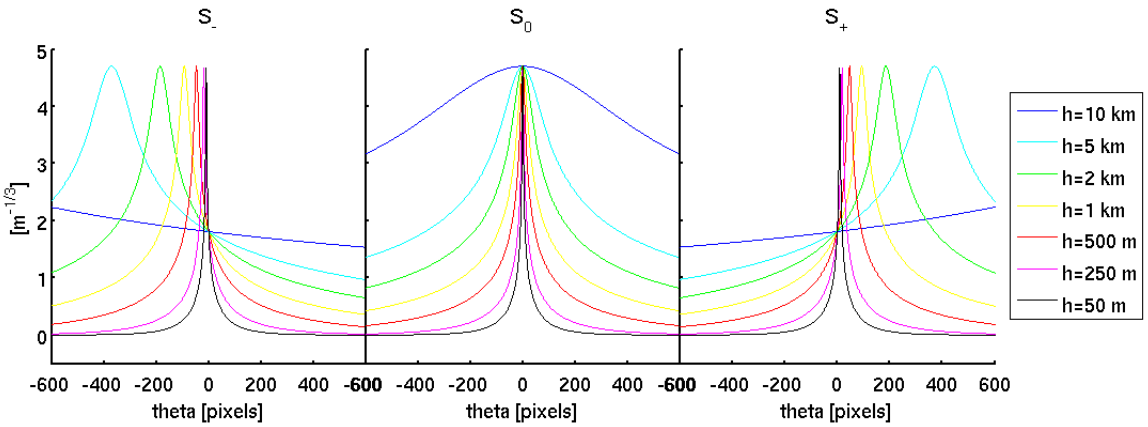

Figure 3.14: *Theoretical $S_{0,-,+}$ for single layers with $\mathcal{L}_0(h)$ =20 m. Left: S_-. Center: S_0. Right: S_+. Each color represents the functions for a different layer altitude: h = 50 m, 250 m, 500 m, 1 km, 2 km, 5 km and 10 km. Those correspond to single rows from the top three images of Fig. 3.13.*

up of multiple layers of variable thickness at different altitudes, with different turbulence strength and outer scale value. In order to obtain the theoretical model of the covariance produced by a multi-layered atmosphere, one need to determine the parameters of each individual layer (i). Those includes: h_i, Δh_i, $C_n^2(h_i)$ and $\mathcal{L}_0(h_i)$. Then, all the layers contribution can be summed up providing the equivalent covariance for the overall atmosphere. From those parameters, two are preset before hand (h_i, Δh_i), and the other two ($\mathcal{L}_0(h_i)$, $C_n^2(h_i)$), can be retrieved by minimizing the difference between theoretical and measured values. However in the case of differential measurements, the outer scale impact on the covariance is negligible, hence for the PBL the outer scale value is fixed to 20 m. I developed an algorithm using the simulated annealing technique (Kirkpatrick et al., 1983), for the minimization process, to reconstruct the turbulence profile, $C_n^2(h).dh$.

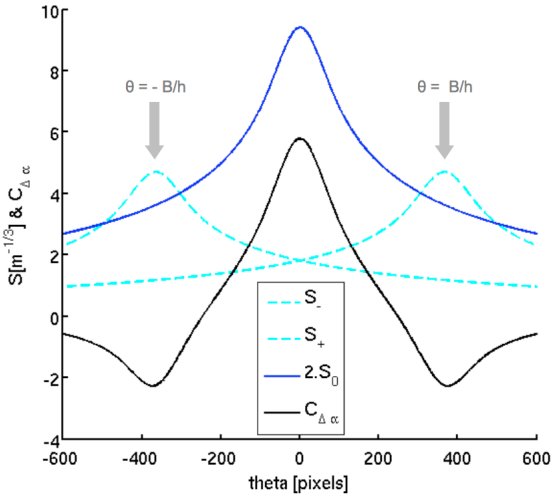

Figure 3.15: *Covariance for a single layer of unity strength at h=350 m and with $\mathcal{L}_0$ = 20 m. Dark blue line: $2S_0$. Sky blue dashed lines: $S_{+,-}$. Note the position of the peak of the lateral component located at $+/-\frac{B}{h}$ Black line: $C_{\Delta\alpha}(h = 1km) = K^{Cn}.[2S_0 - S_- - S_+]$, with $K^{Cn} = 1$.*

3.3.1 Altitude grid and Inversion Response

Table 3.1: *Reconstruction altitude grid.*

GL	h[m]	10	150	250	350	450	550	650	750	850	950									
						dh = 100 m														
FA	h[km]	1.25	1.75	2.25	2.75	3.25	3.75	4.25	4.75											
						dh = 500 m														
h[km]	5.5	6.5	7.5	8.5	9.5	10.5	11.5	12.5	13.5	14.5		16	18	20	22	24				
					dh = 1 km							dh = 2 km								

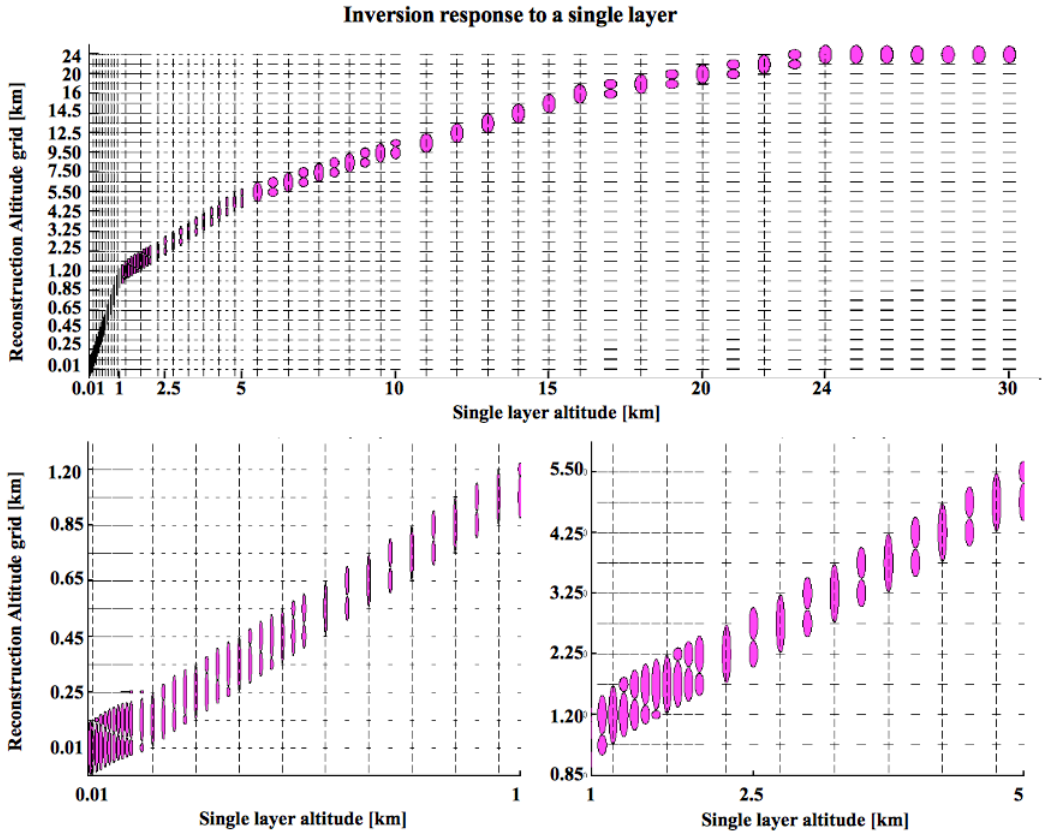

Figure 3.16: *Response of the inversion algorithm to single turbulent layers. Top: the input single turbulent layer altitude is given on the x-axis while the y-axis represents the altitudes of the reconstruction grid. For each input layers (x) the relative distribution of the turbulence throughout the reconstruction grid layers (y) is represented by the pink ellipses. Bottom: Zoom on the 0 to 1 km and 1 to 5 km range of altitudes, otherwise not clearly visible.*

In order to cover both the GL and the FA part of the atmospheric turbulence, I chose a 33 layers grid. It is made of 10 layers for the GL below 1 km and 23 layers for the FA between 1 and 25 km. The detail of the altitude grid is given in Table 3.1.

I tested the response of the reconstruction grid to 89 individual turbulent layers with altitudes ranging from 5 m to 30 km. For simplicity, all layers were of unit strength (K^{C_n} = 1) and with an outer scale value ($\mathcal{L}_0$) fixed to 20 m. The response results are shown in Fig. 3.16 and 3.17.

In Fig. 3.16, the x-axis shows the altitude of the input turbulent layer, while the y-axis shows the altitudes of the reconstruction grid. The pink ellipses represent the relative amount of turbulence. Fig. 3.17 shows the sensitivity of each of the reconstruction grid altitude to turbulence in the adjacent layers. The base of each triangle gives the range of altitudes for which the individual layers of the reconstruction grid can sense turbulence. The height at each altitude gives the sensitivity strength from 0 to 1, the latter being 100% sensitive. The bottom graphs of each figure are enlargement on the 0 to 1 km and the 1 km to 5 km altitude range which are otherwise not clearly visible.

For each of the 89 single turbulent layers, the reconstruction process should apportion the turbulence of the input layer between the 33 layers of the reconstruction grid. One expects that for a turbulent layer located at one of the reconstruction grid altitudes, all the turbulence will be reflected in that layer after the inversion. In the case of a turbulent layer located in between two altitudes of the reconstruction grid, one expects the reconstruction to spread the turbulence between the adjacent layers. If we take the input 10 km layer (on the x-axis), located in between the 9.5 km and 11 km layer of the reconstruction grid (on the x-axis), the turbulence is redistributed with 63.7% in the 9.5 km layer and 36.3% in the 11 km one. Similarly, the 21 km layer is split with 48.15% in the 20 km layer and 51.85% in the 22 km layer. The redistribution agrees with the theoretical expectations and validates both the choice of the altitude grid and inversion method.

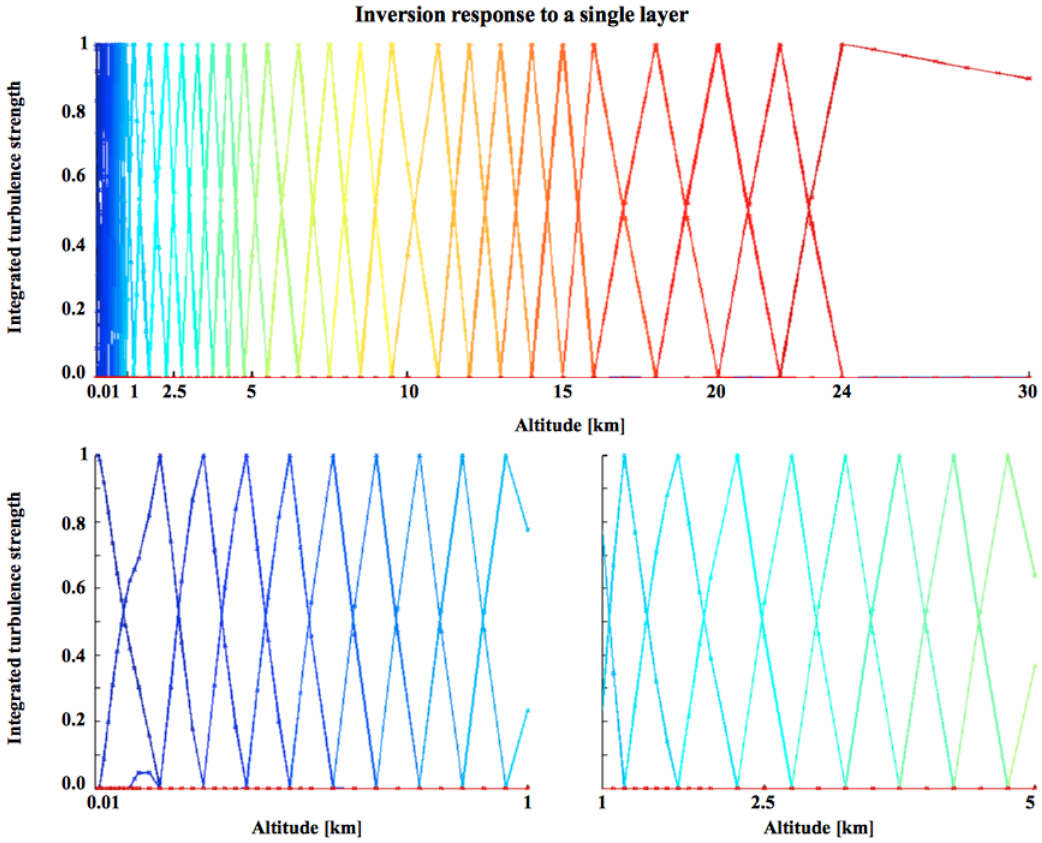

Figure 3.17: *Sensitivity of each layer of the reconstruction grid to adjacent layers. Top: The color triangle-like shape curves represent the sensitivity of each layer of the altitude grid to turbulence in layers at different altitudes. The x-axis shows the altitude at which the simulated a single turbulent layers are located. I used the same 89 single turbulent layers as in Fig. 3.16. The y-axis gives the sensitivity, 1 corresponds to 100%. From the triangles, one can see that each altitude of the reconstruction grid is 100% sensitive to turbulence at that altitude and partially sensitive to turbulence in adjacent layers. Bottom: Zoom on the 0 to 1 km and 1 to 5 km range of altitudes, otherwise not clearly visible.*

3.3.2 PBL Fried parameter extraction

In addition to the turbulence profile the PBL data can be used to measure the integrated seeing by determining the Fried parameter. Each acquisition gives the temporal variation of the position over the 1000 images and for each position along the edge. This provides 600 DIMM measurements per acquisition. In the case of the PBL the motion is only measured in the direction perpendicular to the Lunar limb that corresponds to the direction perpendicular to the sub-apertures separation base, hence transverse motion. For all positions along the edge, I computed the variance (σ^2) over the 1000 images. The classical relation between the Fried parameter (r_0) and the variance (σ^2) was derived in Fried & Could (1966); Tatarskii (1961):

$$r_0^{5/3} = 0.179 sec(z) \lambda^2 \frac{D^{-1/3}}{\sigma^2_{abs}},$$

where λ is the wavelength, z the zenith angle and D the aperture diameter. An expression, including the outer scale ($\mathcal{L}_0$) contribution, was derived by Ziad et al. (1994):

$$r_0^{5/3} = 0.179 sec(z) \lambda^2 \frac{[D^{-1/3} - 1.52 \mathcal{L}_0^{-1/3}]}{\sigma^2_{abs}}.$$

This method can be applied to either the top or bottom images independently. Note that when $\mathcal{L}_0$ tends towards infinity, the expression simplifies to the more general Kolmogorov's case.

Similarly, the transverse variance (σ_t^2) of the differential motion, perpendicular to the direction of the sub-apertures separation, can also be used to determine the Fried parameter. The original formula was derived by Sarazin & Roddier (1990):

$$r_0^{5/3} = \lambda^2 * sec(z) * D^{-1/3} * \frac{K_t}{\sigma_t^2},$$

with $K_t = 0.358 * (1 - 0.811 * S^{-1/3})$, and $S = \frac{B}{D}$, where D is the apertures diameter and B the separation between the two apertures. z is the zenith angle.

An updated value of the constant K_t is given in Tokovinin (2002):

$$K_t = 0.364 * (1 - 0.798 * S^{-1/3} - 0.018 * S^{-7/3});$$

This is the method I will use to measure the Fried parameter presented in Section 3.6.1.

3.4 Angle of arrival covariance - Experimental measurements

For each image, I determined the edge position using the barycenter method described in Section 3.2.6 and illustrated in Fig. 3.11. From these edge positions and for each set of two images of an acquisition we can calculate the experimental differential covariance of the AA, as illustrated in Fig. 3.18, using the following formula:

$$C^{meas}_{\Delta_\alpha}(\theta) = \langle [\alpha_T(x_i) - \alpha_B(x_i)] [\alpha_T(x_i + \theta) - \alpha_B(x_i + \theta)] \rangle,$$

where $\alpha_T(x_i)$ and $\alpha_B(x_i)$ are the vertical coordinates of the limb at an initial x_i coordinate for respectively the Top and Bottom images. $\alpha_T(x_i + \theta)$ and $\alpha_B(x_i + \theta)$ are the positions at the x coordinate along the limb separated by an angle θ from the initial position. The $\langle\rangle$ signs represent the average value for all the products corresponding to a specific separation angle θ along the edge. One can see that the larger θ, the fewer number of measurements along the finite length of the Lunar limb. After the image pre-processing, the "cleaned" images are generally between 550 and 600 pixels wide. This gives a maximum of 599 measurements for the smallest separation angle

(θ_1 = 1 pixel = 0.594") and a single measurement for the largest separation angle ($\theta_{max} \sim 599$ pixels $\simeq$ 356"). The measurement error is hence much larger for larger θ than smaller ones. In the inversion process I will weigh the fits by the number of data points for each θ. For one acquisition, I calculate $C_{\Delta_\alpha}(\theta)$ for each of the 1000 images. Then, the final differential covariance function for the acquisition is obtained by taking the average of all thousands $C_{\Delta_\alpha}(\theta)$.

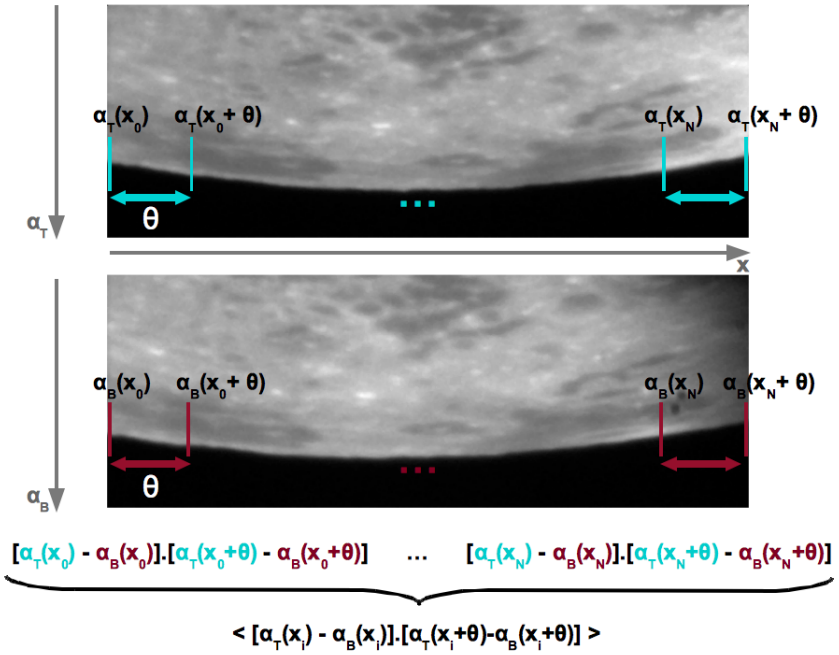

Figure 3.18: *Experimental covariance. Detail of the differential covariance measurement. I calculated the product of the difference between top (blue) and bottom(red) position at x_i and $(x_i + \theta)$ for all x_i position along the edge. The average of all products is the differential covariance ($C^{meas}_{\Delta_\alpha}(\theta)$) value at a separation θ.*

Using both, measured and theoretical, covariances one can reconstruct the turbulence. I generated an atmospheric profile (h_i, Δh_i, $C_n^2(h_i)$ and $\mathcal{L}_0(h_i)$) that I used to compute the corresponding theoretical covariance function before comparing it to the measured one.

I use a simulated annealing (SA) algorithm (Kirkpatrick et al., 1983), that I developed under Matlab, to find the best fit value. The SA algorithm is a random-search technique which exploits an analogy with thermodynamics and the way in which a metal cools and freezes into a minimum energy, assimilated here to the global minimum. Starting from an initial set of $C_n^2(h_i)$ values I computed the initial cost function ($E_{n=0}$) between the theoretical and measured covariance: $E_{n=0} = \sum_\theta [C^{theo}_{\Delta_\alpha}(\theta) - C^{meas}_{\Delta_\alpha}(\theta)]^2$. Then for each subsequent iteration (n), I applied a small variation to the previous $C_n^2(h_i)$ values, calculated the new cost function, and then computed the cost difference $\Delta E = E_{n+1} - E_n$. If it is negative, the cost decreases and I keep the new set of parameters. If the cost increases, ΔE is positive, I do not systematically reject the solution but accept it with a probability $p = e^{(-\Delta E/T)}$. This cost increasing acceptance probability allows to explore the full parameter space and avoid to get stuck in a local minimum. This acceptance probability is set by the "temperature" parameter T, in analogy with thermodynamics. The SA algorithm starts with a high initial temperature to explore a wide area of the parameter space and a "cooling" schedule slowly lowers the "temperature" towards the reduction of the search around the global minimum. The search stops and the current best set of $C_n^2(h_i)$ values are saved as the best fit result, when, at a fixed "temperature", no improvement to the cost function can be made. A similar technique was also used in Maire et al. (2007).

3.5 Simulation

3.5.1 Covariance Simulations

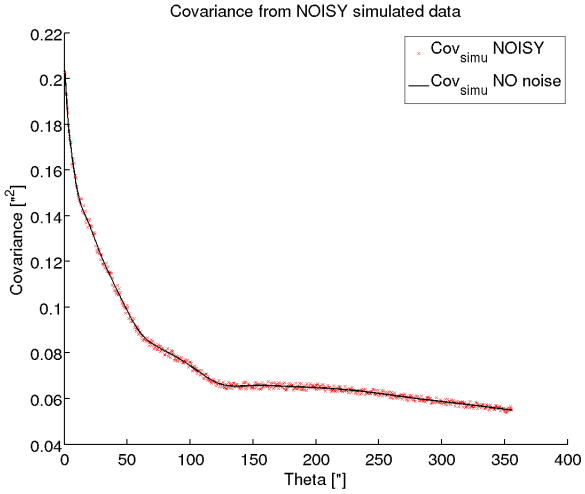

Figure 3.19: *Simulated covariance for 33 layers with a profile given in the second column of Table 3.2 (simu). The black line shows the perfect covariance overlapped to the noisy covariance (red crosses) produced by adding Gaussian noise to the perfect curve.*

In order to probe the reconstruction method, I simulated differential covariances for a profile with altitudes matching the reconstruction grid. I looked at two cases, one with a perfect covariance curve and one with a noisy covariance curve. The noisy data were produced from a perfect covariance to which I added Gaussian noise (Fig. 3.19).

The reconstruction results are shown in Fig. 3.20, with the input simulated data in red and reconstruction in blue. The covariances are shown on the left while on the right we have the corresponding turbulence profiles. For both graphs, the mean relative error between the input data and the output reconstruction are given. The top two panels correspond to the perfect covariance case while the bottom ones are for the noisy data case. In addition, the relative strength of the layers from the simulated and reconstructed profiles are reported in Table 3.2.

The relative error of the reconstruction from a perfect data set seems negligible on the covariance, with a value below 10^{-13}%, however, this still reflects as a 1.57% relative error on the reconstructed profile. In the case of the noisy data set, the relative error on the reconstructed covariance is 0.45%, which reflects as 13.5% on the reconstructed profile. The error on the profile is more important on the higher layers of the atmosphere. At higher altitudes, the covariance peak from different layers get closer to each other (Fig. 3.14). This implies that the response of the reconstruction in the higher layers is more sensitive to turbulence in adjacent layers. This greater sensitivity to turbulence in adjacent layers is seen as wider triangles for the higher altitudes in Fig. 3.17. As a result, I expect to see some error coming from a wrong redistribution between adjacent layers. In order to evaluate this effect, I compared the reconstructed and original simulated profile after applying a smoothing over three consecutive layers: $C_n^2(h_i) = \frac{1}{3}\sum_{k=i-1}^{i+1} C_n^2(h_k)$. After smoothing, the relative error between the profiles goes down to 4.3%, confirming that a large part of the error is coming from a wrong redistribution between adjacent layers. Also, in some cases, poorer optimization of the algorithm could generate convergence issues and additional error in the redistribution.

Overall, when running a set of 100 noisy data simulations, the mean relative error on the profile reconstruction is 14% for the full range of altitude, 25% for the 5 to 24 km range and 5% for altitudes below 5 km.

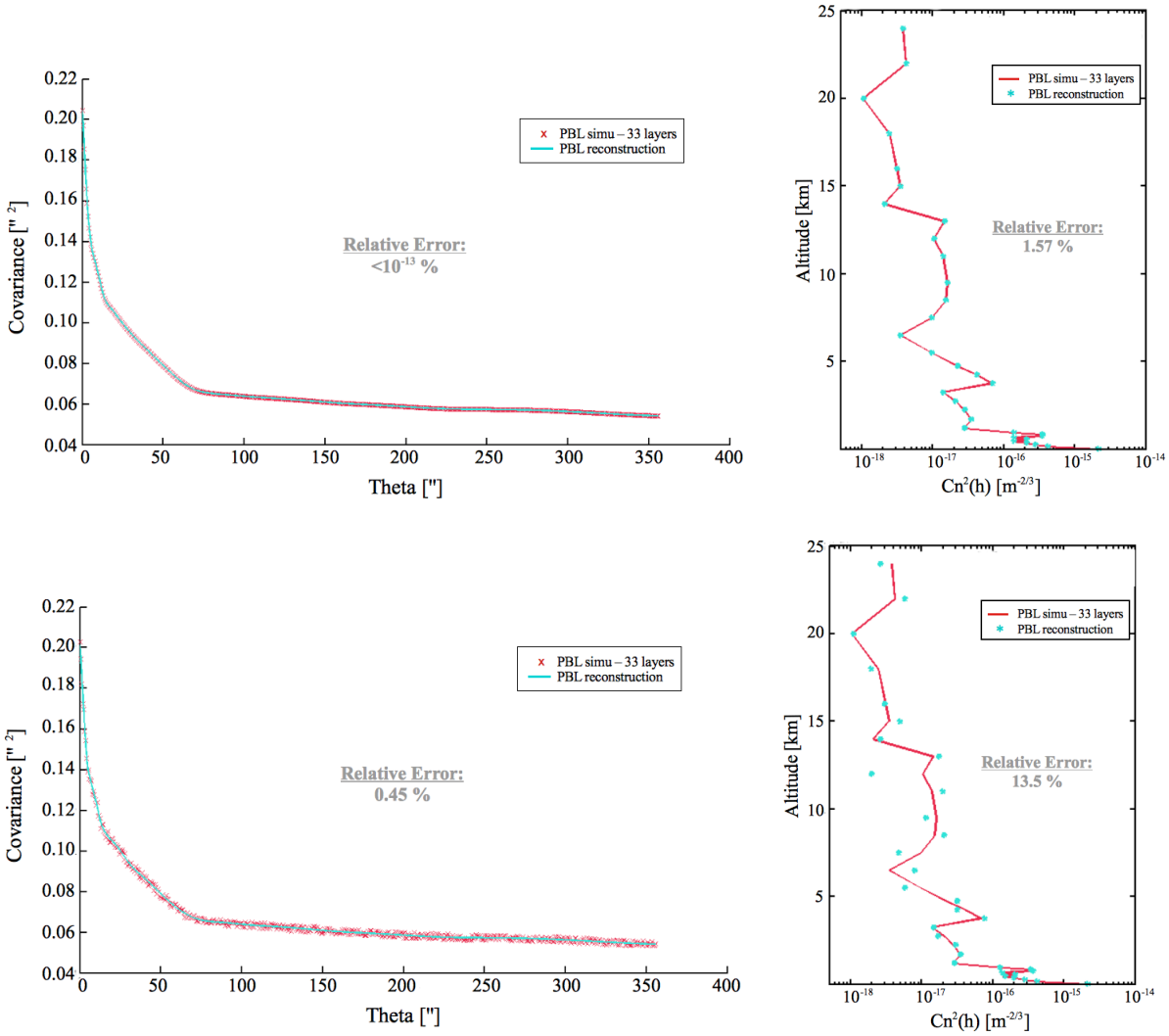

Figure 3.20: *Example of simulated covariance and the best fit from the reconstruction method in the case of a 33 layers model matching the reconstruction grid. Left: Covariance fit showing the simulated covariance (red circle) overlapped with the reconstructed ones (blue line). Right: Corresponding profiles, respectively in red and blue. Top: reconstruction from a perfect covariance curve (black line in Fig. 3.19). Bottom: reconstruction from a noisy covariance curve (red crosses in Fig. 3.19). The simulated and reconstructed profiles relative turbulence strength are given in Table 3.2. For each graph, the value of the relative error between the simulated data and the reconstructed ones are provided.*

As a second test, I also looked at a more realistic case where the simulated profile has a different number of turbulent layers at altitudes that are not matching the reconstruction grid. For this simulated profile, I also added noise to a perfect theoretical covariance. I used a 25 layers profile. The layers altitude and relative strength are reported in the last columns of Table 3.2, along with those from the reconstruction. Fig. 3.21 shows the simulated and reconstructed covariance and corresponding profiles. Here again, I found a fairly good redistribution of the turbulence from the simulated profile onto the reconstruction grid.

Table 3.2: *Reconstruction Profile from covariance simulations.*

Altitude [km]	**Relative strength of the turbulence layers**				
	33 simulated layers			25 simulated layers	
	simu	recon	recon (NOISY)	simu	recon (NOISY)
0.01	31	30.6	30.9		33.8
0.03				41	
0.15	6	6	6		12
0.2				3	
0.25	4	4	4		3.1
0.275				2	
0.325				4	
0.35	3	2.9	2.9		3.3
0.425				6	
0.45	2	2	2.2	5	12.3
0.475				4	
0.55	3	3	1.9		0.2
0.65	2	2	3.7	3	2.1
0.75	5	5	3.8		2
0.8				4	
0.85	5	5	6		4.8
0.9				5	
0.95	2	2	2		5.3
1				3	
1.2	2	2	1.4		1.8
1.3				1.2	
1.7	2.5	2.5	2.4	0.8	2
1.9				1	
2.25	2	2	2.1		0.5
2.75	1.5	1.5	0.8		0
3				0.5	
3.25	1	1	0.7		0.8
3.5				1.4	
3.75	5	5	6.6		2.2
4				2.4	
4.25	3	3	3.3		1.2
4.75	1.6	1.6	0.4	2.6	2.5
5.5	1.4	1.4	0.5	3	2.8
6.5	0.5	0.5	0.9		1
7				2.1	
7.5	1.4	1.4	1.5		1.7
8.5	2.2	2.2	4.7	0.8	0
9.5	2.3	2.3	2.3		0.5
11	2	2	0.2	0.9	0.3
12	1.5	1.5	0.3		1
13	2.1	2	0.8	1	0
14	0.3	0.3	4.6		0.5
15	0.5	0.5	0.4		0
16	0.9	0.9	0.2		0.6
17				1.2	
18	0.7	0.7	0.3		0.6
20	0.3	0.9	0.2		0
22	1.2	1.2	0.4		0
24	1.1	1.1	1.6	1.1	1.1

However, those results use perfect simulated covariance functions, with an addition of Gaussian noise, injected as input in the inversion algorithm. This is a very simplified model of the system response to measured noisy covariances. In order to test the inversion on more realistic synthetic data, I simulated a series of PBL-like images using the end-to-end adaptive optics simulation tool CAOS (Code for Adaptive Optics System, Carbillet et al. (2005)) in seeing-limited mode.

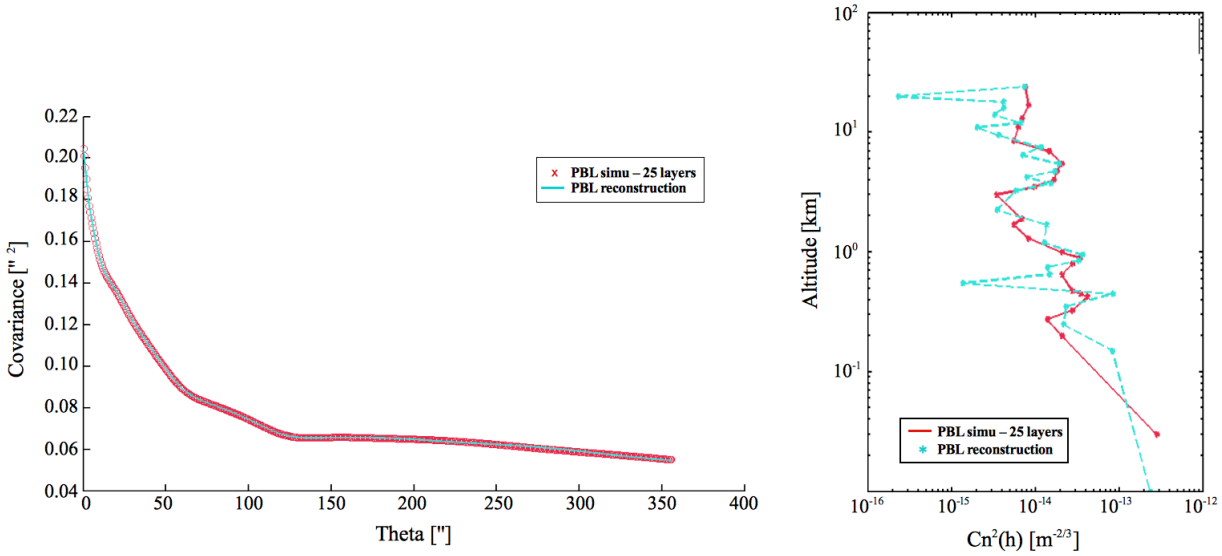

Figure 3.21: *Example of simulated covariance and the best fit from the reconstruction method in the case of a 25 layers model not necessarily matching the altitudes of the reconstruction grid. Left: covariance fit showing the simulated covariance (red circle) overlapped with the reconstructed ones (blue line). Right: Corresponding profiles, respectively in red and blue. The simulated and reconstructed profiles relative turbulence strength are given in Table 3.2 (columns 5 and 6)*

3.5.2 Images Simulation

Synthetic PBL images were simulated and used to test the overall data pre-processing, edge detection method and profile reconstructions. I used the CAOS application to produce a synthetic data set. All telescope parameters were chosen to be identical to the system used in Sutherland. The wavelength was set to $0.5\mu m$ where the spectral response of the camera is maximum. To obtain results as close to the experimental setup as possible I used an image generated by the instrument as input.

Table 3.3: *Simulation Input Profiles.*

Profile number	Layers altitude [km]	Input r_0 [cm]	Retrieved r_0 [cm]
1	0 and 0.1	7.5	7.3
2	0 and 0.3	7.5	7.4
3	0 and 0.5	7.5	7.1
4	0 and 1	7.5	7.5
5	0 and 2	7.5	7.3
6	0 and 4	7.5	7.8
7	0 and 6	7.5	7.6
8	0 and 8	7.5	7.2
9	0 and 12	7.5	7.9
10	0 and 16	7.5	7.1

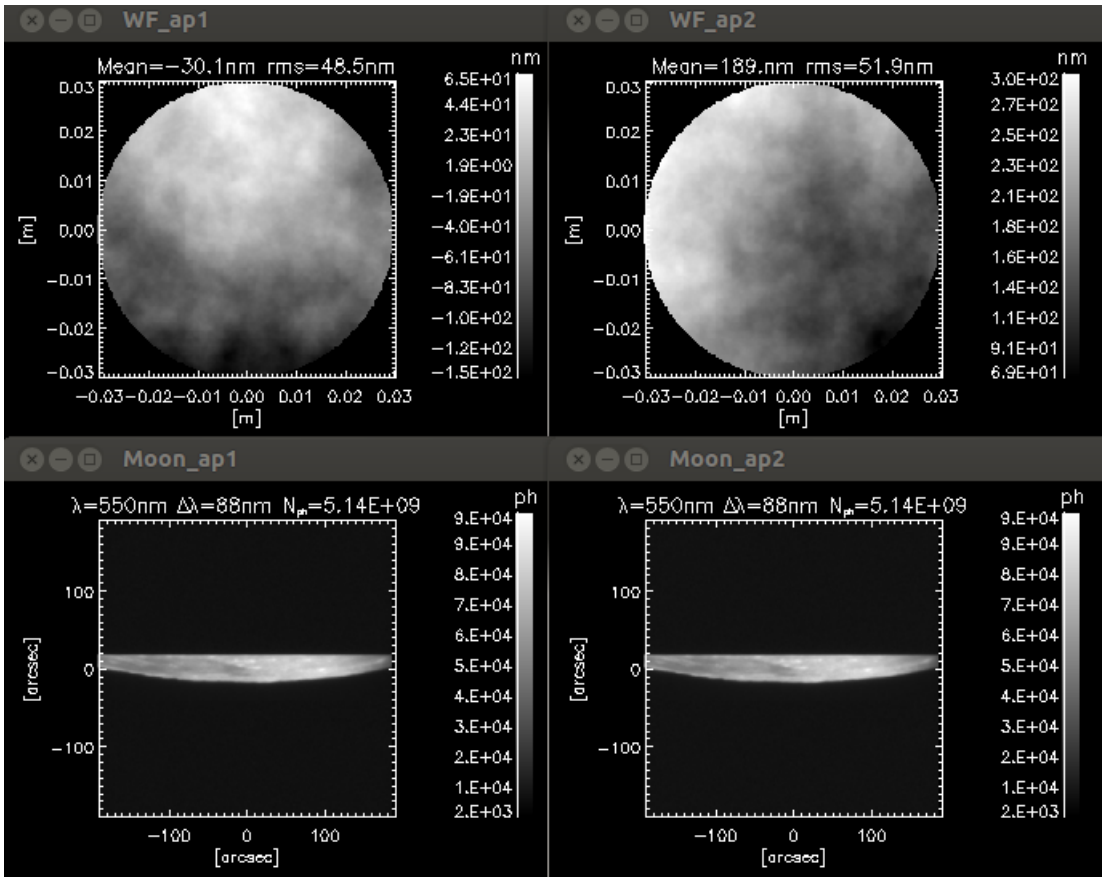

Figure 3.22: *Example of simulated PBL Moon images with CAOS used in seeing-limited mode with an atmosphere model made of two turbulent layers. Top: Pupil image of the turbulent wavefront as seen by the 2 sub-apertures of PBL, positioned with a 0.266 m separation in the simulation. Bottom: resulting Moon images at the focal plane of the telescope. Both channels are looking at the same source. Here I used one of the real PBL images as an extended source for the input of the simulation.*

In the CAOS simulation, I use the PBL image as an extended source. To lower the computational power I restricted the images to a 600x50 pixels around the Lunar limb. Turbulence screens were generated for a two layered atmosphere, with a r_0 of 7.5 cm and a $\mathcal{L}_0$ of 20 m. For the telescope entrance, I created 2 channels with a 6 cm aperture size, one at -0.133 m from the optical axis and the other one at +0.133 m, reproducing the 0.266 m base of the PBL setup. Each channel looks at the same source and same turbulent atmosphere but from a different angle. Fig. 3.22 shows the turbulence as seen by the two sub-apertures (top images) and the images produced after going through the turbulent layer and telescope pupil (bottom images).

I repeat this procedure 1000 times, as per the number of images per acquisitions in the PBL measurement process. I then applied the data processing method to detect the edge position, calculate the covariances and retrieve the profiles from the simulated annealing algorithm. The profiles input and estimated r_0 values are shown in Table 3.3, while the reconstruction is represented in Fig. 3.23. Here I simulated a series of profiles with 2 turbulent layers, one at 0 km and the other at a higher altitude, as shown in the second column of Table 3.3. For each profile, r_0 is set to 7.5 cm and the turbulence is located for 80% in the lower layer and 20% in the higher one. The retrieved profiles and estimated r_0 are in good agreement with the input data, validating the pre-processing and inversion method.

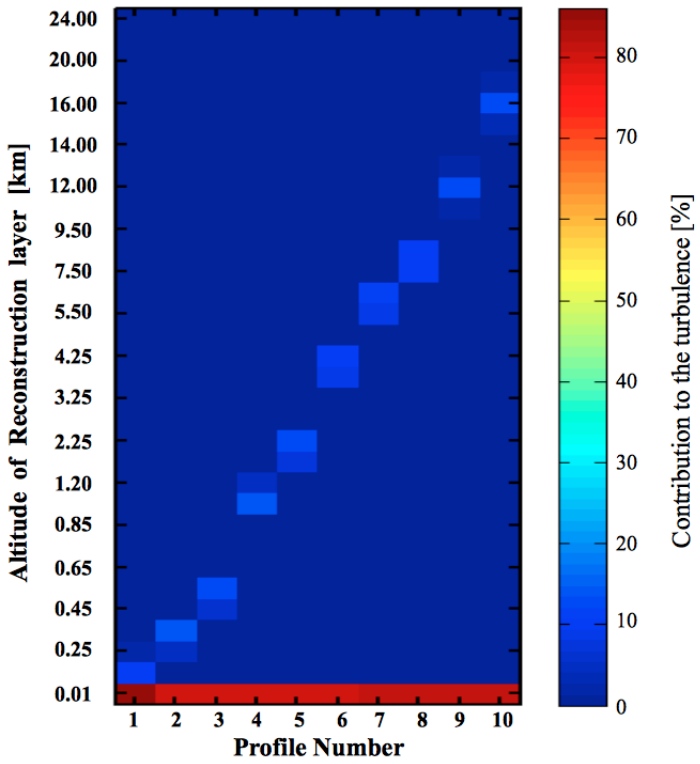

Figure 3.23: *Turbulence profile reconstructed from simulated images produced with the CAOS using 2 layers atmosphere models. The input profiles are listed in Table 3.3. The color indicates the relative turbulence strength in percentages.*

3.6 PBL results - Sutherland August 2011

The PBL was deployed at the Sutherland Observatory in South Africa in August 2011. During the PBL observing campaign, we also had a MASS-DIMM and a GSM running alongside with it. Fig. 3.24 shows the instrument setup. For all operating night, I was able to measure the seeing and compare it to the DIMM and GSM measurements while I compared the profile measurements to the MASS FA profiles.

3.6.1 Fried parameter measurements

I obtained the equivalent of a DIMM measurement for each field angle along the Lunar limb and the corresponding r_0 value for the acquisition is taken as the mean of all values along the limb. An example of Fried parameter measurement is shown in Fig. 3.25. On the left-hand-side one can see the measured Fried parameter for all position along the Lunar limb for the acquisition done at 18:46:09 on the night of the 11/08/2011. As given in the legend, the mean value of the Fried parameter for this acquisition was 9.45 cm. The seeing measurements throughout the night along with the corresponding DIMM and GSM measurements are represented on the right hand-side.

From the figure, we can see that PBL and DIMM seeing measurements trend agrees very well, despite the overall better seeing measured by PBL. One explanation can come from the height difference between the DIMM and PBL setups. The DIMM entrance aperture was at around 1.5 m from the ground while the PBL one was at around 3 m. Hence, I expected PBL to measure a higher r_0 value. In addition, even when fully opened, the sliding roof of the MASS-DIMM enclosure can still cause surface turbulence worsening the seeing as seen from the instrument. On the other hand, I expected the GSM and PBL measurements to agree more. There are 3 factors that could have contributed to the discrepancy between PBL and GSM measurements. Even if both GSM

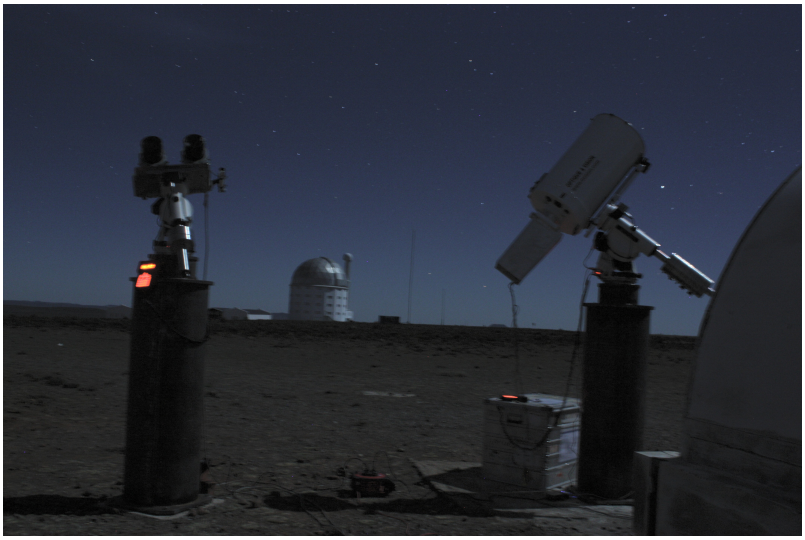

Figure 3.24: *PBL and GSM setup at Sutherland. PBL (on the right-hand-side of the picture) and GSM (on the left-hand-side of the figure) on 1.5 meter piers next to the sliding roof structure hosting the MASS-DIMM. One can also see the SALT in the background.*

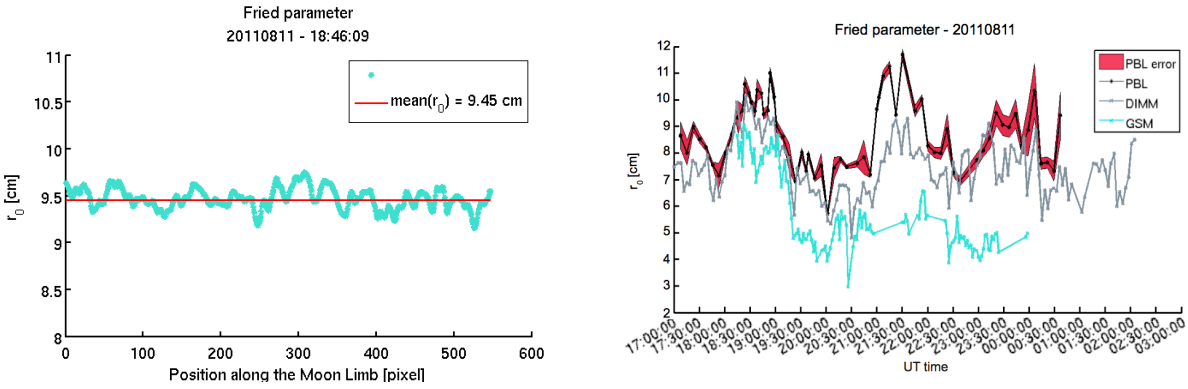

Figure 3.25: *Fried parameter measurement. Left: measurements of the Fried parameter for all positions along the Lunar limb on the night of the 11/08/2011 at 19:46:09 with an average value of 9.45 cm. Right: Instrument comparison of the measured seeing on the night of the 11/08/2011 with PBL (red), GSM (green) and DIMM (grey).*

and PBL sits on a 1.5 m pier the GSM entrance aperture is slightly lower than that of PBL due to the instrument sizes. Also, they have different lines of sight, as can be seen in Fig. 3.24, and hence are not sensing the exact same part of the atmosphere. More importantly, and probably the main error contribution, we had contrast issues on the GSM during the campaign due to cirrus clouds, humidity and frost forming on the unit lenses. GSM measures flux modulations and hence when there is light loss due to external factors, GSM measurements become unreliable.

3.6.2 Turbulence Profiles

The measured (red cross) and fitted (blue line) covariances for the acquisition done at 19:01:11 on the night of the 11/08/2011 are shown in Fig. 3.26 (left). The fitted covariance function corresponds to the best fit turbulence profile for that measurement. The retrieved profile is shown on the right-hand-side of Fig. 3.26. In order to verify both the profile reconstruction and seeing measurement with PBL I compared the seeing value obtained in the DIMM-mode (r_0^{DIMM}), as presented in Section 3.6.1, and the value calculated from the full integration of the profile ($r_0^{profile}$). For the night of 11/08/2011 at 19:01:11 $r_0^{DIMM} = 9.04$ cm, as compared to $r_0^{profile} = 8.99$ cm.

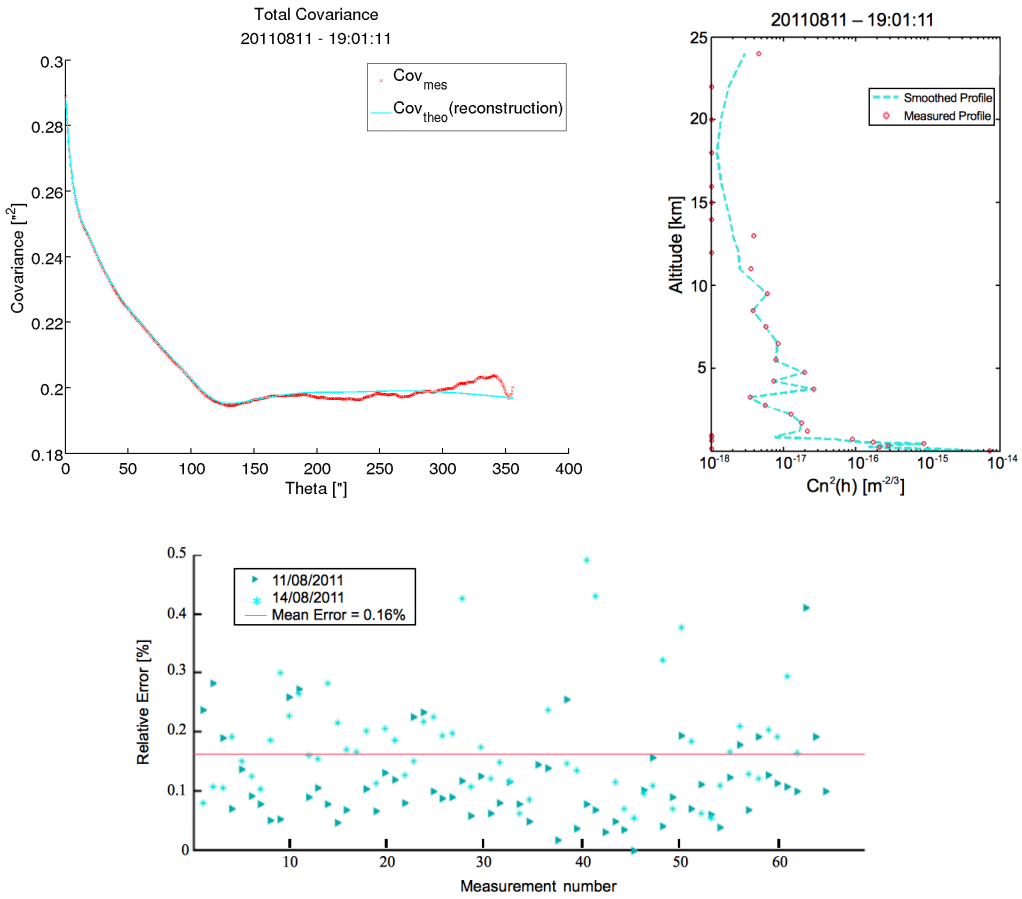

Figure 3.26: *PBL turbulence profile results. Top Left: measured covariance (red circles) and the best fit of the theoretical covariance (blue line) on the 11/08/2011 at 19:01:11. Top Right: retrieved PBL turbulence profile from the best fit covariance. Bottom: Relative error between measured covariances and fitted ones for 125 measurements over 2 nights. The mean error value is 0.16%.*

In addition, I compared the PBL results with the ones from the MASS-DIMM instrument. I calculated r_0 from the integrated MASS profile which gives a value of 25.7 cm while integrating the corresponding top layers of the PBL profile (0.5 to 24 km) I obtain a r_0 of 27.1 cm. Both instruments agree well on the amount of turbulence located in the FA. However, those are comparisons on a single acquisition and to have a sense of how well the data reconstruction performs I show on the bottom graph of Fig. 3.26 the value of the relative error between measured covariance and reconstructed ones for 125 measurements over 2 nights. The mean relative error value is found to be 0.16%. Further verification is done by instrument cross comparison with MASS results on a full night set of data .

Fig. 3.27 shows the turbulence profile evolution throughout the night on the 11/08/2011 from both PBL and MASS measurements. The top figure shows the full PBL profile with 33 layers. For easier comparison with the MASS profile I binned the PBL results according to the MASS altitude grid. The plain grey line overlapped to the PBL profile on the top figure shows the lower altitude limit of the MASS instrument, while the dotted lines above it represent the boundaries of the altitude range sensed by each of the 6 MASS layers. Note that those boundaries are just indicative as I did not perform a linear binning but used the triangular weighting function of the MASS instrument (Fig. 3.27, top right). I also indicated those boundaries on the MASS weighting function graph.

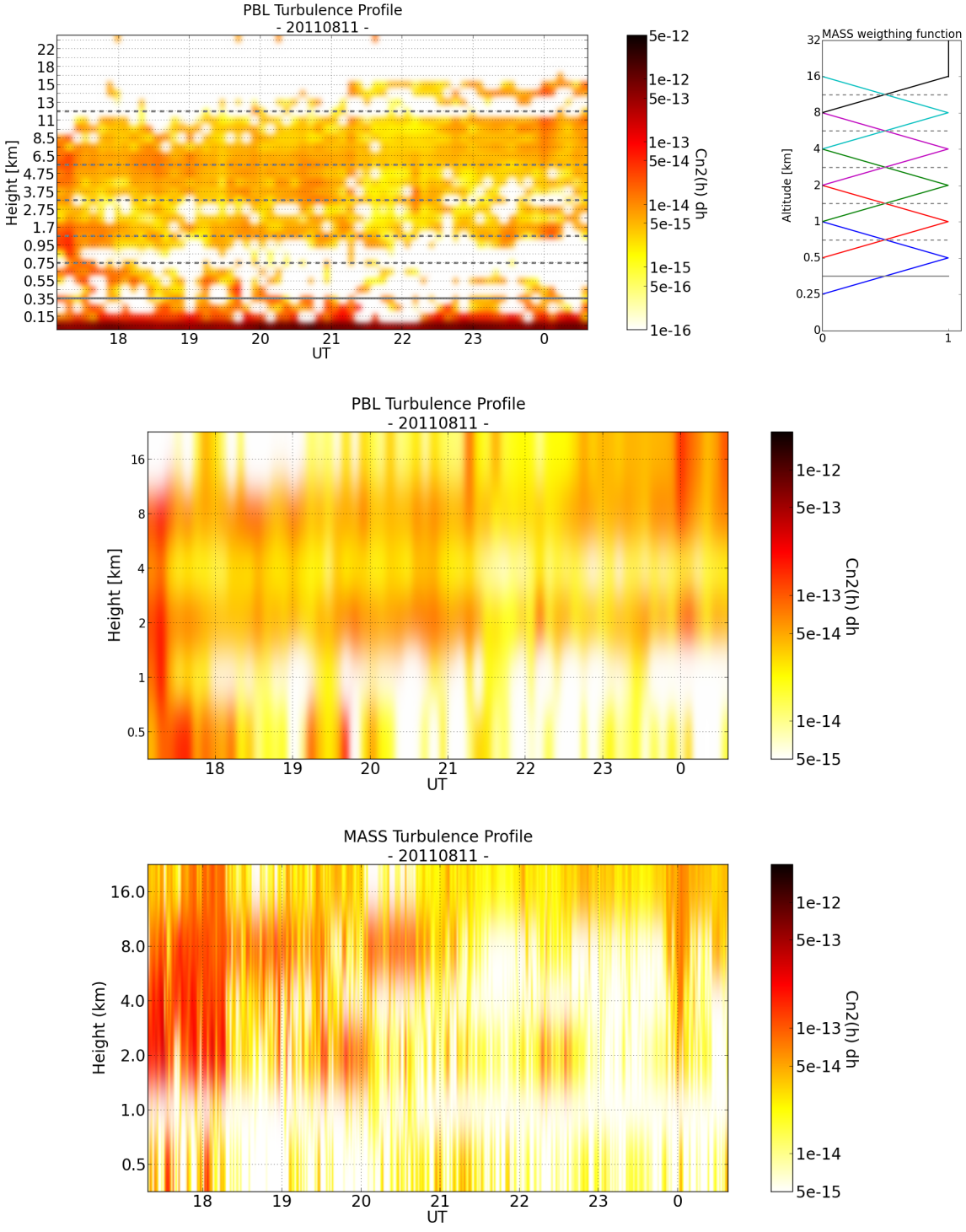

Figure 3.27: *Turbulence profiles for the night of the 11/08/2011. Top left: PBL measurements. Top right: MASS weighting functions used to re-bin the PBL data for comparison with MASS. On both figures, the dotted grey lines show the average transition between each MASS bin. The plain grey line shows the lower limit of MASS altitude. Middle: Resulting PBL profile after binning. Bottom: MASS profile.*

Comparing the re-binned PBL (Fig. 3.27, middle) to the MASS profile (Fig. 3.27, bottom), one can see a fairly good agreement between the two. Before 18.00 UT, we see strong turbulence around 500 m, and from 2 to 8 km. Later on and until 21.00 UT, the turbulence is mainly located between the 2 and 8 km layers. And then, after 23.00 UT the 16 km layer become dominant especially around 00.00 UT.

Comparing the full PBL profile (Fig. 3.27, top) to the one matching the MASS altitude grid (Fig. 3.27, middle), one can clearly see the advantage of PBL over MASS. Not only PBL delivers a much higher altitude-resolution but it also resolves the ground layer turbulence below 500 m unseen by the MASS instrument.

3.7 Conclusion

The PBL method uses differential measurements making it insensitive to tracking errors or telescope wind shake. Moreover, the use of the continuous Lunar limb provides a large range of separation angles, as compared to the double star used for SLODAR, allowing for the high altitude-resolution of the turbulence profile. The large number of separation angles available also permits a characterization of both the ground layer and free atmosphere where most of other instruments are tuned to determine one or the other. The method was validated by both testing it on simulated synthetic data and cross comparison with MASS-DIMM and GSM results.

Simulations showed that the reconstruction is accurate within 14% of the real value, with higher errors for altitudes above 5 km, mainly due to a wrong redistribution between adjacent layers. Other reconstruction algorithms are investigated to try and lower the error.

The PBL measurement campaign at the Sutherland site was limited to 3 weeks in August 2011 due to the fact the instrument was on loan from the University of Nice for that period, after which it returned to Nice where it is now permanently set up at the Calern Observatory. However, those 3 weeks provided us with enough data to conduct instrument cross-comparison and validate the reconstruction method. The comparison to DIMM measurements for the r_0 value and MASS for the $C_n^2(h)$ profile, shows very good agreement in both cases. In addition, a first measurement of $\mathcal{L}_0(h)$ profile, gave promising results while it still needs some work and cross-comparison with other instruments to validate the method.

In principle, both θ_0 and τ_0 can be retrieved from PBL data. This is something that could be implemented in further data analysis. Also, more work is currently being done in terms of speeding up the data processing in order to have an automated system that can produce real-time measurements.

Chapter 4

AN ADAPTIVE OPTICS SYSTEM FOR SALT: A CONCEPT STUDY

Contents

Since its first implementation on a telescope in 1989 (Merkle et al., 1989, 1991), adaptive optics (AO) systems have come into common usage at most of the major large telescopes worldwide. SALT and HET are the only 8+ m class telescopes that have not implemented an AO yet. A first investigation of a potential AO correction for SALT was presented in Kenworthy et al. (2008). However, it focused on tip-tilt correction only and was based on the optimistic historical median seeing value of 0.92" (Erasmus, 2000). Nonetheless, those simple simulations showed that even a tip-tilt only correction could provide significant gains in encircled energy at wavelengths beyond 1 micron. In this chapter, I explore in further details the potential improvements that a full AO correction system could bring to SALT.

SALT (Buckley, 2008) is the largest optical telescope at the Sutherland observatory. It was built based on the design of its twin the Hobby-Eberly Telescope (HET), at the McDonald Observatory in Texas (Ramsey et al., 1994; Sebring et al., 1994; Sebring & Ramsey, 1997; Ramsey et al., 1997). SALT is an 11 meter spherical segmented hexagonal telescope. Its primary mirror consists of 91 one-meter segments. As part of its design, it has a fixed elevation which was set at 37^o from zenith. The change of 35^o to 37^o as compared to HET was set for observations of the SMC. The tilt is a compromise to maximize sky coverage while keeping the airmass reasonably low. As for the pointing and tracking, the telescope azimuth angle can be adjusted prior to each observation by lifting the structure by the means of eight air bearings, however, the azimuth will remain fixed during an observation. The pointing and tracking are then done with the tracker unit at the prime focus of the telescope in an "Arecibo-like" fashion. The tracker has six degrees of freedom allowing

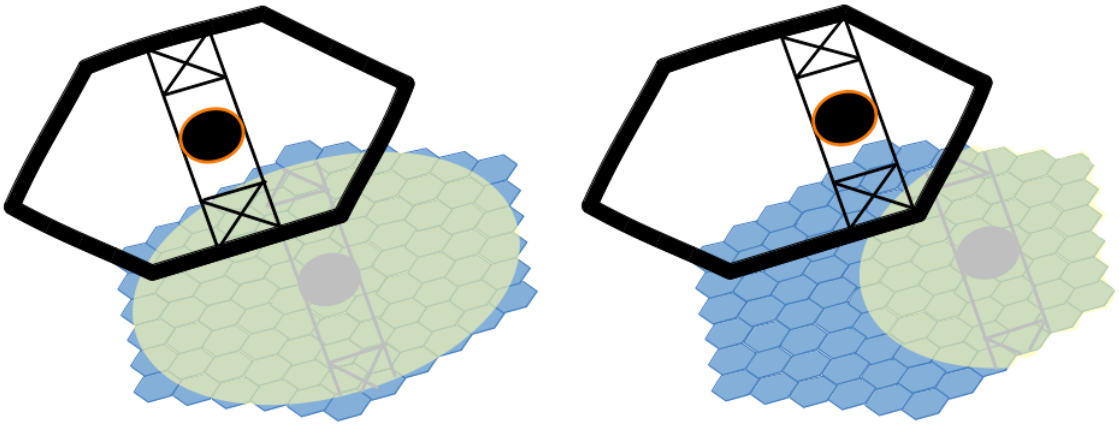

(a) (b)

Figure 4.1: *Schematic of SALT primary mirror and tracker. (a): pupil illumination when the tracker is centered. (b) pupil illumination at the far end of the tracker course.*

it to follow an object as it crosses the region of sky covered by the SALT viewing window. One consequence of this design is a limited tracking time. Depending on the object declination, a track can last one to three hours. To best optimize the telescope time as a function of the target visibility windows, SALT is entirely queue-scheduled. Another consequence of SALT specific design is that the size and shape of the pupil changes throughout an observation as the tracker moves (Fig. 4.1). When the tracker is centrally located, the effective collecting area of the telescope is equivalent to the full size of the primary mirror minus the tracker obscuration which corresponds to 55 m^2. At the tracker outermost position, the effective collecting area is 40 m^2.

The tracker holds the payload including the spherical aberration corrector (SAC, O'Donoghue & Swat (2002); O'Donoghue et al. (2010); Crause et al. (2012)) and the two first-generation prime focus instruments: the SALT imaging camera (SALTICAM, O'Donoghue et al. (2006)) and the Robert Stobie Spectrograph (RSS, Burgh et al. (2003); Kobulnicky et al. (2003)). In addition an auxiliary port instrument was installed in early 2009: the Berkeley Visible Imaging Tube (BVIT, Siegmund et al. (2008)). A fiber-fed instrument was delivered and installed in September 2013, the High-Resolution Spectrograph (HRS, Barnes et al. (2008); Bramall et al. (2010)). After a science verification period, HRS became fully operational in April 2014.

SALTICAM is an imaging camera that operates in the UV-visible range (320-900 nm) with a 10' field of view (FOV). Although mainly used as an acquisition camera, it also offers full science-grade capabilities with broad and narrow band filters as well as a high-speed imaging mode. Further photometric capabilities are available with BVIT, a photon counting and time-tagging detector system designed for very high time resolution photometry.

On the spectroscopy side, RSS operates at visible wavelengths between 320 and 950 nm. RSS provides a wide range of different operating modes. It offers imaging, long slit, high-speed and multi-object spectroscopy (MOS) as well as Fabry-Perot imaging spectroscopy, spectropolarimetry and imaging polarimetry. The suite of Volume Phase Holographic (VPH) gratings allows spectral resolution ranging from R ~250 to 5500 for a 1.2" slit and up to R ~9000 with 0.6" slit. The MOS mode uses carbon-fiber laser-cut masks that can hold up to ~30 objects at the same time. The Fabry-Perot mode offers resolution from R ~320 to 9000.

The second spectrograph, HRS, is a fiber-fed echelle spectrograph operating in the visible. It has two channels, a "blue" arm covering the 370 to 550 nm wavelengths range and a "red" arm covering the 550 to 890 nm part of the spectrum. It is a single object spectrograph using pairs of fibers, one for the science target and one for the sky background. The fiber sizes available are 1.56" and 2.23", and it offers four resolution modes. The low resolution mode uses unsliced images

with the 2.23" fiber providing spectral resolutions of R 15000 for the blue arm and R 14000 for the red arm. The medium resolution mode uses image slicers with the 2.23" fiber providing spectral resolutions of R 43000 for the blue arm and R 40000 for the red arm. The high-resolution mode uses image slicers with the 1.56" fiber providing spectral resolutions of R 67000 for the blue arm and R 74000 for the red arm. Lastly, the high stability mode uses image slicers with the 1.56" fiber providing spectral resolution of R 67000 for the blue arm and R 65000 for the red arm (Crause et al., 2014).

Despite the imaging and photometry capabilities offered by SALTICAM and BVIT, SALT is primarily designed for spectroscopy. For the concept study of an AO system for SALT I will focus on the spectroscopic aspects. Typically, the performances of a spectrograph are evaluated in terms of wavelengths coverage ($\Delta\lambda = N_r.\delta\lambda$) and spectral resolution ($R = \frac{\lambda}{\delta\lambda}$), where $\delta\lambda$ is the spectral resolution element corresponding to the projected size of the slit on the CCD at the focal plane and N_r is the number of spectral elements that can be fitted onto the CCD. The resolving power can also be expressed as a function of the spectrograph and telescope dimensions:

$$R = \frac{\lambda A d_{cam}}{\phi f_{Tel}} \frac{f_{col}}{d_{col}} = \frac{\lambda A d_{cam}}{\phi D_{Tel}}, \tag{4.1}$$

where λ is the observing central wavelength in Å, A is the dispersion in Å.arcsec^{-1}, ϕ is the projected angular size of the slit in arcseconds, d_{cam}, d_{col} and D_{Tel} are respectively the diameters of the camera, the collimator and, the telescope in meters and, f_{col} and f_{Tel} are the focal lengths of the collimator and the telescope in meters.

Independently of the choice of slit, dispersing element, collimator and camera, in conventional seeing limited spectrographs, the best resolution is limited by the size of the telescope diameter. As Eq. 4.1 suggests, the larger the telescope diameter, the lower the resolution. The image delivered after AO correction tends toward the telescope diffraction limit. While for conventional spectrographs the entrance slit is determined by the size of the seeing disc, it is inversely proportional to the telescope diameter when AO correction is applied. Hence, there is a telescope diameter/resolution coupling in seeing limited mode, while the resolution is not a function of the telescope diameter in AO-fed spectrographs. There are a number of advantages in using AO-assisted spectrographs. The smaller size of the AO-corrected image, allows the use of smaller slits resulting in smaller $\delta\lambda$ without additional light loss at the entrance slit (Ge et al., 1998). For a given spectrograph dimensions and characteristics, the AO-assisted one, with its smaller image size, can pack a larger number of cross-dispersed orders onto the CCD as compared to the traditional seeing limited one. As a result, it can provide a greater wavelength coverage over similar spectral resolution. Also, the use of smaller slits reduces the sky background giving access to the study of fainter objects (Pasquini et al., 1998). Moreover, since the PSF size is reduced, the spatial resolution over the FOV increases and smaller spatial scale structures can be studied. Overall AO-assisted spectrographs can use slower optics than seeing limited ones to deliver the same performances. This lead to the reduction of the overall dimension and cost of a spectrograph when supported by AO correction as compared to a seeing limited one with similar resolving power and wavelength coverage.

The requirements for spectroscopy in terms of PSF characteristics, however, are not quite the same as for imaging. AO systems of first generation were mainly correcting the low spatial frequency wavefront errors, delivering PSF with diffraction limited core, well suited for high-resolution imaging. However, while providing small full width at half maximum (FWHM) value within small corrected fields and relatively high Strehl ratios, the fraction of energy within a small angular section of the PSF central part was still very low, and most of the energy remained within the seeing limited halo of the PSF. As illustrated in Fig. 4.2, the AO-corrected PSF is made of two components: a diffraction limited core (blue) and a broad seeing limited halo (grey). In the particular case of spectroscopy, we are not so much interested in having diffraction limited images (i.e. high Strehl ratios) as we are in getting more energy in a given slit or fiber. The opening of a new

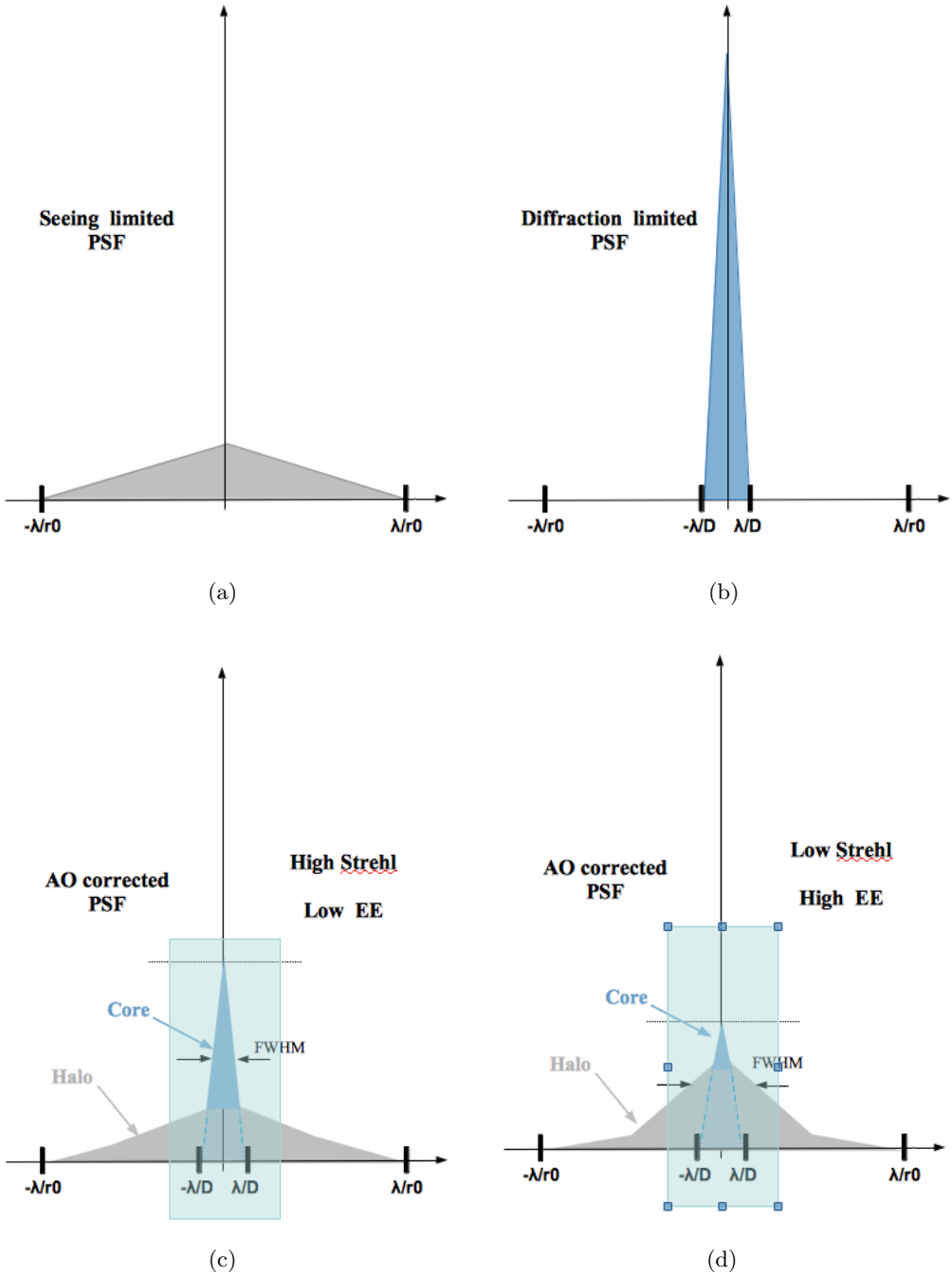

Figure 4.2: *PSF shapes schematic. (a):seeing limited PSF. (b):diffraction limited PSF. The bottom figures represent AO-corrected PSFs with its 2 components, the diffraction limited core (blue) and the seeing limited halo (grey), overlap with a shaded green area representing a given aperture. (c):low order correction providing high Strehl ratio but low EE. (d):correction of higher order providing higher EE despite a lower Strehl.*

era in spectroscopy at large ground-based telescopes, only came with later AO systems and their capability to correct for the higher spatial frequency of the wavefront errors.

As presented in Section 1.6, there are different metrics one can use to evaluate the performances of an AO system. Those allow to take into account both the AO-corrected PSF shape (Fig. 4.2) and the specific needs of the instrument fed by the AO system. For the 10 m class telescopes, as SALT, the slit size that one is considering for an AO-fed spectrograph could be significantly smaller than the seeing disc, by a factor of 10 or more, but still much larger than the diffraction limit of the telescope given that it is of the order of 10^{-2} arcseconds, considering that the primary mirror segments are phased. Hence, as illustrated in Fig . 4.2-d, the encircled (EE) or enslited (ESE) energy are more appropriate metrics to study the spectroscopic performances of an AO system. Looking at the EE and/or ESE within a given aperture size gives us a measure of the fraction of the total energy concentrated within it. While it might not correspond to the highest Strehl ratio, as required for high-resolution imaging, it is more suited for spectroscopy. Fig. 4.2 illustrates the two cases: a PSF shape providing high Strehl but low EE (c) and one with high EE but low Strehl (d).

This Chapter is dedicated to the overall dimensioning of an AO system for SALT. As explained in Ch. 1, no AO system can deliver a perfect correction of the distorted wavefront (WF). Designing an AO system relies on finding the best combination of parameters that define the different component of the system, namely the wavefront sensor (WFS), the deformable mirror (DM) and the control loop (CL). The optimization process consists in finding the optimal trade-offs between the different errors that contribute to the final error budget underlying the residual wavefront distortions remaining after AO correction. Ch. 1 presents a full description of the errors and their relation with the different component of an AO system. At this stage of a high level dimensioning and performance study, I considered a fairly common AO system setup using a Shack-Hartmann wavefront sensor (SHWFS) and a coupling with the DM that assumes Fried geometry (Fried, 1977) on a linear scale with N+1 actuators for N sub-apertures.

Such an optimization requires that one defines a system model and performs simulations in order to explore and evaluate different configurations. In terms of AO simulation, there are two different approaches. The analytic approach which models the entire system at once and the end-to-end simulation tools, reproducing each component of the system individually and linking them together. The advantage of analytic tools is to be less consuming in terms of computation time allowing the exploration of a wider range of different systems to find the optimum configuration.

For the study of an AO system on SALT focusing on the overall dimensioning, the analytic approach is the most appropriate. I used the software package PAOLA (Performance of Adaptive Optics for Large (or Little) Apertures, Jolissaint (2014)), which I presented briefly in the first part of this chapter. To carry out an AO simulation there are two main parts that need to be modeled aside from the AO system parameters: the telescope and the atmosphere. In order to obtain realistic results, I used the known telescope aberrations to create a model of the primary mirror as close as possible to the actual one. As for the atmosphere model I used the results from the site characterization study presented in Ch. 2. I describe the comparison checks that was conducted on the telescope model and give an overview of the full system, telescope and atmosphere, in the second part of this chapter. In the third part of this chapter, I determine the AO system optimal configuration taking into account both the general performances and the sky coverage. Based on the telescope and atmosphere models together with the optimized AO parameters, I looked at the performances that one could expect with such a system. The performance study is presented in the fourth part of this chapter.

4.1 Simulation Tool - the software package PAOLA

Fig. 4.3 gives the general layout of PAOLA. It calculates the analytical residual phase spatial power spectrum (PSD), based on Kolmogorov statistics, for each element in the system. From the

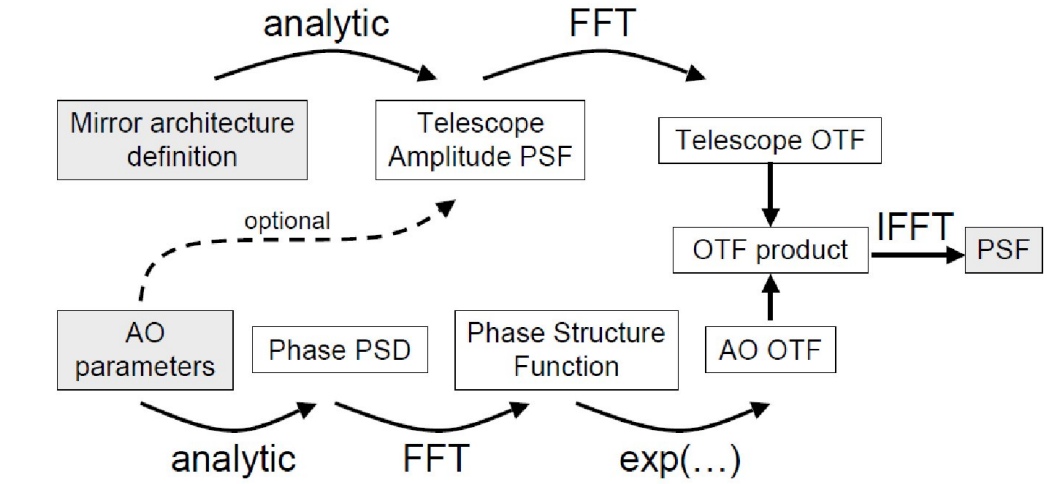

Figure 4.3: *PAOLA toolbox flow chart. Jolissaint (2014).*

PSD one can calculate the optical transfer function (OTF) for long-exposures, which PAOLA uses to calculate the point-spread function (PSF) through an inverse fast Fourier transform (IFFT). The system is split into the telescope and the AO system. The primary mirror architecture and known optical aberrations of the telescopes are used as input to calculate the PSF_{Tel} and then the OTF_{Tel}. Concerning the AO part, the OTF_{AO} is calculated analytically from the corrected phase structure function (D_{φ}) depending on both AO and atmospheric parameters used as input. Then the final OTF is given by:

$$OTF_{out} = OTF_{Tel}.OTF_{AO},$$

and finally, the IFFT gives the final PSF. For further details, an extensive description of the PAOLA software and theoretical background can be found in Jolissaint (2010, 2014).

Table 4.1: *SALT Telescope Model.*

Telescope parameters		
Diameter	11.1m	
central obscuration	Tracker and arms	
shape	segmented hexagonal	
Number of segments	91 (11 along the diagonal)	
gap between segments	0.01 m	
tracker position	centered (Fig. 4.4)	
telescope aberrations	Tip-Tilt	0.1”
in terms of Zernike modes (Z)	Decentering	10 microns
	Primary Astigmatism (Z=4,5)	27 nm
	Primary Coma (Z=6,7)	27 nm
	Primary Trefoil (Z=9,10)	25 nm
	Secondary Astigmatism (Z=11,12)	20 nm
	Secondary Coma (Z=13,14)	20 nm
	Secondary Trefoil (Z=16,17)	15 nm

4.2 Primary mirror and atmosphere model definition

Before studying the performances of a specific system one needs to define it with a realistic model. Here I present the telescope and atmosphere model, based on actual metrology on SALT and the site characterization campaign results presented in Ch. 2.

4.2.1 Telescope Parameters

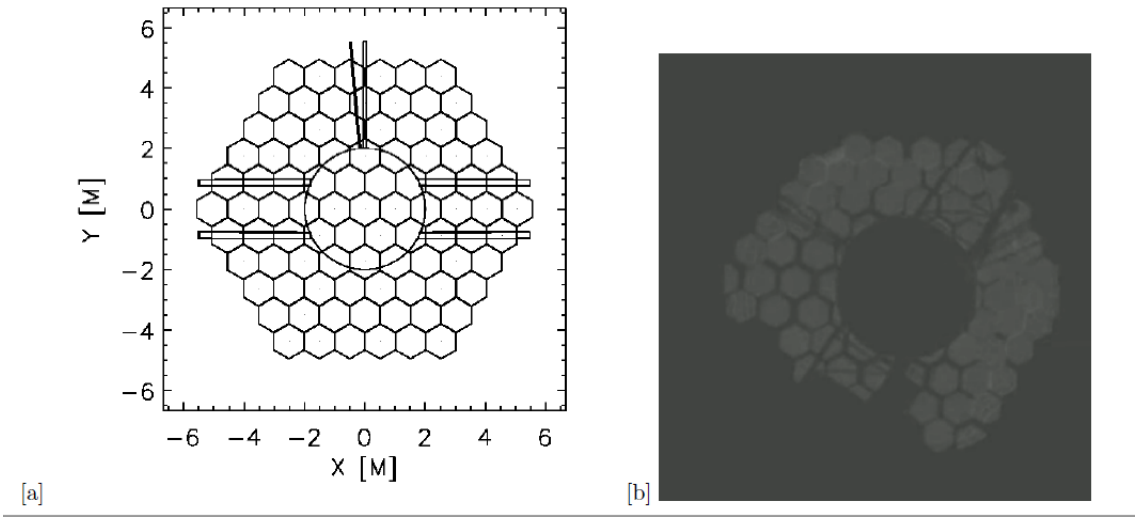

Figure 4.4: *SALT primary mirror and tracker shadow. (a): PAOLA simulation. (b):Actual image of SALT pupil and tracker shadow. Note that I used a simplified structure in my simulations, depicting the ideal case of a centrally located tracker on a simple two rails support.*

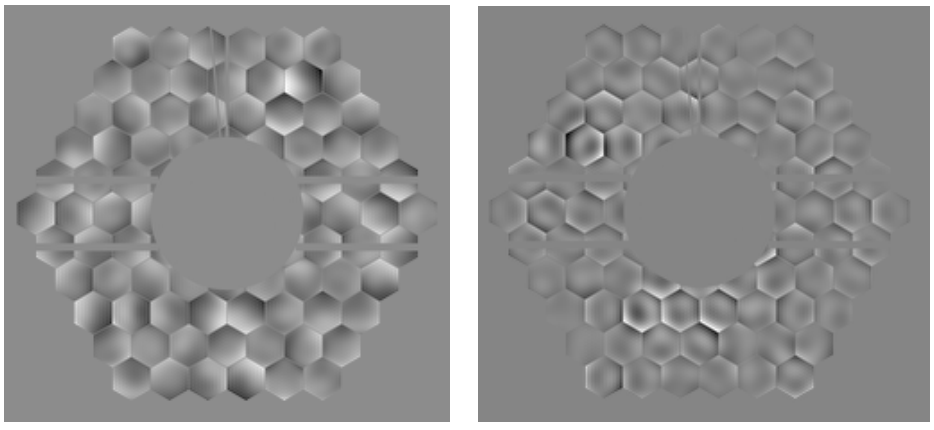

(a) (b)

Figure 4.5: *SALT pupil phase map at 700 nm. (a):phase map with telescope aberrations. (b):resulting phase map after the partial correction of the static aberration that the AO model system can deliver.*

I first define the overall shape of the primary mirror which consists of 91 one-meter hexagonal segments. All together, they form a spherical mirror of 11 meters edge-to-edge with a radius of curvature of 26.165 m. Since the instruments are at the prime focus, there is a central obscuration due to the tracker supporting the SAC and instruments payload, and itself supported by a rail structure. These features are modeled within the mirror parameter file in PAOLA. In order to represent the tracker, rails and payload, I used the spider arms definition option in PAOLA. In addition, to generate a model as close as possible to the real system, I added a number of known

aberrations to it. The aberrations, corresponding to the first 17 Zernike modes, were obtained via internal communication from Darragh O'Donoghue and based on the work done during the optomechanical modifications of the SAC (O'Donoghue et al., 2010). A summary of the SALT model is given in Table 4.1, where the individual values for each aberration are also provided.

Fig.4.4 shows the simulated primary mirror and tracker structure model as compared to an image of the actual SALT pupil. Since the AO system "sees" the telescope pupil, it is able to partially correct for the static aberrations in addition to the ones due to the atmospheric distortion. In order to see how much of the static aberrations are actually corrected by the simulated system, I looked at the system in a configuration with the telescope alone and no atmosphere. In Fig. 4.5 (a), one can see the phase map across the simulated pupil including the additional aberrations. Fig. 4.5 (b) shows the same phase map after correction by the AO system. One can see that not all the static aberrations of the telescope are corrected as there are some remaining residual phase aberrations across the pupil.

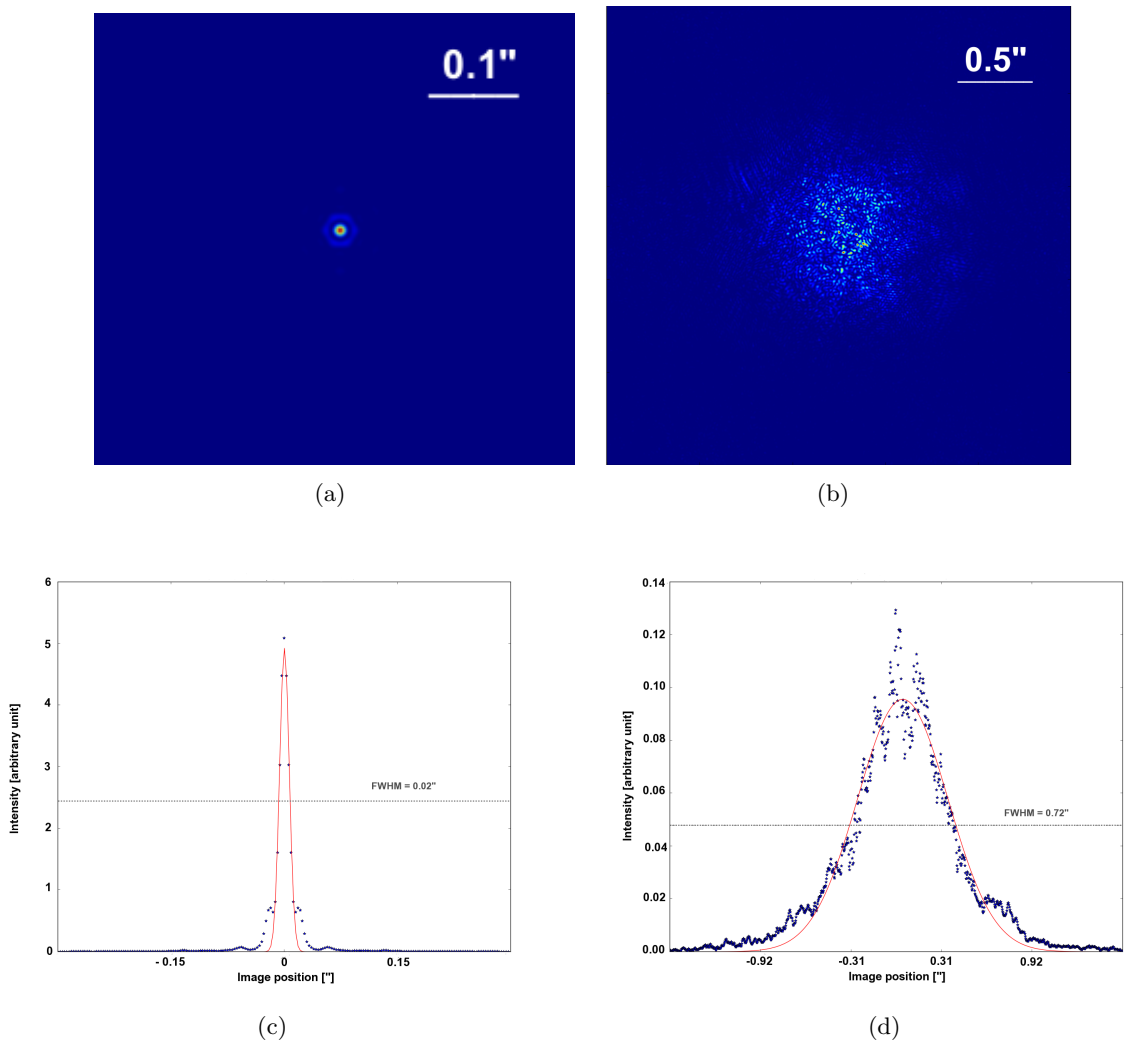

Figure 4.6: *Simulated system PSFs at 700 nm. (a) PSF delivered by a perfect system made of a model of SALT segmented mirror with no aberrations and a phased primary mirror array, the measured FWHM is 0.02". (b) PSF delivered by the SALT model including known static aberrations, the measured FWHM is 0.72".*

In order to test the simulated telescope, I ran two simulations. One with a perfect pupil with no aberration and one with the model defined above that will be used in the AO performance study

later on. I first looked at the PSF delivered by those two systems at 700 nm, and compared them with the theoretical diffraction limit of the telescope (0.013") and the SALT image quality (IQ) as given by design (0.68")[1]. I found respectively 0.02" for the perfect system and 0.72" for the full model including aberrations. The two are in fairly good agreement with the real system values. In Fig. 4.6, the top images show respectively, from left to right, the PSF from the simulation of a perfect system and the one from the model including aberrations. The bottom graphs show the radial profile of the top images (blue dots) and its fitted Gaussian functions (red lines) from which I deduced the FWHM values of 0.02" and 0.72" given above.

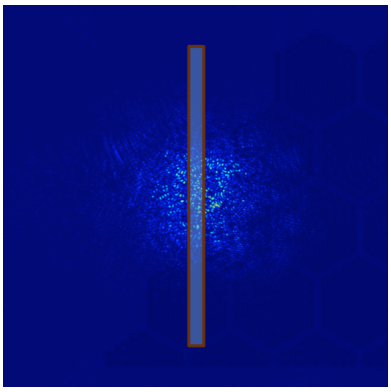

Figure 4.7: *Illustration of ESE estimation from simulations. The simulations, based on the telescope and atmosphere model, provide the expected PSF of a point source object. Here I show one of those simulated PSFs superimposed with a grey shaded area representing a slit. The ESE is given by the amount of energy within a given slit size.*

Table 4.2: *Comparison checks of PSF simulation vs. SALT actual data.*

DIMM seeing	**Seeing 37^o**		**FWHM**			
z=0, λ=500 nm	500 nm	700 nm	SALTICAM:	500 nm	700 nm	Simu(700 nm)
1.0"	1.14"	1.07"		1.4"	1.31"	1.3"
1.5"	1.72"	1.61"		1.8"	1.68"	1.73"

Since SALT is primarily designed for spectroscopy, I also compared the seeing limited spectroscopic performances of the model against actual on-sky performances of SALT. This comparison is summarized in Table 4.2 and 4.3. Note that in Table 4.2 the actual SALT values were measured at a wavelength of 500 nm, while due to computation memory limitation, I could only generate the equivalent results from the simulated model at 700 nm. For easier comparison, I give the equivalent SALTICAM values at 700 nm. The conversion from 500 nm to 700 nm is done by using the theoretical relation $\epsilon_0(700nm) = \left[\frac{700}{500}\right]^{-1/5} \epsilon_0(500nm)$. The first column gives the seeing as measured by the DIMM instrument, in the second and third column I give the equivalent seeing at the SALT elevation angle at both 500 nm and 700 nm. Column 4 and 5 provide a comparison between the observed FWHM on SALTICAM under those conditions of seeing and what was obtained with the simulated model. Similarly to the previous comparison in terms of IQ, the simulated model gives consistent results with what is observed with SALTICAM. In Table 4.3, more relevant to this study, I compared the spectroscopic performances in seeing limited mode between the real system and results from the simulations. The two first columns give the seeing conditions, as measured by DIMM, and the slit sizes considered. In the last two columns, I give the enslited energy (ESE) as

[1]Note here that the 0.013" value assumes a circular 11 m diameter telescope and ignores SALT mirror segmentation. Also the 0.68" is the error budget given by design specification with central wavelength ~635 nm.

measured by the real system (column SALT) and as computed by the simulations (column Simu). As illustrated in Fig. 4.7, I ran the simulations to obtain a PSF and then looked at the energy within a given slit size. Under 1" seeing, for slit sizes that deliver 50% and 80% of ESE on SALT, I obtained 56% and 80.2% of ESE in the simulations. Similarly, the simulations gave 53% and 79.6%, under 1.5" seeing. In both conditions of seeing, the simulations gave results very close to the 50% and 80% of ESE delivered by the real system.

Table 4.3: *Comparison checks of simulation for enslited energy output vs SALT actual data.*

DIMM seeing	**slit size**	**ESE**	
		SALT	Simu
1.0"	1.6"	50%	56%
	2.6"	80%	80.2%
1.5"	2.0"	50%	53%
	3.3"	80%	79.6%

Those simulations looking at the IQ results from the telescope alone and the spectroscopic performances under seeing limited mode allowed us to compare the telescope model with the real system. After demonstrating that they are in very close agreement, I am confident that the following performance study of an AO system on SALT will provide realistic values.

4.2.2 Atmospheric parameters

Table 4.4: *Sutherland atmospheric model.*

Atmospheric parameters				
seeing(500nm, za=0)	1.38"			
r_0 (500nm, za=0)	7.32 cm			
SALT zenith angle	37^o			
r_0 (500nm, za=37^o)	6.4 cm			
Outer-scale ($\mathcal{L}_0$)	20 m			
atmospheric turbulence profile	alt(m)	C_n^2(%)	wind dir(^{o})	wind speed(m/s)
	50	74.5	-135	8
	350	8.8	-135	8
	1000	3.6	-135	12
	2650	8.5	45	15
	8000	1.3	40	12
	12000	3.3	10	20

The second important part to define before starting to look at the potential performances of an AO system is the model of the turbulent atmosphere. For the present study, I will use the results from the extensive site characterization campaign presented in Ch. 2. For the wind profile, I used averaged wind speed and dominant wind directions obtained from both the SALT weather mast data and NCEP/NCAR [2] reanalysis data for the Sutherland site. The turbulence profile model is based on the results from the MASS six layers model. For the first part of the performance study, I used the median profile, which characteristics are summarized in Table 4.4. In a second part,

[2]NCEP/NCAR website: http://www.esrl.noaa.gov/psd/data/reanalysis/

I will be looking at the performances off-axis and investigate the influence of different profiles. In addition to the median profile, I use the profiles corresponding to the first and last quartile of the seeing distribution with seeing values of 1.15" and 1.55" respectively. Those three profiles are shown in Fig. 4.8 together with a summary table of the layers contribution.

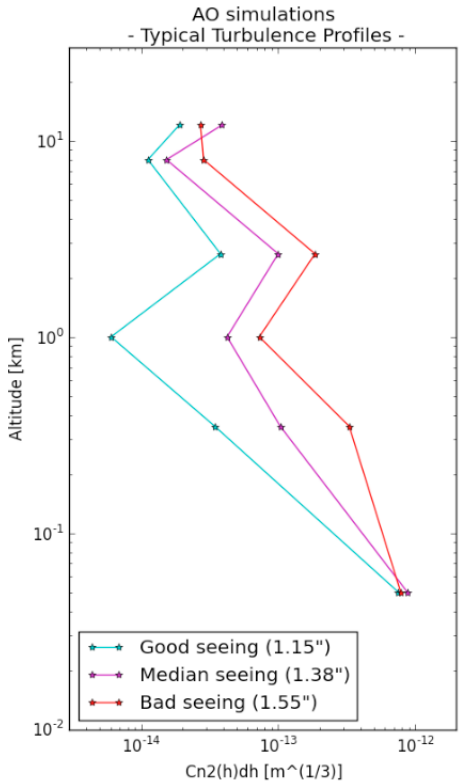

Turbulence Proliles for AO simulations

Altitude $[km]$	Good [%]	Median [%]	Bad [%]
12	2.2	3.3	1.9
8	1.3	1.3	2.0
2.65	4.4	8.5	13
1	0.7	3.6	5.1
0.35	4.0	8.8	23.1
0.05	87.4	74.5	54.9
ϵ_0	1.15"	1.38"	1.55"
r_0	8.8 cm	7.3 cm	6.5 cm

Figure 4.8: *Typical turbulence profile at the Sutherland site used as input for the AO simulations. Left: profiles representation. Right: table summary of the layers contribution. The purple profile is the median profile used for most of the simulations in Section 4.4. The blue and red profiles are used in the second Section of 4.4.3.*

4.3 AO system parameters optimization

In the previous section, I have defined all the parameters external to the AO system that, nonetheless, have a crucial importance in the determination of the potential AO performances on a specific telescope at a particular site. Using the telescope and atmosphere model described in the previous section one can now look into optimizing the AO parameters in the particular case of SALT at the Sutherland site.

As discussed in Section 1.4, an AO system can not do a perfect correction. There are a number of residual errors inherent to the system itself. The process of optimization consists in trading off between the different errors to find the point where the system performs best. From the full set of errors discussed in Section 1.5, we can extract four main ones: the WFS noise, the aliasing error, the fitting error, and the servo-lag error. Those errors are linked to one or more of the main AO system components, namely the WFS, the DM and the control loop (CL).

In the case of the simulations, the DM is in a Fried geometry (Fried, 1977) with respect to the WFS sub-apertures, hence the number of actuators is set by the number of sub-apertures in the WFS. I will subsequently only refer to the WFS number of sub-apertures when referring to the size of the system. The choice of WFS will determine the aliasing error and the WFS noise as well as have an influence on the servo-lag error through the integration time. It also determines the DM

number of actuators due to the chosen geometry and hence also defines the fitting error.

The CL typically influences the servo-lag error by providing more or less computation power and optimizing the WF reconstruction and DM command algorithm. In the simulations, I have set the WFS readout noise (RON) to $5e^-$/pix and let the loop gain and integration time to be optimized automatically. The loop gain (g) is a positive number acting as a multiplicative factor in several errors estimation formula (Jolissaint, 2010). To summarize its effect, both the aniso-servo and the aliasing errors decreases as g increases, while the WFS noise error increases with g. The optimization range of the loop gain is between 0.1 and 1.5, and the integration time between 0.1 and 15 ms.

In order to choose the size of the AO system, I looked at the residual wavefront error after correction for 12 different systems and a range of natural guide stars (NGS) magnitudes.

4.3.1 Wavefront error minimization

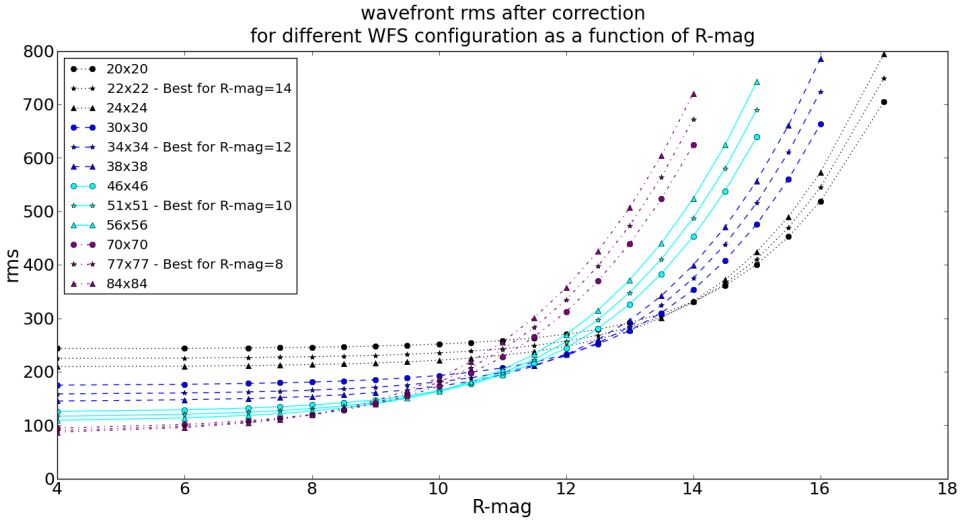

Figure 4.9: *Optimization of the number of sub-apertures. RMS as a function of NGS magnitude for different WFS configurations. Note that for each NGS magnitude (x-axis) there is an optimal system, providing the lower rms (y-axis), which is not necessarily the larger one. The fainter the NGS, the less efficient large system are as compared to smaller ones. The second column of Table 4.5 gives for each system configuration, the NGS magnitude at which it provides the optimal correction.*

The optimization results are presented in Fig. 4.9. For stars brighter than magnitude 8, we can see that increasing the number of sub-apertures gives a lower wavefront residual RMS. For fainter stars, the quality of the correction drops quickly, as can be seen with the exponential increase of the residual wavefront RMS. For each NGS magnitude, there is an optimal number of sub-apertures associated with the best correction. Increasing that number will lower the number of photons per sub-apertures resulting in an increase in the WFS noise. This can only be compensated by increasing the integration time, which in turn will increase the servo-lag error. On the other hand, using a smaller number of sub-apertures will reduce the sampling of the wavefront and increase the fitting error. The optimum size corresponds to the configuration for which the error budget is balanced. The error contribution for mag_{NGS}=8, 10, 12, and 14 optimum configurations are given in Table 4.5. In each case, one can see that all of the errors are of the same order.

To better visualize the optimization point for a specific NGS magnitude, I show the case of R = 12 in Fig. 4.10 where one can clearly see the inflection point. It is also worth noticing that this is also the point where the system provides the largest number of photons per sub-apertures as displayed on the x-axis on top of the figure.

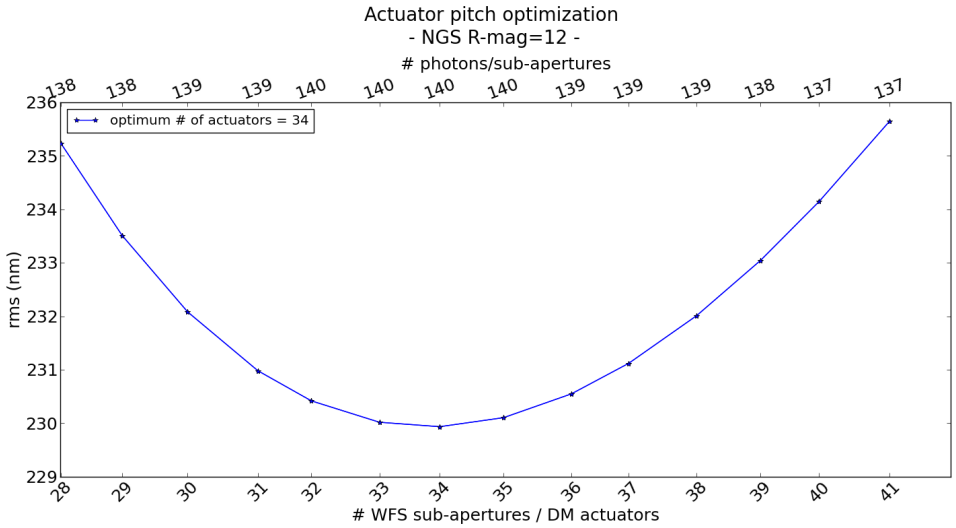

Figure 4.10: *Detailed system dimension optimization using a 12 magnitude NGS. Note that the optimal number of sub-aperture (bottom x-axis) corresponding to the lower rms (y-axis) value is also the configuration where the system delivers the higher number of photons per sub-apertures (top x-axis).*

Table 4.5: *Configuration optimization parameters.*

# of sub-apertures	**R-mag optimum** †	**Errors for the optimum *R*-mag [nm]**				**Mag-lim**♮ **(*J*)**	**star density**‡	**Strehl**∗ **(*J*)**
		fitting	aniso-servo	aliasing	WFS noise			
77x77	8	68	69	39	57	12.25	76	0.82
51x51	10	96	88	54	80	13	140	0.71
34x34	12	134	122	74	118	14	285	0.52
22x22	14	193	173	106	172	14.5	511	0.28

†*gives the magnitude for which the system configuration is optimal (at that magnitude this is the configuration that gives the best RMS).*
♮*magnitude at which the system reaches a Strehl ratio of 5%.*
‡*number of field stars per square degree having a magnitude greater than Mag-lim. These values are based on an average through all galactic latitude given in Table 1 of Simons (1995), who used the Bahcall-Soneira model (Bahcall & Soneira, 1981) and assumed a Johnson **R** bandpass for computing the predicted values.*
∗*value of the best Strehl ratio achieved in **J**.*

In addition Table 4.5 also displays the limiting magnitude of each system. Here the limiting magnitude is defined as the larger NGS magnitude that can be used while still providing a Strehl ratio greater than 5% in J-band. Also, the last column provides the value of the best Strehl that can be achieved with the system, providing that one uses a sufficiently bright NGS.

As explained above, there is no absolute optimum but one optimal system for each NGS magnitude. Hence, an NGS magnitude range for the system needs to be chosen to determine the final configuration size. The trade-off here is a better correction or a better sky-coverage. In Table 4.5, I give a rough approximation of the sky coverage at each limiting magnitude in terms of field star density, based on the Bahcall-Soneira model (Bahcall & Soneira, 1981).

Based on those results, I chose to optimize the system for an NGS of magnitude 12. For a first optimization, taking the performance in terms of Strehl in *J* for the 22x22, 34x34 and 77x77 configurations, gives respectively a best Strehl ratio of 0.28, 0.52 and 0.71. For each of these systems, the limiting magnitude at 5% of Strehl are 13, 14, and 14.5 respectively. Based on Table 4.5, the 34x34 increases by 104% the average number of stars available within one square degree

compared to the 51x51 for a loss of 27% in Strehl, while the 22x22 only increases the average number of stars by 44% for a 46% loss in Strehl compared to the 34x34. With regard to this simplistic evaluation of the number of stars per square degree compared to performances, I can justify the choice of a 34x34 configuration.

A more accurate determination of the sky coverage requires to also take into account the isoplanatic patch and the direction in the sky, towards the galactic plane or away from it as the field star density changes drastically. In the next part, I present a detailed evaluation of the sky coverage at the Sutherland site and for the specific range of right ascension (RA) and declination (Dec) covered by SALT.

4.3.2 Sky coverage

In order to accurately determine the number of field stars available to be used as NGS for the AO system I used the full guide stars catalogue from HST, GSC II (Lasker et al., 2008). I limited the search to the visibility range of SALT that spans from -76^o to +11^o in declination over all RA. As the number of stars in the catalogue between 10 and 14 magnitude is very large I also limited the search for stars with magnitude between 10 and 12. The results obtained are hence underestimating the number of available stars that can be used as NGS for the AO system. However, based on the Bahcall and Soneira model, one can estimate that the number of stars having magnitudes between 10 and 14 is 6.5 times larger than those between 10 and 12.

The full sky coverage map for SALT is shown in Fig. 4.11. Each green dot corresponds to the position of a star-like object [3] and is represented as a circle of 4' radius. The 4' radius serves as a representation of the area covered by the NGS to provide some correction to a science target located within that region. I will elaborate on the quality of the correction at different separation angle from the NGS in section 1.4.1. From this full map, we clearly see that the density of stars toward the galactic plane is much higher. I split the dataset to look at the sky coverage for regions within 10 degrees around the galactic plane, 25 to 35 degrees away from the galactic plane and 80 to 90 degrees away from the galactic plane. Examples of 1x1 degree fields within those three regions are shown in Fig. 4.12. Each circle has a 4' radius and is centered on the coordinate of a star. In Table 4.6 (column 2 to 4) I give the average percentage of sky-coverage for each region, around the galactic plane, around 30^o away from the galactic plane and around 90^o from the galactic plane. Those percentages are given for separation angle of 1, 2 and 4 arcminutes between the NGS and science target. The sky coverage ranges from 13% to 60% for the 4 arcminutes separation angle and 0.81% to 3.75% for 1 arcminute. This is in agreements with what I found using the Bahcall and Soneira model (given in column 5).

Table 4.6: *Sky Coverage.*

Distance from the galactic plane	**Sky coverage for different separation angle from the NGS**			**B&S‡ model**
	4'	2'	1'	1'
G. center	60%	15%	3.75%	3.6%
30^o	25%	6.25%	1.56%	1.9%
90^o	13%	3.25%	0.81%	0.9%

‡ *Sky coverage for a 1' separation angle calculated from the number of stars having magnitudes between 10 and 12 within 1 square degree as given by Bahcall & Soneira (1981)*

[3] GSCII website: *"Star/nonstar classifications were assigned by voting all available classifications from 15um scans, before applying the magnitude cutoff. Classifications from 25um scans were used only if no 15um data were available for the object. Ties were broken in favor of nonstar, and defect classifications were considered to be nonstellar for matched objects. Unmatched plate defects were excluded from the catalogue."*

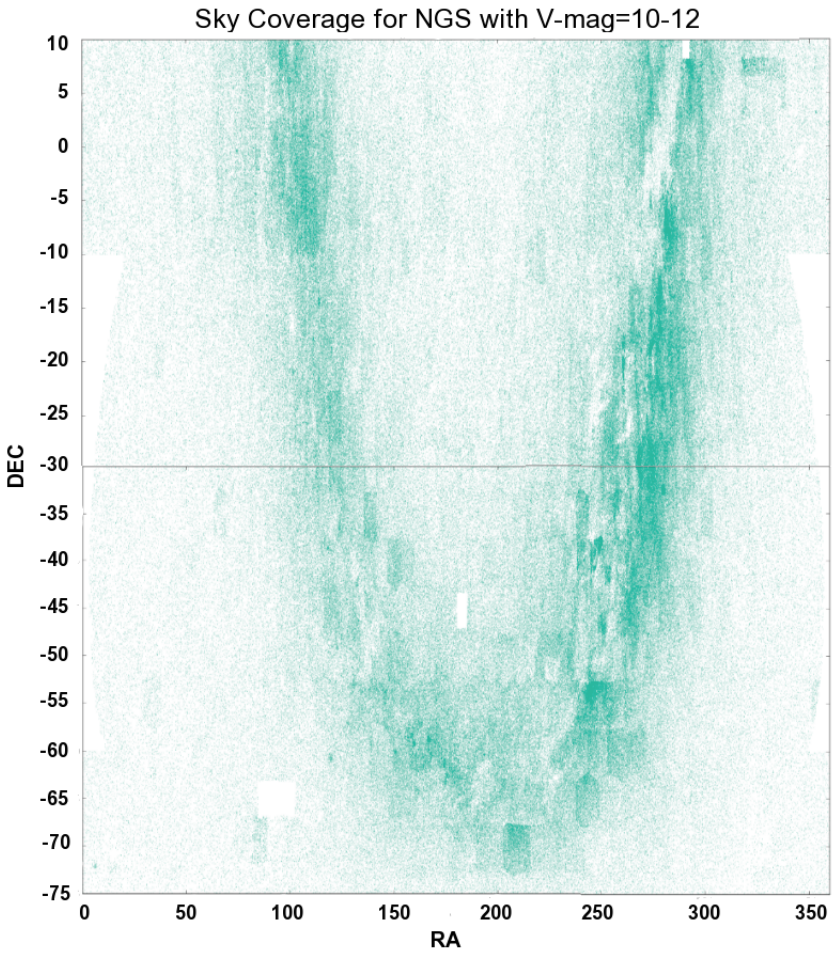

Figure 4.11: *Sky coverage plot. This plot was created by using the Guide Star Catalog II (GSC-II, Lasker et al. (2008)). I selected all star-like objects* [3] *with magnitudes within the 10 to 12* $R-mag$ *range. At each object location I then plotted a disc with a 4 arcminutes radius, shown in green. I limited the search to the range of RA and Dec covered by SALT.*

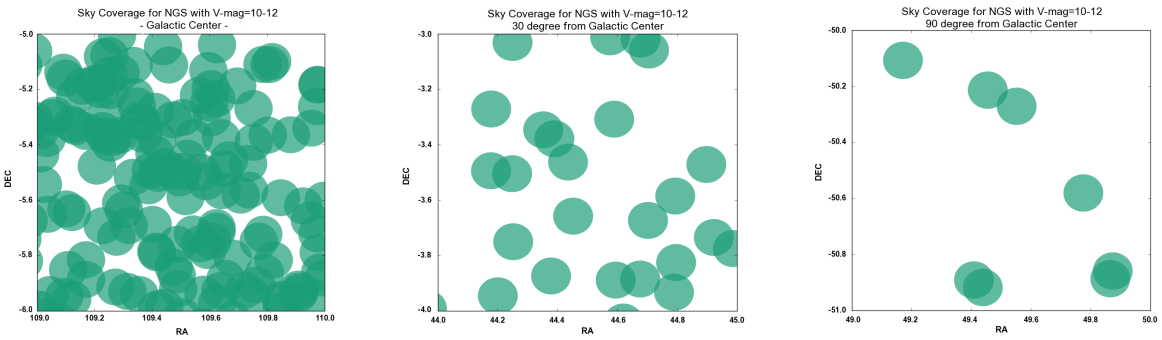

(a) (b) (c)

Figure 4.12: *The 3 figures shown here were produced with the same method as in Fig. 4.11. Only here, I zoomed in on 3 specific regions of the sky representative of the star density in the Galactic center direction for (a), at* 30^o *from the galactic center in (b) and* 90^o *in (c).*

If I extrapolate the equivalent sky coverage, for a 1' separation angle from the NGS, with magnitudes between 10 and 14, based on the Bahcall and Soneira model, I find the sky coverage towards the galactic plane to be 24%, while it is 10% and 5%, at 30^o and 90^o respectively. Close to 100% sky coverage is reached when considering a 2' separation angle from the NGS towards the galactic plane.

4.4 Expected AO performances on SALT

Table 4.7: *SALT AO modeling specifications.*

Atmospheric parameters				
seeing(500nm, za=0)	1.38"			
r0 (500nm, za=0)	7.32 cm			
SALT zenith angle	37^o			
r0 (500nm, za=37^o)	6.4 cm			
Outer-scale ($\mathcal{L}_0$)	20 m			
atmospheric turbulence profile	alt(m)	C_n^2(%)	wind dir(^{o})	wind speed(m/s)
	50	74.5	-135	8
	350	8.8	-135	8
	1000	3.6	-135	12
	2650	8.5	45	15
	8000	1.3	40	12
	12000	3.3	10	20
Telescope parameters				
Diameter	11.1 m			
central obscuration	Tracker and arms			
shape	segmented hexagonal			
Number of segments	91 (11 along the diagonal)			
gap between segments	0.01 m			
tracker position	centered (Fig. 4.4)			
telescope aberrations	Tip-Tilt		0.1"	
in terms of Zernike modes (Z)	Decentering		10 microns	
	Primary Astigmatism (Z=4,5)		27 nm	
	Primary Coma (Z=6,7)		27 nm	
	Primary Trefoil (Z=9,10)		25 nm	
	Secondary Astigmatism (Z=11,12)		20 nm	
	Secondary Coma (Z=13,14)		20 nm	
	Secondary Trefoil (Z=16,17)		15 nm	
AO parameters				
Guide star	spectral type/Temperature		R-mag	
	A0 - 7500 K		8-16	
isoplanatic angle	correction on-axis			
conjugation height	0 m			
WFS RON	5 e/pix			
loop mode	closed			
loop gain	optimized			
integration time	optimized			
♯ of WFS lenslet/DM actuators	34 - after optimization (see § 4.3)			
Centroid calculation	Center of Gravity (8x8 pix)			

As mentioned previously, SALT is primarily designed for spectroscopy. It is currently equipped with two spectrographs. The Robert Stobie spectrograph (RSS) and the high-resolution spectrograph (HRS). The existing RSS-VIS arm uses either a single slit or a multiple slits mask. On the other hand, the HRS is a fiber-fed instrument using different fibers and offering four modes with different resolution. In order to evaluate the improvement in performances that an AO system could deliver on SALT I looked at the enslited energy to cover the case of the RSS-VIS and the encircled energy in the case of the HRS. From the current configuration, I considered the RSS slit sizes of 0.6", 0.9", 1.2" and 2". The two HRS fibers are modeled by a 2.2" and a 1.6" fiber corresponding to the 2.23" and 1.56" of the real system. As for the upcoming RSS-NIR arm, the

proposed design is based on an integral field unit made out of either 0.6" or 0.9" fibers, hence for the case of RSS-NIR I will be looking at the encircled energy within those two fiber sizes.

The current instruments were designed to operate in seeing limited mode and hence are not suited to take direct advantage of an AO system without other design modifications. The comparative study here is, however, important in order to evaluate the potential improvements on similar instrumentation. In Table 4.7 I detail the overall parameters of the system model I used in the simulations, including the telescope and atmosphere definition as well as the chosen AO system configuration.

The performance study is separated into two main parts. I looked first at the performances on-axis at different wavelengths and for different NGS magnitudes. In the second part, I focused on the performances off-axis and consequences in terms of sky coverage. Lastly, I briefly discuss the issue of moving pupil due to the specific design of SALT.

4.4.1 General performances on-axis

Fig. 4.13 gives the expected spectroscopic performances for a 34x34 AO system in R-band at 0.7 microns (top graphs), J-band at 1.2 microns (middle graphs) and H-band at 1.6 microns (bottom graphs) in terms of enslited energy, referred to as ESE later on (left graphs) and encircled energy, referred to as EE later on (right graphs). Each graph shows the performances with NGS magnitude of 8 (dark blue line), 10 (green line), 12 (red line), 14 (light blue line) and 16 (purple line) as well as the seeing limited case (black dotted line). The x-axis gives both the slit size (bottom) and its corresponding fraction of $\frac{\lambda}{D}$ value (top), with $\frac{\lambda}{D}$ being the diffraction limited case. The y-axis gives the percentage of ESE or EE values. For this part of the study, I used median seeing and turbulence profile summarized in Table 4.7.

On the overall performances, one can see that for NGS of magnitude 16, there is no or very little improvement as compared to the seeing limited mode. This is in agreement with the limiting magnitude of around 14 that was determined earlier on the basis of performances in terms of Strehl ratio and reported in Table 4.5. This is due to the lack of photons within the SHWFS lenslet leading to poor centroid measurements. One could improve the quality of centroid measurements by increasing the exposure time on the WFS camera, but that will be at the expense of smoothing out the turbulence and hence under correcting for it. At the other end of the magnitude range, the system reaches nearly full performance for stars of 10 mag and one can see that having an NGS of 8 mag does not bring much improvement over the tenth magnitude star. The system, being optimized for a twelfth magnitude NGS, can use brighter stars but it does not improve significantly the quality of the correction. By using brighter stars, one could decrease the exposure time on the WFS camera, however as soon as the overall time necessary to close the AO loop gets lower than the turbulence coherence time (τ_0), the turbulence is considered "frozen". Going to shorter exposure time, and speeding up the overall AO loop, while it is already below τ_0, would not improve the quality of the AO correction.

With regard to the wavelength range covered, one can clearly see that better correction is obtained at longer wavelengths. This is due to the fact that shorter wavelengths are more sensitive to shorter spatial frequency turbulence that are not sensed by the modeled system. Only turbulence with spatial frequencies larger than the size of the WFS sub-apertures is measured. With a fixed system of 34x34 sub-apertures across the 11 m pupil of SALT, we are unable to measure turbulence with spatial scale smaller than 30 cm. This lower limit on the wavefront spatial sampling is the reason for the higher measurement error at shorter wavelengths. Increasing the wavefront spatial sampling to improve performances at shorter wavelengths will be at the cost of a poorer sky coverage, as one will need to use brighter NGS to compensate for the loss of photons in smaller sub-apertures.

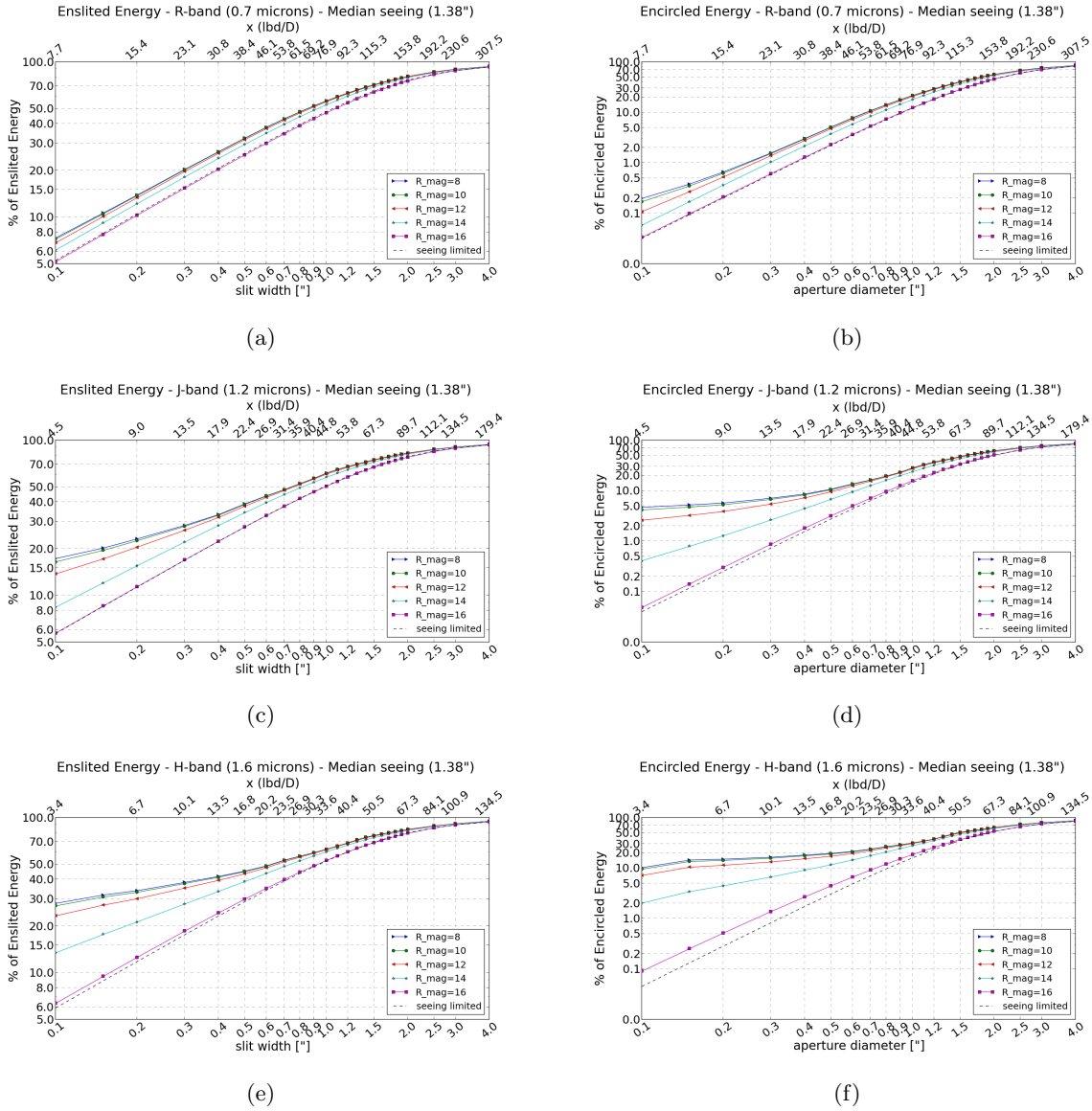

Figure 4.13: *Performance results from AO simulations. Enslited (left) and encircled (right) energy as a function of slit size, in R, J and H-bands from top to bottom. Each color curve corresponds to a different NGS R-band magnitude, including 8, 10, 12, 14 and 16. The dash line shows the seeing limited mode performances for comparison. The fraction of the diffraction limit size to which the slit corresponds is also given on the top x-axis.*

In terms of aperture size range at the entrance of the spectrograph, we always see a better improvement for smaller apertures over the larger ones. This is due to the simple fact that larger apertures, even with no correction, already enclose a large portion of the light. Hence to best capitalize on an AO system capabilities one should look towards the smaller aperture sizes that would not be available otherwise. However, any AO system will still bring some improvement to existing systems designed to work on seeing limited mode.

Looking into more details, I focused on the AO performances for slit and fiber sizes similar to those of the current instrumentation on SALT in order to investigate the possible improvement over the existing system.

4.4.2 Potential improvement on existing systems

Table 4.8 summarizes the simulated performances of the AO system for existing and planned instrument slit and fiber sizes.

The first 3 columns of Table 4.8 give a performance comparison between seeing limited mode and AO mode for slits similar to the ones on the RSS visible arm (RSS-VIS, 320-900 nm). Here we are looking at the ESE results (Fig. 4.13, left) for AO correction with an NGS of magnitude 12 (red line) for the R-band in the visible part of the spectrum. The ESE, in seeing limited, are respectively 30.4%, 43.8%, 55.3% and 76.4% for slit sizes of 0.6", 0.9", 1.2" and 2". Those values go up to 37.1%, 51.3%,62.4% and 80.3% with the AO correction on. This corresponds to +22%, +17.1%, +12.8% and +5.1% gain in ESE for each slit sizes respectively.

In order to evaluate the potential gain in performances for the upcoming near-infrared arm of the RSS (900 to 1700 nm) I looked at the J (1200 nm) and H (1600 nm) bands. Since the design plans for the RSS-NIR is to have it fed by a fiber bundle with fibers of either 0.6" or 0.9" (Doering, Sheinis & Wolf, 2010; Wolf et al., 2014), I looked at the EE results (Fig. 4.13, right). Those results are reported in column 4 to 9 of Table 4.8. For these two fiber sizes, the EE in seeing limited mode are 9.5% and 19.8% in J-band and 10.3% and 21.2% in H-band. With AO correction the EE rises up to 21% and 32.8% in J-band and 29.2% and 38.3% in H-band. This is equivalent to a 120.1% and 182.8% increase in EE for the 0.6" fiber in J and H-band respectively, and 65.7% and 80.6% for the 0.9" fiber.

Concerning the evaluation of potential gain for the HRS instrument, I looked at the EE for fiber sizes of 1.6" and 2.2" similar to the current HRS fiber sizes of 1.56" and 2.23". The results are reported in the last 3 columns of Table 4.8. The encircled energy gain with AO correction as compared to the seeing limited performance for the 1.6" fiber is 25% and for the 2.2" fiber the gain is 14.1%.

These gains in EE and/or ESE can be related to more commonly used parameters in terms of defining a spectrograph capabilities. One could consider several factors to evaluate the overall instrument capabilities, among which:

- The resolving power.
  Increasing the resolving power increases the quality of the data and opens up a window on new science cases that could not be studied otherwise.

- The integration time.
  Reducing the integration time for a given science output increases the number of observations that can be made over an observing night and hence the science output of the instrument.

Table 4.8: *Spectroscopy Performance on existing and upcoming instruments.*

Aperture		RSS-VIS (320-900) ESE @ 700 nm			RSS-NIR (890-1700) EE @ 1200 nm			EE @ 1600 nm			HRS (370-890) EE @ 700 nm		
fiber size	slit size	sltd [%]	AO [%]	Gain	sltd [%]	AO [%]	Gain	sltd [%]	AO [%]	Gain	sltd [%]	AO [%]	Gain
0.6”		30.4	37.1	+22%	9.5	21	+120.1%	10.3	29.2	+182.8%	-	-	-
0.9”		43.8	51.3	+17.1%	19.8	32.8	+65.7%	21.2	38.3	+80.6%	-	-	-
-	1.2”	55.3	62.4	+12.8%	-	-	-	-	-	-	-	-	-
-	2”	76.4	80.3	+5.1%	-	-	-	-	-	-	-	-	-
1.6”		-	-	-	-	-	-	-	-	-	42.7	53.4	+35%
2.2”		-	-	-	-	-	-	-	-	-	61.2	69.8	+14.1%

The slit size necessary to reach a given ESE is smaller with AO correction as compared to the seeing limited case. Assuming that the detector sampling and the overall spectrograph design offers the possibility of taking advantage of it, using a smaller slit will lead to a higher resolving power. The resolving power of a spectrograph is given by $R = \frac{\lambda}{\Delta\lambda}$, with λ the observing wavelength and $\Delta\lambda$ the projected slit width on the camera. Equivalently, the AO correction delivers a higher ESE value for a given aperture size. This reduces the integration time necessary to reach the same signal to noise ratio (SNR) as in seeing limited mode. For bright science targets, I assumed the SNR to be object dominated (photon noise regime). For this particular case, one can assess the potential decrease of integration time that AO correction will allow using an approximation of the SNR expression. Neglecting the sky background and detector noise, it can be written as: $SNR \propto (t \times ESE \times R_*)^{1/2}$, with t the integration time, and R_* the flux from the science object. If we look at the RSS-VIS case, we find that to reach 50% of ESE in seeing limited mode requires the use of a 1.1" slit. With AO correction on, using a R=12 NGS, one could narrow down the slit width to 0.85", while keeping the same percentage of ESE. Based on the definition of the resolving power given above, reducing the slit size by a factor 0.77 corresponds to 30% gain in resolving power. As for the integration time, I looked at the largest (2") and the smallest (0.6") slit sizes results. For the 2" slit the ESE is only 1.05 times larger, leading to 5% decrease of the integration time. For the 0.6", however, the ESE increases by a factor 1.22, hence the integration time could be decreased by 18%.

Similarly for RSS-NIR, if we look at the fiber size for seeing-limited and AO mode that provides 50% of EE, we see that an AO system could bring a 25% increase in resolving power in J-band and a 33% increase in H-band. As for the exposure time, the AO correction could decrease the required exposure time for the same signal to noise ratio by 40% for the 0.9" fiber and 55% for the 0.6" fiber in J-band, and 45% and 65% in H-band.

In the case of HRS, one could reduce the exposure time by 20% and 12% for the 1.6" and 2.2" fibers, respectively. As for the resolving power at 50% of energy, it could potentially be increased by 36% when using the 1.6" fiber and 30% for the 2.2" one. Alternatively, the AO correction would allow to reach the same value of encircled energy while using smaller fibers, of 1.3" and 1.85" respectively. This would result in 23% and 19% potential gain in spectral resolution.

This part of the study examines how instruments designed for seeing limited operation may benefit from an AO system. The goal here was to assess the potential impact in terms of performances that an AO system would have in comparison with the existing telescope and instruments suite performances. Spectrographs initially designed as AO-assisted instruments could take greater advantage of the AO correction. The domain for which AO correction will be the most beneficial is for high spectral resolution, using apertures smaller than 0.5" at longer wavelengths. However, I have shown that even for the existing and upcoming instrument performances, substantial improvements could be obtained thanks to AO correction. Those improvements could grant access to higher spectral resolution, help reduce the exposure time necessary to achieve a given SNR as well as increase the sensitivity of the instruments toward fainter objects.

For all the cases studied so far I only looked at the performances on-axis. In the following section, I present the results from the off-axis performance study.

4.4.3 Performances off-axis

In this section, I look at the off-axis performances of the chosen AO system configuration. The correction provided by a system using a single NGS is not uniform across the FOV. This is due to the difference in light path while looking at objects in different directions of the sky. Seen from the entrance aperture of the telescope, the light from objects at different observing angles passes through slightly different portions of the atmosphere and hence are not exposed to the same turbulence (Fig. 1.5). As a result, the size and shape of the AO-corrected PSF varies across the FOV (Orlov et al., 2003). Assuming the NGS is at the center of the FOV, the correction degrades

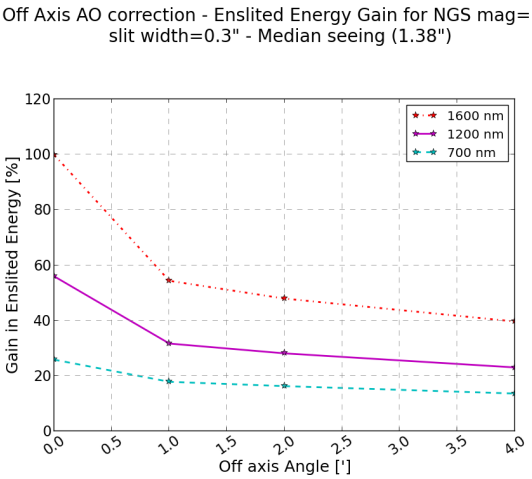

(a)

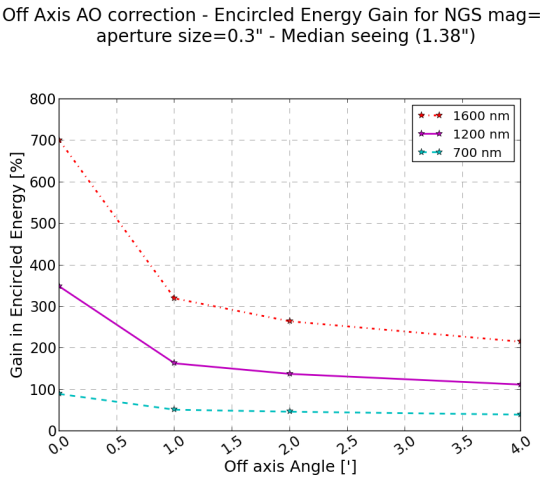

(b)

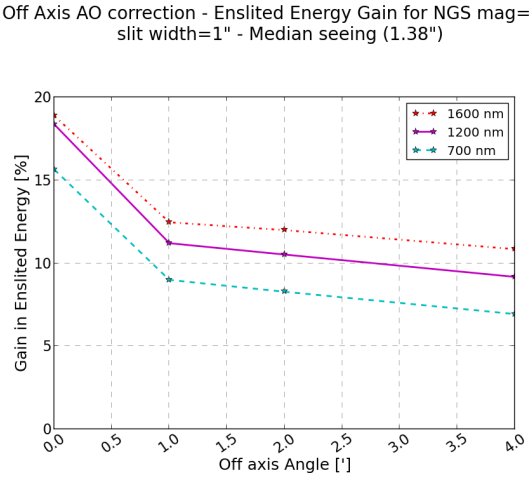

(c)

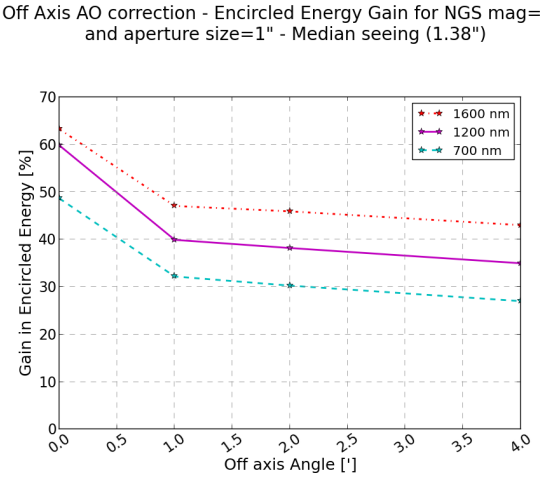

(d)

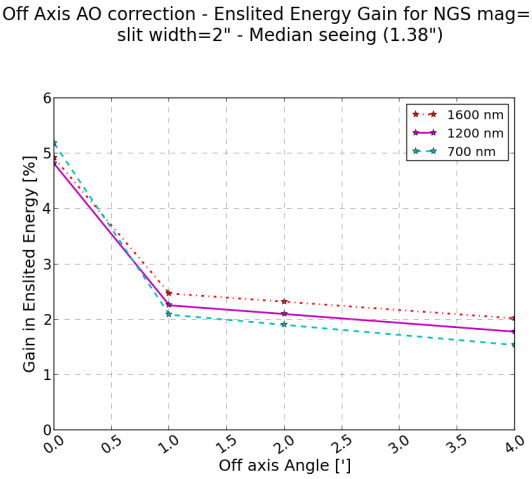

(e)

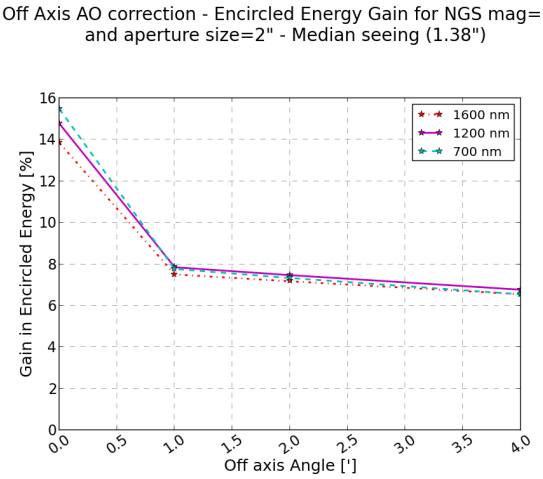

(f)

Figure 4.14: *Performance results from AO simulations. Enslited (left) and encircled (right) energy as a function of separation angle from the NGS and for slit/aperture sizes of 0.3", 1" and 2", from top to bottom respectively. The red curve corresponds to the H-band (1600 nm), purple the J-band (1200 nm) and blue the R-band (700 nm).*

further away from the NGS. Not only does the PSF becomes broader, but there is also an elongation of the PSF in the radial direction away from the NGS. Note that the anisotropic effect is also stronger at shorter wavelengths as well as under bad seeing conditions associated with stronger turbulence in the higher layers of the atmosphere.

In order to asses the off-axis performances of the AO system model that I chose I looked at two different things. I first looked at the performances under median seeing conditions in R, J and H-band for three different aperture sizes. I choose 1" and 2" apertures as an average and large value from the existing instrumentation. And for the third size I chose 0.3", half the size of the smaller currently used apertures. This provides us with a first idea of the potential gain that an AO-assisted designed instrument could obtain while using smaller apertures.

In the second part I looked at the effect of the turbulence profile on off-axis performances. As explained in Section 1.2.2.3, the turbulence profile has a direct influence on the size of the isoplanatic patch and hence the performances off-axis.

4.4.3.1 General off-axis performances under median seeing conditions

Fig. 4.14 shows the AO performances in median seeing conditions when using a single guide star located at 1, 2 and 4 arcminutes from the science target (this is given by the off-axis angle along the x-axis of the figures). The y-axis gives the gain (G) in enslited energy (left) or encircled energy (right), calculated with the following formula: $G = \frac{EE_{AO} - EE_{sltd}}{EE_{sltd}}$. Each figure gives the gain for a given aperture size: 0.3" for the top figures, 1" for the middle figures, and 2" for the bottom ones. For aperture sizes of 0.3" and 1", the best performances are always obtained at longer wavelengths where the correction is more efficient. However, for the 2" aperture, the performances are better at shorter wavelengths on-axis and for small off-axis angles. The seeing angle (ϵ_0) has a $\lambda^{-1/5}$ dependence on the wavelength and hence a seeing-limited image is larger at shorter wavelengths. For the range of wavelengths and the conditions of seeing considered, most of the light is already contained within a 2" aperture. Even with better performances of the AO system at longer wavelengths, there is too little room for improvement to obtain a significant gain as compared to shorter wavelengths. On the other hand, the isoplanatic angle (θ_0) has a $\lambda^{6/5}$ dependence on the wavelength hence, its size increases significantly with the wavelength. As a consequence, the anisotropic effect is more important at shorter wavelengths, and the gain from AO correction at shorter wavelengths drops faster with increasing off-axis angle. This results in an inversion of the gain performances at larger off-axis angle where a better gain is obtained at longer wavelengths.

Looking at the encircled energy for the 1" aperture (Fig. 4.14, middle right), the gain at 1 arcminute off-axis is ~1.5 times lower than that obtained on-axis. Similarly, for the 0.3" aperture the gain is divided by 2 when using an NGS located at 1 arcminute off-axis. However, searching for an NGS up to 1 arcminute away from the science object increases the sky coverage by a factor 100 as compared to on-axis correction. While the correction is not as good when using an NGS at 1 arcminute, it remains above 30% of gain in EE over the seeing limited case, within a 1" aperture. Further extending the NGS search field out to 2 arcminutes away from the science target increases the sky coverage by a factor 4 as compared to the 1 arcminute search. This would deliver close to full sky coverage towards the galactic center. For the 1" aperture the correction performance is only reduced by a factor ~1.05 as compared to the correction done with an NGS 1 arcminute away from the science target. Similarly, the correction gain drops by a factor 1.15 for the 0.3" slit. As for increasing the search for NGS up to 4 arcminutes away from the science target, it is clearly not advantageous for targets towards the galactic center, where the 2 arcminutes search already provides close to full sky coverage. For other targets, there is an additional loss in correction, decreased by a factor 1.1 as compared to the 2 arcminutes search when using a 1" aperture. However, it still provides reasonable improvement, with 27% or more gain over the seeing

limited case. For the 0.3" slit the gain remains above 47%.

We clearly see that, given the distribution of turbulence at the Sutherland site, mainly located in the ground layer, the AO system can provide decent correction even when using NGS far away from the science target. The system can hence be used at its full capabilities for science target bright enough to also serve as NGS, or if there is a bright enough NGS within arcseconds around it. The system could also provide reasonable correction and close to full coverage for the part of the sky towards the galactic center, using NGS up to 2 arcminutes away from the science object.

4.4.3.2 Influence of the turbulence profile on off-axis correction

Here instead of looking at the performances at different wavelengths under the general median seeing conditions, I looked at the performances at 700 nm, the most challenging wavelength of the set, under different seeing conditions and turbulence profiles. As presented in Section 1.2.2.3, the size of the isoplanatic patch is mainly influenced by the amount of turbulence in the higher atmospheric layers, while the lower layers do not affect it as much. In order to evaluate the impact of the Sutherland atmospheric turbulence conditions on the potential performances of an AO system, I used three typical profiles extracted from the site monitoring campaign. Those three profiles are shown in Fig. 4.8.

Fig. 4.15 shows the AO performances at 700 nm under good (blue curve), median (purple curve) and bad (red curve) seeing conditions when using a single guide star located at 1, 2 and 4 arcminutes from the science target. As for Fig. 4.14, the y-axis gives the gain (G) in enslited energy (left) or encircled energy (right) and each graph, from top to bottom, corresponds to apertures size of 0.3", 1" and 2".

Overall since the profiles associated with bad and median seeing condition also have stronger turbulence in the higher layers, the anisotropic effect is more important as the seeing degrades. As a result, the gain in encircled or enslited energy drops faster with increasing off-axis angles under worse seeing conditions. Within the two larger apertures of 1" and 2" the gain on-axis is more important under bad seeing conditions. The reason here is linked to the fact that under good seeing condition there is very limited room for improvement within larger apertures, and hence a lower gain. However, as one goes further off-axis, since the gain is dropping faster for bad and median seeing conditions, we see an inversion in performances towards a higher gain for the better seeing conditions. For the smaller aperture of 0.3", even on-axis the gain is better under good seeing conditions. The shape of the corrected PSF comprises a central diffraction limited core ($\frac{\lambda}{D}$) and a halo that extends to $\frac{\lambda}{r_0}$. While the two larger apertures include most of the light from both the core and the halo even for seeing limited images, the 0.3" aperture is cutting out most of the energy within the halo. Under good seeing conditions, the correction brings a larger amount of the energy in the core of the AO-corrected PSF, hence the higher gain for good seeing conditions. Note that for slits, as compared to circular apertures, the correction only applies along the slit width and hence gets lower improvement. This explains the fact that on-axis, even for the 0.3" slit, there is still a slightly better gain under bad seeing as compared to median seeing conditions. As more of the energy is left within the halo for off-axis correction, at a similar off-axis angle the decrease in correction efficiency affects smaller apertures more than larger ones that comprise more of the halo region of the PSF. In consequences, we see a faster drop in the gains for smaller aperture sizes which explains why the inversion of performances between good and bad seeing conditions happens at smaller off-axis angle for 1" aperture compared to the 2" aperture.

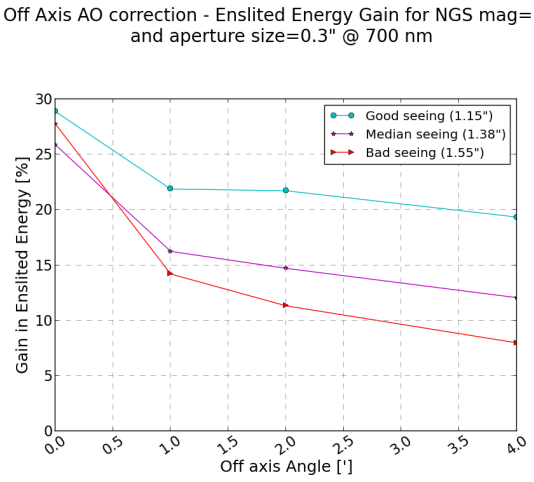

(a)

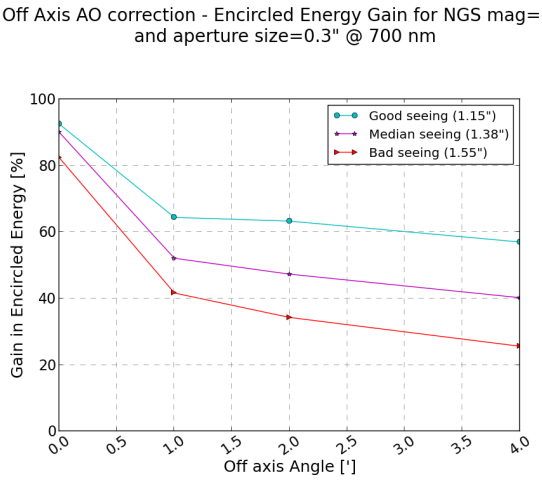

(b)

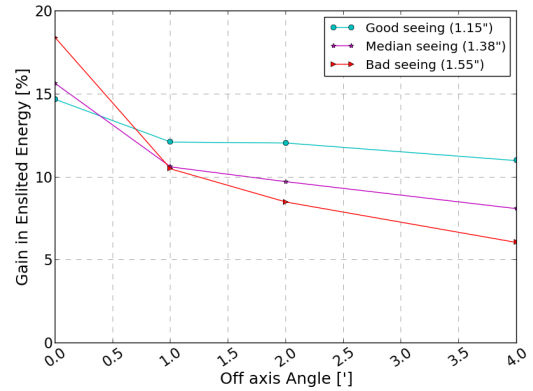

(c)

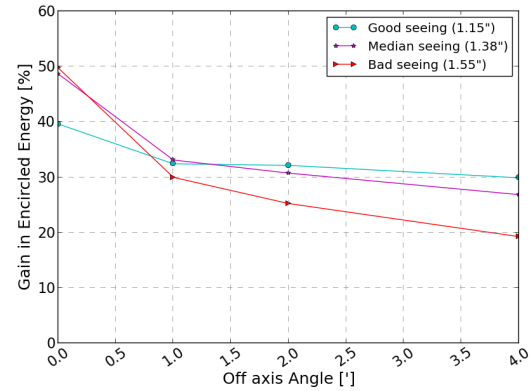

(d)

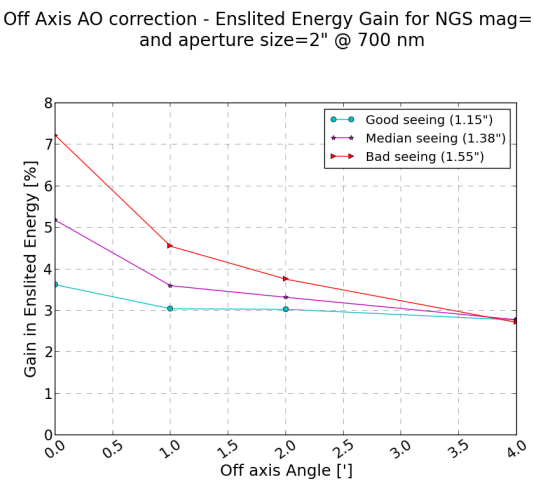

(e)

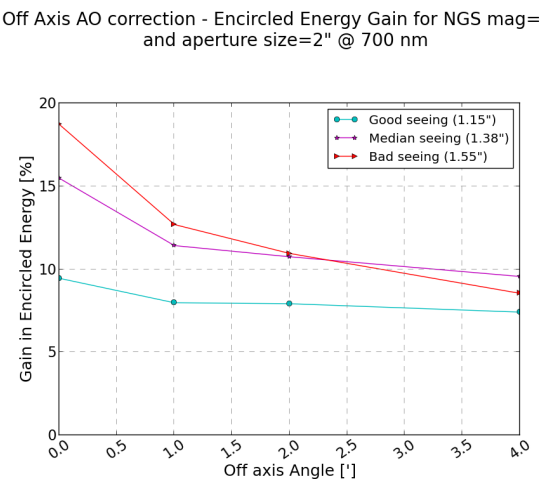

(f)

Figure 4.15: *Performance results from AO simulations. Enslited (left) and encircled (right) energy as a function of separation angle from the NGS and for slit/aperture sizes of 0.3", 1" and 2", from top to bottom respectively. Here all simulations are done in the R-band at 700 nm. The curve colors represent the different conditions of seeing and turbulence profiles given in Section 4.8. Good seeing conditions is the blue curve, median the purple and bad the red.*

Based on those results, one can see that despite a clear performance drop of the AO correction as the seeing conditions degrade while using off-axis NGS, the gain in encircled energy, especially for small apertures where AO is the most beneficial, remains significant. Even at the more challenging wavelength of 700 nm the AO system tested still provides over 25% gain in encircled energy for the 0.3" under bad seeing conditions. This means that 25% or more gain in encircled energy could potentially be reached 70% of the observing time.

4.4.4 Effect of SALT moving pupil

As mentioned in the introduction of the Chapter, the SALT design includes the absence of a secondary mirror, a fixed elevation and tracking done at prime focus by the tracker that also supports the instruments. As illustrated in Fig. 4.1 this causes variations in the pupil illumination. The effective area of the primary mirror being used during an observing track varies from 55 m^2, when the tracker is centrally located, down to 40 m^2 at the far end of the tracker position.

While the AO system performances should remain unchanged, the limiting magnitude decreases with the pupil size. That is considering the interaction matrix of the AO system can handle the loss of illumination on some parts of the WFS, corresponding to the shaded areas of the primary mirror, and its consequences for the DM control. At all times, the part of the pupil that is illuminated will benefit from AO correction with an unchanged wavefront spatial sampling. This means that for the illuminated area, each WFS sub-aperture will keep receiving the same amount of photon and hence the AO correction efficiency will not be affected by light losses due to the moving pupil. However, due to the reduced total effective collecting area (S), the science object flux (F_*) decreases . As a result, for a science object of a given V-mag, the SNR drops as the pupil illumination decreases.

4.5 Conclusions

In this chapter, I presented the modeling and dimensioning of a single natural guide star (NGS) adaptive optics (AO) system for the Southern African Large Telescope (SALT). I used known aberrations of the telescope as well as the results from the seeing and turbulence characterization campaign (Ch. 2) as input to the performance study. I first verified that the telescope model was realistic by comparing the image properties of the simulations in seeing limited mode with current on-sky performances of SALT. Their good agreement ensured us that the subsequent simulations in AO mode could be trusted and provided realistic estimations of the expected performances on SALT.

The first step of this study consisted in choosing an optimal AO configuration given the Sutherland site characteristics and SALT optical properties. This led to the choice of a 34x34 configuration, optimized for NGS of R=12. The simulations showed that the working NGS magnitude range of the system is 10 to 14 R-mag. I could have opted for a larger system dimension, given the relatively small value of r_0 at the Sutherland site, in order to gain in spatial sampling across the wavefront, and hence obtain a better correction. However, this will have been at the expense of sky coverage. Given an NGS of R-mag between 10 and 14, I estimated the sky coverage, for an NGS search field up to 1 arcminute away from the science object. I found 24% of sky coverage towards the galactic center, 10% at 30^o away from the galactic center, and 5% at 90^o.

SALT being primarily designed for spectroscopy, I focused the AO study on spectroscopic performances and used the encircled (EE) and enslited (ESE) energy as the AO performance metric. In particular, I compared the performances in seeing limited mode and with AO correction, for apertures corresponding to the ones currently in use on the two SALT spectrographs: RSS and HRS. I looked at the performances at three typical wavelengths in R-band(700 nm), J-band(1200 nm) and H-band(1600 nm). I chose two parameters to quantify and compare the instruments' capabilities that an AO system could improve on: the resolving power and the required exposure time to achieve a given SNR. In the case of RSS-VIS, I found that a 30% increase in resolution at

an ESE of 50% could be achieved in R-band (700 nm). For a 1.1" slit, corresponding to 50% of ESE in seeing limited mode, the AO correction could allow to decrease the exposure time by a factor of 1.2 while keeping the same SNR. In the case of HRS, the results show that with AO assistance, the exposure times could be reduced by 12% to 20% depending on the fiber used. Alternatively, one could consider using smaller fibers to increase the resolving power by 19 to 23% while preserving the same SNR as in seeing limited mode. For the upgrade of RSS, with the RSS-NIR arm, I found that using AO correction could decrease the exposure time by 40 to 60% for the RSS-NIR fiber sizes of 0.6" and 0.9". Considering the potential use of smaller fibers made possible by using AO, the resolving power could be increased by 25 to 30% in J and H-band, respectively.

Those results are all in the case of on-axis correction. To increase the sky coverage, one can consider using NGS further away from the scientific target, however, this will be at the expense of a poorer correction due to the anisoplanatism effect. I investigated the loss of correction as we go further away from the NGS. I concluded that searching for NGS up to 1' away from the science target provides a good compromise between performances and sky coverage. I also found, for targets towards the galactic center, that increasing the patrol field up to 2' will provide close to full sky coverage. However, the search for NGS further away from the science target is at the expense of a loss in correction efficiency. In addition, looking at performances in R-band (700 nm) under different seeing conditions gave indications of how often one can expect a given level of performances. Considering a patrol field of 2 arcminutes radius around the science target, for a 1" aperture, we could have 20% or more gain in EE, 70% of the time.

Overall the dimensioning and performance study suggests that SALT could benefit from an adaptive optics correction, even from a simple single natural guide star AO system. SALT also has the advantage of being in the Southern hemisphere and can hence benefit from the higher density of stars towards the galactic center. For observations in that region, this ensures a reasonable sky coverage despite the use of relatively bright NGS of 12 R-band magnitudes, necessary to keep a high enough number of photons within the WFS sub-apertures. The gain in EE, delivered by an AO system, would increase the telescope efficiency by lowering the time required for an observation. Saving telescope time means that more programs could be observed increasing its scientific output.

Chapter 5

CONCLUSIONS

Contents

The main goal of this work was to carry out an extensive atmospheric turbulence characterization study at the Sutherland site to serve as the basis for a conceptual study of an adaptive optics system on SALT. The characterization part of this study was mainly based on MASS-DIMM data, collected over 5 years, starting from early 2010. In addition, a SLODAR, on loan from the University of Durham, was installed at Sutherland from February to April 2010. It provided a complementary measurement of the ground layer. The results from this work were presented in Ch. 2. In the framework of the site characterization I also helped develop a new instrument, the PML, in collaboration with the "laboratoire Lagrange" at the University of Nice Sophia Antipolis. As part of the work presented in this thesis, I implemented a data processing scheme as well as a method of inversion to recover the turbulence profiles from the measurements. This work was presented in Ch. 3. Based on the site monitoring results, I implemented adaptive optics simulations in order to explore the potential improvements that could be achieved on SALT. Those simulations, based on PAOLA (Jolissaint, 2010, 2014) analytic modeling, were presented in Ch. 4.

5.1 Main Results from the site characterization campaign

This study showed that the median seeing at ground level, over a 5 year period of time from January 2010 to November 2015, at the Sutherland site was 1.51". While a direct comparison with previous measurements is not possible (due to discrepancies between the methods used), this result can be partly explained by the longer exposure time used in previous studies, smoothing out the turbulence and hence underestimating the seeing. There is also a possibility that the seeing conditions have degraded since 2000 when the last campaign found a median seeing of 0.95" (Erasmus, 2000). There have been suggestions of El Niño / La Niña influence on the seeing conditions at other sites (Sarazin, 2010). This could be a plausible explanation for the Sutherland seeing degradation but needs further investigation of correlations with longer term climatic changes before drawing any conclusions. This work also, allowed us to confirm some previous results. As in the Erasmus (2000) study, I found a strong correlation with wind direction. South-Easterly winds are associated with bad seeing conditions and the North-Westerly are associated with good seeing conditions. Having 5 years of data also allowed us to look at seasonal patterns. It appears that the winter months (June, July, August) are generally associated with worse seeing (1.63"). In addition, the results from MASS and SLODAR provided turbulence profile information, that was missing from previous studies. I found that nearly 85% of the turbulence was located in the

ground layer, below 1 km, with a median GL seeing of 1.34" for a median FA seeing of 0.42". Further investigation, based on the SLODAR results, showed that the main contributors to the GL turbulence were the first 30 m and a broad layer located between 300 and 500 meters above ground. Moreover, exploring potential seasonal trends of the turbulence profile, I found that the summer months (December, January, February) had a higher FA contribution to the overall turbulence as compared to the rest of the year. This seems to be associated with turbulence in the 2-3 km wind shear layer. Retrieving wind speed and direction, and potentially the temperature gradient as well, specific to this altitude range, from the NCEP/NCAR [1] reanalysis data, could allow to derive more specific correlations and explanation for this trend.

In addition to the seeing value and the turbulence profile, the MASS-DIMM instrument also gives measurements of the coherence time (τ_0) and the isoplanatic angle (θ_0). With a value of 1.94", the median θ_0 is slightly lower than what is observed at most other major observatories. On the other hand, having a median value of 5.38 ms, τ_0 is longer than at most other observatories. Moreover, a much longer coherence time of 12.99 ms has been recorded for 20% of the data set.

Overall, the Sutherland site has a significantly worse median seeing as compared to most other major observatories. This could be explained by its much lower altitude, on average a 1000 meters below other major observatories. However, with a very strong ground layer and a relatively longer than average coherence time, it has significant potential for improvements on seeing-limited observations thanks to ground layer adaptive optics correction.

5.2 Summary on the PBL instrument development

The main reason driving the development of the PBL instrument, despite the number of already existing devices, was to provide better altitude-resolution than what is delivered by the currently available instruments. It can also sense both the GL and FA turbulence, whereas current devices that deliver similar resolution are only sensitive to one or the other.

For the PBL development framework I set up the data processing scheme and implemented a simulated annealing based inversion method to extract the turbulence profile. I demonstrated that we could reconstruct a 33 layers profile. The distribution of those layers gives 10 layers in the GL with 100 m resolution, and 23 layers in the FA with resolutions ranging from 500 m, for the lower layers, to 2 km, for the higher layers. I was able to validate the data processing and inversion method based on cross-comparisons with MASS-DIMM and GSM data.

Based on simulations with synthetic data, I estimated the error to be within 14% of the actual value. Further development and potential extensions to the PBL instrument are discussed in 5.4.

5.3 Conclusions from the AO simulations study

The goal of this part of the work, presented in Ch. 4, was to explore the possibility of using an adaptive optics system on SALT. At this stage of the study, it was restricted to the high-level conceptual design, without getting into the details of the different components of the system. This study was not driven by a specific science case either, hence focused on very general parameters for the performance evaluation such as: sky coverage and gain in enslited (ESE) or encircled (EE) energy. As SALT's primary instruments are the RSS and HRS (two spectrographs) I looked at the improvement in ESE and/or EE could impact the resolving power and the required integration times for the different instrument setups.

For the initial optimization study, based on a trade-off between the level of wavefront correction and the sky coverage, I settled on a system using a 34x34 Shack-Hartmann wavefront sensor

[1] NCEP/NCAR website

(SHWFS) in Fried geometry with the deformable mirror (DM) and using a single natural guide star (NGS) with a R-mag ranging from 10 to 14 magnitudes. For a maximum separation angle of 1 arcminute between the science target and the NGS, the sky coverage varies from 26% towards the Galactic plane down to 5.5% at the Galactic poles. Extending the NGS search field out to 2 arcminutes increases the sky coverage to 96% and 20%, towards the Galactic plane and poles, respectively. However, the use of NGSs further away from the science target results in a lower correction efficiency due to the anisoplanatism effect.

Using this conceptual AO system, together with an atmosphere model based on the site characterization and a realistic model of the SALT telescope, including known optical aberrations, I ran a number of simulations in order to evaluate the spectroscopic performances of AO correction on SALT. I found that for instruments similar to the current and upcoming SALT instrumentation suite, one could expect a 25% to 35% increase in resolving power while maintaining an ESE/EE of 50%. If the observations can be done with an ESE/EE lower than 50%, the potential gain in resolving power is even larger. Similarly, the exposure time on the different set of slits and fibers currently in use could be decreased. For the RSS-VIS using 0.6", 0.9", 1" and 2" slits at 700 nm, the greater concentration of energy provided by AO correction would allow a reduction of the exposure time by a factor 1.22, 1.17, 1.13 and 1.05 respectively. For the 0.6" and 0.9" fibers planned for RSS-NIR, the exposure time could be decreased by a factor 2.21 and 1.66, respectively, when observing at 1200 nm. Observation at 1600 nm would benefit from the AO correction with a reduction of the exposure time by a factor 2.83 and 1.81, for the same respective fibers. As for HRS, using 1.56" and 2.23" fibers, the exposure time for observations at 700 nm could be reduced by a factor 1.25 and 1.14, respectively. Lowering the necessary integration time for a science program will increase the efficiency and scientific output of SALT, as a larger number of programs could be observed each night. Eventually, one could obtain even better improvement when looking at future instruments, if those were designed to work in AO mode. The AO correction would be the most beneficial for high-resolution spectroscopy, for which the use of smaller apertures is required. This could also allow access to fainter objects at similar resolution and SNR. In addition, the specific design of SALT, having all of its instruments located on the payload at prime focus, limits the volume and weight available for prime focus instruments. An AO-assisted spectrograph, with equivalent performances as a seeing-limited one, can be significantly smaller and lighter (Ge et al., 1998; Pasquini et al., 1998). In the specific case of SALT, where room and payload at prime focus are scarce, reducing the instrument size and weight present the advantage of potentially be able to pack more instruments on the tracker.

5.4 Future work

While greatly improving on the former site characterization, as well as providing up-to-date and real-time seeing measurements to all observers on the Sutherland plateau, work still needs to be done in terms of site monitoring. The MASS-DIMM instrument is currently located at ground level, and it is clear that the measurements are affected by convection from the ground and turbulence due to the surrounding building structures. Ideally one would want to put it on an 8-meter tower, as the lowest point of the SALT primary mirror array, or at least 5-meter, as it is done at many other sites. In the specific case of SALT, its 30 meters high dome, on one hand, constitutes a shelter against the surface layer turbulence, but on the other hand, produces internal dome seeing. In the future, and for further defining a potential AO design, it will be necessary to measure SALT dome seeing. A straightforward solution to estimate the overall improvement possible would be to use two DIMM instruments, one located at ground level inside the dome and the second one up close to the dome entrance, on the dome itself or on the external rail of the dome. Although the practicalities of this, with restrictions on sky visibility, make it difficult to realize as a permanent setup.

In terms of the PBL instrument development status, there is still work to be done. The

simulated annealing method of inversion could still be further optimized in order to lower the reconstruction error. In addition, we can also investigate the possibility of increasing the number of reconstructed layers without increasing the noise between adjacent layers. In the present work I have been using a fixed value for $\mathcal{L}_0$ and ultimately, I should be able to implement a reconstruction scheme that will include both the profile of $C_n^2(h)$ and $\mathcal{L}_0(h)$, as well as extracting the value of τ_0 and θ_0. Work is also currently being done in order to use a faster reconstruction method that could deliver real-time measurements. For example a modified non-negative least square method is under investigation.

In terms of further investigations for a potential AO system on SALT, a number of things still need to be explored and defined. The most important factor, which was ignored for the present study, is the fact that the primary mirror segments are not phased. The phasing of the mirror was not implemented since it is not necessary for the operation of the current seeing-limited instruments. However, it seems possible for the current primary mirror structure and segment actuators to achieve an alignment to a higher precision as soon as the measuring device used for alignment can provide the necessary accuracy for phasing the primary mirror segments. The phasing of the primary mirror may be considered if correction by an AO system is judged to have a demonstrable improvement in performance for the next generation of instruments. Apart from the segments phasing, the static aberrations on SALT, due to imperfections on the primary mirror segments as well as residual aberrations in the SAC, are quite large. While those are not significant for seeing-limited observations, it become an issue when adaptive optics correction is considered. When the AO system applies corrections on the DM, part of the DM stroke can be used to compensate for these static aberrations. However, the more stroke it uses to correct for the telescope static aberrations the less is available to correct for the wavefront distortion due to atmospheric turbulence. One way of improving the correction efficiency would be to correct the static aberrations upstream from the main AO system. This correction could be done with another AO system, only correcting for low order aberrations, also active optics correction should be sufficient since those are static aberrations, with a potential slow variability associated with structure flexure and/or segments' alignment slowly changing. In order to increase the sky coverage without losses in efficiency, one could also look a the possibility of using a Rayleigh laser guide star. Also, as seen in the simulations, an AO system is most beneficial for the smallest apertures sizes, hence to take full advantage of it, one should consider options for future instruments that are designed to be used in AO mode using smaller apertures (i.e. fibers and slits) than those of the current seeing-limited instruments. Finally, in order to advance the design of a possible AO system, looking at specific types of wavefront sensors and DM, implemented in an end-to-end simulation, is needed. In addition, a set of science drivers should be defined. The choice of system devices is greatly dependent on the final science that it will be mainly used for.

Bibliography

Avila R., Ziad A., Borgnino J., Martin F., Agabi A., Tokovinin A., 1997, J. Opt. Soc. Am. A, 14, 3070

Babcock, 1953, PASP, 65, 229

Bahcall J. N. and Soneira R. M., 1981, ApJS, 47, pp. 357-403

Barnes S. I., Cottrell P. L., Albrow M. D., Frost N., Graham G., Kershaw G., Ritchie R., Jones D., Sharples R., Bramall D., Schmoll J., Luke P., Clark P., Tyas L., Buckley D. A. H. and Brink J., 2008, Proc. SPIE, 7014

Batchelor G. K., 1970, "The theory of homogeneous turbulence", Cambridge Univ. Press

Berdja A., Prieto G., Thomas-Osip J. E., 2011, MNRAS, 416, pp. 553-558

Blanc A., Fusco T., Hartung M., Mugnier L.-M., Rousset G., 2003, A&A, 399, 373-383

Borgnino J., Martin F., Ziad A., 1992, Optics Communications, 91, 267

Bramall D. G., Sharples R., Tyas L., Schmoll J., Clark P., Luke P., Looker N., Dipper N. A., Ryan S., Buckley D. A. H., Brink J. and Barnes S. I., 2010, Proc. SPIE, 7735

Brooks K. J., Catala L., Kenworthy M. A., Crawford S. M., Codona J. L.,2016, Proc. SPIE, 9912, 991203

Buckley D. A. H., 2008, ASP Conf. Series, 329, 273

Burgh E. B., Nordsieck K. H., Kobulnicky H. A., Williams T. B., O'Donoghue D., Smith M. P., and Percival J. W., 2003, Proc. SPIE, 4841, pp. 1463–1471

Burke R. B., 1962, "The Opus Majus of Roger Beacon", Russel & Russel edition Vol. 2, P. 535-542

Butterley T., Wilson R. W., Chun M. R., Avila R., Aviles J.-L. ,2008, Proc. SPIE, 7015, 70154L

Butterley T., Wilson R., Sarazin M., 2006, MNRAS, 369, 835

Carbillet M. et al., 2005, MNRAS, 256, 1263

Catala L., Crawford S. M., Buckley D. A. H., Pickering T., Wilson R., Butterley T., Shepherd H., Marang F., Matshaya P. and Fourie C., 2013 MNRAS, 436, 590

Chun M., Wilson R., Avila R., Butterley T., Aviles J.-L., Wier D., Benigni S., 2009, MNRAS, 394, 1121

Chun M. et al., 2009, MNRAS, 394, 1121

Codona J. L., 2012 Proc. SPIE. 8447, 84476P

Conan J.-M., Rousset G., Madec P.-Y., 1995, JOSA, 12, 1559-1570

Conan J.-M., 1994, PhD thesis, Université Paris XI Orsay, Etude de la correction partielle en optique adaptative. .

Coulman C. E., 1985, ARA&A, 23, 19

Crause L. A., Sharples R. M., Bramall D. G., Schmoll J., Clark P., Younger E. J., Tyas L. M. G., Ryan S. G., Brink J. D., Strydom O. J., Buckley D. A. H., Wilkinson M., Crawford S. M. and Depagne E. 2014, Proc. SPIE, 9147, 91476T-1

Crause L. A., O'Donoghue D. E., O'Connor J. E., Strumpfer F., Strydom O. J., Sass C., du Plessis C. A., Wiid E., Love J., Brink J. D., Wilkinson M. and Coetzee C., 2012, Proc. SPIE, 8444, 84444I

Dali Ali W., Ziad A., Berdja A., Maire J., Borgnino J., Sarazin M., Lombardi G., Navarrete J., Vazquez Ramio H., Reyes M., Delgado J. M., Fuensalida J. J., Tokovinin A., Bustos E., 2010, A&A, 524, id.A73 pp.8

Doering R. L., Sheinis A. I. and Wolf M. J., 2010, AAS, 42, 406

Egner S. E. et al., 2007, PASP, 119, 669

Els S. G., Sebag J., 2011, RMXAC, Vol. 41, pp. 79-82

Els S. G. et al., 2009, PASP, 121, 922

Els S. G., Schoeck M., Seguel J., Skidmore W., Walker D., Tokovinin A., Kornilov V., Riddle R., Travouillon T., Bustos E., Vasquez J., Blum R., Gregory B., Gillett P., 2008 Proc. SPIE, 7012, 701222

Erasmus A., 2000, Sth. Af. J. Sci., 96, 475

http://www.eso.org/gen-fac/pubs/astclim/papers/review00/seeing3.html

Foy R., Labeyrie A., 1985, A&A, 152, pp. L29-L3185-87

Fried D. L., 1982, JOSA, 72, 52-61

Fried D. L., 1977, JOSA, 67, 370

Fried D. L., 1966, PASP, 56, 1372

Fried D. L. Could J. D., 1966, JOSA, 56, 12

Frisch U., 1995, "Turbulence, the Legacy of A. N. Kolmogorov", Cambridge Univ. Press

Fusch A., Tallon M., Vernin J., Proc. SPIE, 2222, pp. 682

Fusco T., Rousset G., Petit C., J.-L. Beuzit, Conan R., Montagnier G., Mouillet G., Dohlen K.,2005, Proc. SPIE, 5903, pp. 179-189

Ge J., Agel C., Shelton C., 1998, Proc. SPIE, 3355, pp. 253

Gochermann J. et al., 1999, Exp. Ast., 9, 1

Greenwood D. P. and Tarazano D. O., 1974 A proposed form for the atmospheric microtemperature spatial spectrum in the input range, RADC-TR-74-19 (AD-776294/1G1) (Rome Air Development Center 1974)

Guyon O., 2010, PASP, 122:49-62

Harding G. A., 1974, SAAOC, Vol. 1 - P. 31

Hartmann J., 1900, Bemerkungen uber den bau und die justirung von spektrographen, Z.Instrumentenkd. 20: 47–58.

Rosch J., 1962, IAU Symposium no.19, Gauthier-Villars, Paris

Jiang W., Li H., 1990, Proc. SPIE, 1271, pp.82-93

Jolissaint L., 2014 PAOLA - an Astronomical Adaptive Optics Modeling Toolbox - User Manual V7.3

Jolissaint L., 2010 JEOS Rapid publications, Europe, v. 5, ISSN 1990-2573

Kenworthy M. A., Sheinis A., Buckley D. A. H., 2008, Proc. SPIE, 7015, 701563

Kirkpatrick S., Gelatt C. D., Vecchi M. P. 1983, Science, New Series Vol. 220, No. 4598, 671-680

Kobulnicky H. A., Nordsieck K. H., Burgh E. B., Smith M. P., Percival J. W., Williams T. B., and O'Donoghue D., 2003, Proc. SPIE, 4841, pp. 1634–1644

Kolmogorov A. N., 1941a, Dokl. Akad. Nauk. SSSR, 30:9-13

Kolmogorov A. N., 1941b, Dokl. Akad. Nauk. SSSR, 31:538-540

Kornilov V., Kornilov M., 2011, Exp. Ast., Vol. 29, Issue 3, pp 155-176

Kornilov V. and Safonov B., 2011, MNRAS, 418, 1878

Kornilov V., 2011, A&A, 530, A56

Kornilov V., Tokovinin A., Shatsky N.,Voziakova O., Potanin S. F., Safonov B., 2007, MNRAS, 382, 1268

Kornilov V., Shatsky N., 2005, MASS data reprocessing

Kornilov V., Tokovinin A., Vozyakova O., Zaitsev A., Shatsky N., Potanin S. F., Sarazin M., 2003, Proc. SPIE, 4839, pp. 837

Kornilov V., Shatsky N., Vaziakova O., 2003, MASS Software Version 2.04 User Guide

Labeyrie A., 1970, A&A, 6, 85-87

Lardiere O., Carbillet M., Riccardi A., Salinari P., 2004, Proc. SPIE, 5490, 516

Lasker B. M., Lattanzi M. G., McLean B. J., Bucciarelli B., Drimmel R., Garcia J., Greene G., Guglielmetti F., Hanley C., Hawkins G., Laidler V. G., Loomis C., Meakes M., Mignani R., Morbidelli R. Morrison J., Pannunzio R., Rosenberg A., Sarasso M., Smart R. L., Spagna A., Sturch C. R., Volpicelli A., White R. L., Wolfe D., Zacchei A., 2008, AJ, 136, 735-766

Liu L.-Y., Yao Y.-Q., Wang Y., Ma J.-L., He B.-L., Wang H.-S., 2010, A&A, 10, pp. 1061-1070

Lombardi G., Sarazin M., Char F., González Ávila C., Navarrete J., Tokovinin A., Wilson R. W., Butterley T. 2014, RMXAC, Vol. 44, pp. 208-209

Lombardi G., Navarrete J., Sarazin M., 2008, Proc. SPIE, 7012, 701221.701221.11

Mahajan V. N., 1981, JOSA, Vol. 71, Issue 1, pp. 75-85

Mahé F., Michau V., Rousset G., Conan J.-M.,2000, Proc. SPIE, 4125, pp. 77-86

Maire J., Ziad A., Borgnino J., Martin F., 2007, MNRAS, 377, 1236-1244

Martin H. M., 1987, PASP, 99:1360-1370

Masciadri E., Stoesz J., Hagelin S., Lascaux F., 2010, MNRAS, 404, 144

Mateen M., Garrel V., Hart M., Guyon O., 2010, Proc. SPIE, 7736

Merkle F., Gerhing G., Rigaut F., Léna P., Rousset G., Fontanella J. C. and Gaffard J. P., 1991, Proc. SPIE, 1542, pp. 308-318

Merkle F., Kern P., Léna P., Rigaut F., Fontanella J. C., Rousset G., Boyer C., Gaffard J. P. and Jagourel P., 1989, The Messenger, 52, 1-4

Obukhov, A. M., 1949, Izv. Akad. Nauk. SSSR, Ser. Geogr. and Geophys. 13, 58–69

O'Donoghue D. E., O'Connor J., Crause L. A., Strumpfer F., Strydom O. J., Brink J. D., Sass C., Wiid E. and Atad-Ettedgui E., 2010, Proc. SPIE, 7739, 77390Q

O'Donoghue D., Buckley D. A. H., Balona L. A., Bester D., Botha L., Brink J., Carter D. B., Charles P. A., Christians A., Ebrahim F., Emmerich R., Esterhuyse W., Evans G. P., Fourie C., Fourie P., Gajjar H., Gordon M., Gumede C., de Kock M., Koeslag A., Koorts W. P., Kriel H., Marang F., Meiring J. G., Menzies J. W., Menzies P., Metcalfe D., Meyer B., Nel L., O'Connor J., Osman F., Du Plessis C., Rall H., Riddick A., Romero-Colmenero E., Potter S. B., Sass C., Schalekamp H., Sessions N., Siyengo S., Sopela V., Steyn H., Stoffels J., Scholtz J., Swart G., Swat A., Swiegers J., Tiheli T., Vaisanen P., Whittaker W., and van Wyk F., 2006, MNRAS, 372, 151–162

O'Donoghue D. E. and Swat A., 2002, Proc. SPIE, 4411, pp. 72-78

Orlov V. G.,Sánchez L. J., Avila R. and Voitsekhovich V. V., 2003, RevMexAA (Serie de Conferencias), 19, 52–58

Pasquini L., Delabre B., Avila G., Bonaccini D., 1998, Proc. SPIE, 3355, pp.105

Poyneer L., Macintosh B., 2004, JOSA, Vol. 21, issue 5, 810-819

Primot J., Rousset G., Fontanella J.-C., 1990, JOSA, 7, 1598-1608

Ragazzoni R., Farinato J., 1999, A&A, 350, L23-L26

Ramsey L. W. et al., 1998, Proc. SPIE, 3352, pp. 34-4

Ramsey L. W., Sebring T. A. and Sneden C., 1994, Proc. SPIE, 199, pp. 31-40

Richardson L. F., 1922, "Weather prediction by numerical process", Cambridge Univ. Press

Rigaut F., 1992, Univ. de Paris, Rigaut F.

Robert C., Conan J.-M., Michau V., Fusco T., Vedrenne N., 2006, JOSA, Vol. 23, issue 3, 613-624

Roddier F., 1988, Appplied Optics, Vol. 27, Issue 7, pp. 1223-1225

Roddier F., 1981, Prog. Optics, 19, 281

Roddier F., Roddier C., 1986, Proc. Soc. Photo-Opt. Instrum. Eng., Advanced technology optical telescopes III, volume 628, pages 298–304

Sarazin M., 2010 - http:www.eso.org/gen-fac/pubs/astclim /papers/review00/seeing3.html

Sarazin M., Melnick J., Navarrete J., Lombardi G., 2008, The Messenger, 132, 11

Sarazin M., 1997, Proc. SPIE, 3125, pp. 366

Sarazin M., Roddier F., 1990, A&A, 227, 294

Sarazin M., 1986a, SPIE Conf. S., 628, pp. 138

Sauvage J.-F., Fusco T., Rousset G., Petit C., 2006, Proc. IAU Colloquium, Cambridge U. Press, pp.607-612

Sebring T. A. and Ramsey L. W., 1997, Proc. SPIE, 2871, pp. 32-37

Sebring T. A., Booth J. A., Good J. M., Krabbendam B. L., Ray F. B. and Ramsey L. W., 1994, Proc. SPIE, 2199, pp. 565-572

Siegmund O. H. W., McPhate J., Tremsin A., Vallerga J. V., Welsh B. Y. and Wheatley J. M., 2008, AIP Conf. S., 984, 103–114

Simons D., 1995, Gemini technical notes - TN-PS-G0030

Soloveva M. A., Venediktov V. Y., 2015 Proc. of SPIE Vol. 9508 95080K

Stocks J. L. (translated by), 1930, "The works of Aristotle translated into English", Oxford U. Press - Ross W. D. editor, Vol. 2, p. 290a-18 (De Calco, book 2, Chap. 8)

Taylor G. I., 1938, Proc. R. Soc. London Ser., vol.64 - p.476

Tatarski V. I., 1961, Dover Publications, Inc., New York

Thomas-Osip J. E. et al., 2012, PASP, 124, 84

Thomas S., Fusco T., Tokovinin A., Nicolle M., Michau M., Rousset G., 2006, MNRAS, 371, 323–336

Thompson L. A., Gardner C. S., 1987, Nature, 328, pp. 229-231

TMT site selection team, 2008, TMT site testing final report, TMT.SIT.TEC.08.2003.REL01

Tokovinin A., Kornilov V., 2007, MNRAS, 381, 1179

Tokovinin A., 2006, "Calibration of the MASS time constant measurements". Internal report - http://www.ctio.noao.edu/ atokovin/profiler/timeconst.pdf

Tokovinin A., Vernin J., Ziad A., Chun M., 2005, PASP, 117:395-400

Tokovinin A., Kornilov V., Shatsky N.,Voziakova O., 2003b, MNRAS, 343, 891

Tokovinin A., Bustos E., Schwarz H., 2002, CTIO RoboDIMM v2.3 software description

Tokovinin A., 2002, PASP, 114, 1156

Tokovinin A., Bustos E., Shwarz H., 2002, CTIO RoboDIMM v2.3 software description

Travouillon T., Els S., Riddle R. L., Schöck M., Skidmore W., 2009, PASP, 121, 787

Vázquez-Ramió et al., 2012, PASP, 124, 868

Vernin J., Munoz-Tunon C., 1994, A&A, 284, 311

Vernin J., Roddier F., 1973, JOSA, 63, 270

Wang et al., 2006, Proc. SPIE, 6267, 62671S

Warner B., 1994, MNSSA, 53, 46

Wilson R., Butterley T., Osborn J. and Shepherd H., 2011, "Optical turbulence profiling and applications for astronomy," in Signal Recovery and Synthesis, OSA Technical Digest (CD) (Optical Society of America, 2011), paper JTuA1.

Wilson R., Butterley T., Sarazin M., 2009, MNRAS, 399, 2129-2138

Wilson R., Saunter C. D., Guerra J. C., 2004, Proc. SPIE, 5382, pp. 661-667

Wolf M. J., Mulligan M. P., Smith M. P., Adler D. P., Bartosz C. M., Bershady M. A., Buckley D. A. H., Burse M. P., Chordia P. A., Clemens J. C., Epps H. W., Garot K., Indahl B. L., Jaehnig K. P., Koch R. J., Mason W. P., Mosby G., Nordsieck K. H., Percival J. W., Punnadi S., Ramaprakash A. N., Schier J. A., Sheinis A. I., Smee S. A., Thielman D. J., Werner M. W., Williams T. B., Wong J. P., 2014, Proc. SPIE, 9147, 91470B

Wood P. R., Rodgers A. W. and Russell K. S. , 1995, PASA, 12, 97-105

Ziad A., Blary F., Borgnino J., Fanteï-Caujolle Y., Aristidi E., Martin F., Lantéri H., Douet R., Bondoux E., Mékarnia D., 2013, A & A, Volume 559, id.L6, 4 pp

Ziad A., Borgnino J., Martin F., Agabi A., 1994, A & A, Volume 282, 1021-1033